

<https://doi.org/10.15388/vu.thesis.371>

<https://orcid.org/0000-0003-2436-6528>

VILNIUS UNIVERSITY

STATE RESEARCH INSTITUTE CENTER FOR PHYSICAL SCIENCES AND  
TECHNOLOGY

Ernesta Bužavaitė-Vertelienė

# Strong coupling of hybrid Tamm and surface plasmon polaritons states

**DOCTORAL DISSERTATION**

Natural Sciences,  
Physics (N 002)

VILNIUS 2022

The dissertation was prepared between 2018 and 2022 at the State Research Institute Center for Physical Sciences and Technology.

**Academic supervisor** – Prof. Dr. Zigmas Balevičius (State Research Institute Center for Physical Sciences and Technology, Natural sciences, Physics, N 002).

This doctoral dissertation will be defended in a public meeting of the Dissertation Defence Panel:

**Chairman** – Prof. Dr. Aidas Matijošius (Vilnius University, Natural sciences, Physics, N 002).

**Members:**

Prof. Dr. Saulius Juodkazis (Swinburne University of Technology, Natural sciences, Physics, N 002),

Dr. Raimondas Petruškevičius (State Research Institute Center for Physical Sciences and Technology, Natural sciences, Physics, N 002),

Prof. Habil. Dr. Valdas Sirutkaitis (Vilnius University, Natural sciences, Physics, N 002),

Prof. Habil. Dr. Sigitas Tamulevičius (Kaunas University of Technology, Natural sciences, Physics, N 002).

The dissertation shall be defended at a public meeting of the Dissertation Defence Panel at 13 (hour)/ on 23 September 2022 in meeting room D401 of the State Research Institute Center for Physical Sciences and Technology.

Address: Saulėtekis ave., 3, D401, Vilnius, Lithuania

Tel. +37052649211; e-mail: office@ftmc.lt

The text of this dissertation can be accessed at the libraries of State research institute Center for Physical Sciences and Technology and Vilnius University, as well as on the website of Vilnius University:

[www.vu.lt/lt/naujienos/ivykiu-kalendorius](http://www.vu.lt/lt/naujienos/ivykiu-kalendorius)

<https://doi.org/10.15388/vu.thesis.371>

<https://orcid.org/0000-0003-2436-6528>

VILNIAUS UNIVERSITETAS

VALSTYBINIS MOKSLINIŲ TYRIMŲ INSTITUTAS FIZINIŲ IR

TECHNOLOGIJOS MOKSLŲ CENTRAS

Ernesta Bužavaitė-Vertelienė

# Stiprioji sąveika hibridinėse Tamm'o ir paviršinių plazmonų poliaritonų būsenose

**DAKTARO DISERTACIJA**

Gamtos mokslai,

Fizika (N 002)

VILNIUS 2022

Disertacija rengta 2018–2022 metais Valstybiniame mokslinių tyrimų institute Fizinių ir technologijos mokslų centre.

**Mokslinis vadovas** – Prof. dr. Zigmas Balevičius (Valstybinis mokslinių tyrimų institutas Fizinių ir technologijos mokslų centras, gamtos mokslai, fizika, N 002).

Gynimo taryba:

**Pirmininkas** – prof. dr. Aidas Matijošius (Vilniaus universitetas, gamtos mokslai, fizika, N 002).

**Nariai:**

Prof. dr. Saulius Juodkasis (Svinburno technologijų universitetas, gamtos mokslai, fizika, N 002),

Dr. Raimondas Petruškevičius (Valstybinis mokslinių tyrimų institutas Fizinių ir technologijos mokslų centras, gamtos mokslai, fizika N 002),

Prof. habil. dr. Valdas Sirutkaitis (Vilniaus universitetas, gamtos mokslai, fizika, N 002),

Prof. habil. dr. Sigitas Tamulevičius (Kauno technologijų universitetas, gamtos mokslai, fizika, N 002).

Disertacija ginama viešame Gynimo tarybos posėdyje 2022 m. rugsėjo mėn. 23 d. 13 val. Valstybinio mokslinių tyrimų instituto Fizinių ir technologijos mokslų centro D401 posėdžių salėje.

Adresas: Saulėtekio al. 3, D401, Vilnius Lietuva, tel. +37052649211; el. paštas office@ftmc.lt

Disertaciją galima peržiūrėti Valstybinio mokslinių tyrimų instituto Fizinių ir technologijos mokslų centro bei Vilniaus universiteto bibliotekose ir VU interneto svetainėje adresu:

<https://www.vu.lt/naujienos/ivykiu-kalendorius>

## LIST OF ABBREVIATIONS

AOI – angle of incidence  
BSA – bovine serum albumin  
CM – cavity mode  
DLW – direct laser writing  
EMA – effective media approximation  
FWHM – full width at half maximum  
GCSF-R – granulocyte colony-stimulating factor receptor  
HLPP (HLPR) – hybrid lattice plasmon polariton (hybrid lattice plasmon resonance)  
LSP – local surface plasmon  
MSE – mean square error  
mQCM – modified quartz crystal microbalance sensor chip  
NIR – near infrared spectrum  
OTS – optical Tamm states  
PBG – photonic band gap  
PBS – phosphate-buffered saline  
PC – photonic crystal  
PMMA – poly(methyl methacrylate)  
RI – refractive index  
RIU – refractive index unit  
SAM – self assembling monolayer  
SE – spectroscopic ellipsometry  
SE-QCM – spectroscopic ellipsometry and quartz crystal microbalance  
SEM – scanning electron microscopy  
SEW – surface electromagnetic wave  
SLG – single layer graphene  
SLPR – surface lattice plasmon resonance  
SPP (SPR) – surface plasmon polariton (surface plasmon resonance)  
TE – transverse electric  
TIR – total internal reflection  
TIRE – total internal reflection ellipsometry  
TM – transverse magnetic  
TPP – Tamm plasmon polariton  
TPP-SPP – hybrid Tamm plasmon-surface plasmon polariton  
VIS – visible spectrum  
VASE – variable angle spectroscopic ellipsometry  
QCM-D – quartz crystal microbalance with dissipation

# CONTENTS

ACKNOWLEDGMENT .....	8
1 INTRODUCTION .....	9
2 LITERATURE OVERVIEW .....	19
2.1 Strong coupling between two harmonic oscillators .....	19
2.2 1D photonic crystals.....	23
2.3 Plasmonic excitations.....	25
2.3.1 Tamm plasmon polaritons.....	25
2.3.2 Surface plasmon polaritons .....	28
2.3.3 Hybrid Tamm plasmon-surface plasmon polaritons .....	31
2.3.4 Hybrid lattice plasmon polaritons .....	33
3 METHODS .....	36
3.1 Optical measurement methods .....	36
3.1.1 Spectroscopic ellipsometry .....	36
3.1.2 Total internal reflection ellipsometry .....	37
3.1.3 Types of ellipsometers .....	38
3.2 Sample production methods.....	39
3.2.1 Structures supporting Tamm plasmon polaritons states.....	39
3.2.2 Hybrid lattice plasmon polaritons formed by direct laser writing.....	40
3.3 Sample characterization methods.....	41
3.3.1 Raman spectroscopy .....	41
3.3.2 Scanning electron microscopy .....	42
3.4 Protein adsorption on sensor surfaces .....	44
4 RESULTS .....	47
4.1 The experimental evidence of strong coupling between tamm and surface plasmon polaritons modes .....	47
4.1.1 Introduction.....	47
4.1.2 Experimental demonstration of strong coupling regime .....	48
4.1.3 Fitting of the experimental results.....	53

4.2	Graphene influence on strong coupling between tamm and surface plasmon polaritons .....	57
4.2.1	Introduction.....	57
4.2.2	Study of graphene influence on strong coupling.....	58
4.3	Application of hybrid tamm plasmon-surface plasmon polaritons modes to biosensing .....	68
4.3.1	Introduction.....	68
4.3.2	TIRE for detection of GCSF-R immobilization on surface .....	69
4.3.3	Hybrid Tamm-surface plasmon polaritons mode for enhanced optical response of biosensor .....	74
4.4	Application of tamm plasmons and cavity modes for biosensing in combined spectroscopic ellipsometry and quartz crystal microbalance method .....	78
4.4.1	Introduction.....	78
4.4.2	Refractive index sensing .....	79
4.4.3	Application for biosensing .....	85
4.5	Gold microbump arrays for generation of hybrid lattice plasmon polaritons.....	91
4.5.1	Introduction.....	91
4.5.2	Hybrid lattice plasmon polaritons dispersion relations .....	93
4.5.3	Investigation of plasmonic properties .....	96
5	MAIN RESULTS AND CONCLUSIONS .....	104
6	SANTRAUKA.....	106
7	PUBLIKACIJŲ SĄRAŠAS .....	127
8	REFERENCES .....	130
	CURRICULUM VITAE .....	146

## ACKNOWLEDGMENT

During the four years of the thesis preparation, I have received enormous amount of support from my colleagues and family, to which I am very grateful. First of all, I would like to thank my supervisor prof. dr. Zigmas Balevičius for the opportunity to work on the thesis. I am grateful for the possibility to have scientific discussions, for strong support and help in the process of writing the thesis. Zigmas Balevičius shared his scientific expertise, guided, encouraged and helped me to grow as a researcher. I am also thankful to my colleague dr. Ieva Plikusienė, who gave me knowledge on how to perform the protein immobilization processes, as well support. It is a great privilege to have such wonderful colleagues.

I am grateful to the director of Center for Physical Sciences and Technology prof. habil. dr. Gintaras Valušis, as well as to the head of the Laser Technologies department dr. Gediminas Račiukaitis, for providing a platform to do research. A big thank you goes to all CPST colleagues for the advice, assistance and a friendly working environment. Especially to dr. Evaldas Stankevičius, dr. Tomas Tolenis and dr. Lina Grinevičiūtė for the preparation of the samples and to dr. Algirdas Selskis for the sample structural analysis.

Finally, I want to thank my wonderful, beautiful mother for raising and encouraging me to pursue my dreams and for all her love. I am also grateful to my husband who supported and motivated me to seek scientific career.



# 1 INTRODUCTION

In recent years the extensive research of interaction between photons and nano-structures has led to development of new concepts and prototype devices which are based on nanophotonics. These studies in nanophotonics first of all are related to the understanding of optically induced excitations in nano-scale structures and how the optical properties of such resonances depend on size, period and shape of the nanostructures. One of the areas, which has attracted much attention in the research, is plasmons in metal nanostructures. Plasmons are collective oscillations of conduction electrons in metals. Coupling of light to plasmon resonances in metal nanostructures has extensive studies primarily due to their ability to localize optical fields to volumes below the diffraction limit [1].

The new phenomena appear when two plasmon resonances in nano-structures are coupled to each other. Similar effect was extensively studied and can be traced for plasmon-exciton coupling [2,3]. Various emitters such as excitons in semiconductors, in dye or photochromic molecules [4–7] are able to support the energy exchanges with plasmonic resonances in strong coupling regime, thus are promising nanophotonic systems for new generation of nanolasers (spacers) [8,9], ultra-sensitive optical biosensing [10], control of chemical reaction rates [11,12], room-temperature condensation [8] and in quantum information processing [13]. The strong coupling phenomena also finds in the purely plasmonic nanostructures where two different or the same plasmonic excitations interact strongly with each other [14]. The main signature of strong coupling regime is that the energy exchange between two plasmonic excitations (this is also valid for plasmon-exciton coupling) occurs during a coherent time [15]. This energy exchange rate exceeds the damping rate and, as a result, the new hybrid plasmonic mode are generated. However, the main difference between plasmon-exciton and plasmon-plasmon coupling is that for the first case plasmon and exciton forms new hybrid polariton, meanwhile two plasmons itself already are polaritons which forms new polaritonic state where both single plasmon polaritons are involved. The key features offered by the strong coupling regime are significant control over polariton energy levels and the coherent, delocalized nature of the new polaritonic mode [16,17]. Rather a small number of publications have been dedicated for strong coupling between two plasmonic modes and their applications [18–20].

This PhD thesis is dedicated to detailed understanding of the hybrid light-matter polaritonic modes and to demonstrate its importance in all aspects, starting from fundamental research to the new nanophotonic applications

mentioned above. In this study, a simple approach of using optical filters which gives unambiguous experimental evidence of the strong coupling regime in the hybrid TPP-SPP polaritonic mode was applied for the very first time (Chapter 4.1). Also, it has been shown that the strong coupling between the Tamm plasmon polaritons (TPP) and surface plasmon polaritons (SPP) components in the hybrid plasmonic mode is sensitive to one graphene monolayer deposited on a metal surface (Chapter 4.2). The variation of coupling strength between the single graphene monolayer and PMMA layer on the top of the nanophotonic-plasmonic structure in the hybrid plasmonic mode allows the characterization of the optical properties of graphene.

In other parts of this PhD thesis, the applications of hybrid polaritonic modes for biosensing are presented (Chapter 4.3). For instance, the optimized sensitivity of the hybrid TPP-SPP mode was investigated and compared with the single SPR mode when detecting a BSA protein layer on the gold surface. The dispersion relations of the hybrid TPP-SPP and single SPR modes were used to explain the enhanced sensitivity of the ellipsometric parameters for the hybrid TPP-SPP mode over the conventional SPR. Moreover, the low-cost 1D plasmonic photonic structures supporting Tamm plasmon polaritons and cavity modes were employed for the optical signal enhancement modifying the commercially available QCM-D sensor chip in the combinatorial spectroscopic ellipsometry and quartz crystal microbalance (QCM-D) method (Chapter 4.4).

Finally, the fabrication of a large-scale lattice array of gold microbumps for the generation of hybrid lattice-propagated plasmon polaritons in the VIS-NIR range by using a direct laser writing technique was demonstrated (Chapter 4.5). The plasmonic structures exhibits narrow, low-loss resonances. This shows the potential impact of direct laser writing method as cost effective, fast and large area for creating integrated photonic devices with designed optical properties. The application of hybrid surface lattice-propagated resonances together with strong coupling regime leads to decreasing losses, resulting in the increased propagation length and better coherence properties of such plasmonic excitations, which in turn promises advanced optical properties.

## **OBJECTIVES**

The objectives of this PhD thesis were to study the properties of the optical response for various hybrid plasmonic modes based on SPP, TPP and surface lattice resonances. The main contribution of the studies was related to the hybrid TPP-SPP mode generation in total internal reflection ellipsometry

(TIRE) setup and application of these modes for plasmonic sensing with bio-related materials. In particular, focusing on the investigation of:

- By using optical filters, to cut the part of incident light spectra that allows to divide measured energy spectra into two parts, where in each range only one branch of the hybrid TPP-SPP plasmonic mode was excited directly by the incident light. Such methodology allows to study strong coupling in detail under experimental conditions.
- Strong coupling changes between the TPP and SPP component in the hybrid plasmonic mode due to the presence of graphene monolayer at the interface of PMMA and silver layers in order to have the possibility to tune the conductivity of the sensing layer through the presence of graphene, which influences the anti-crossing between the TPP and SPP resonances and optical dispersion of the hybrid TPP-SPP mode.
- Hybrid TPP-SPP mode for the application of enhanced sensing properties compared with widely used commercially available single SPR biosensors. The modified optical dispersion of the hybrid TPP-SPP mode due to the strong coupling could be employed for optimization and sensitivity control of the ellipsometric parameters in TIRE configuration.
- To employ the low-cost 1D plasmonic photonic structures supporting Tamm plasmon polaritons and cavity modes for the optical signal enhancement modifying the commercially available QCM-D sensor chip in the combinatorial spectroscopic ellipsometry and quartz microbalance method.
- To apply the lattice array of gold microbumps fabricated by direct laser writing method for the generation of hybrid surface lattice plasmonic resonances whose resonance quality is comparable with ones produced by the traditional lithography methods.

**Tasks to achieve the objectives:**

- To develop a simple experimental methodology by using optical filters to cut the part of incident light spectra for only one branch of the hybrid TPP-SPP mode direct excitation.
- To generate ellipsometric spectra with the whole spectra, a part with only TPP and a part with only SPP of the hybrid TPP-SPP mode in TIRE configuration on the structure photonic crystal/gold layer.
- To study the influence of the strong coupling in the hybrid TPP-SPP mode to its optical dispersion through the separation of TPP and SPP branches in the hybrid dispersion curves

- To compare the influence of the graphene monolayer to the whole optical response under excitation of single Tamm plasmon polaritons in variable angle spectroscopic ellipsometry (VASE) with hybrid TPP-SPP modes under strong coupling in TIRE configuration.
- To develop a multi-layer optical model for the 1D photonic crystal/silver/graphene/PMMA which reasonably well describes the excitation and strong coupling effect in hybrid TPP-SPP mode.
- To apply the hybrid TPP-SPP mode as a sensor probe for the GCSF receptor immobilization and BSA protein on the gold surface. Additionally, to compare the sensitivity of its ellipsometric parameters with those of the single SPR mode.
- To conduct numerical simulations of the optical response of 1D plasmonic nanophotonic structures supporting Tamm plasmon polariton and cavity modes which can be generated on the modified SE-QCM-D chip
- To compare the sensitivity of the ellipsometric parameters  $\Psi(\lambda)$  and  $\Delta(\lambda)$  for protein layer formation on modified SE-QCM-D chip due to the excitation of Tamm plasmon polaritons and cavity modes with conventional SE combined with QCM-D.
- To measure the optical response of ellipsometric parameters of the surface lattice arrays of gold microbumps and characterize the optical dispersion properties and generated plasmonic resonances
- To explain the physical principle of the generation such hybrid surface plasmonic resonances fabricated by direct laser writing method.

## SCIENTIFIC NOVELTY

The experimental studies conducted in the present PhD thesis are in the field of emerging area of plasmonics and nanophotonics which focuses on the interaction of photons with nano-structures.

The main novelty of these studies is the unambiguous experimental evidence of strong coupling between the TPP and SPP resonances in the hybrid TPP-SPP mode by tuning of the incident light spectra with the optical filters, for the very first time. If one component is excited at a resonant wavelength, the other is also present and can be controlled by strong coupling between TPP and SPP. The energy conversion between TPP and SPP shows a potential applications of hybrid TPP-SPP modes for integrated photonic devices.

From a point of view of a plasmonic nanostructures supported strong coupling studies the graphene monolayer influence to the conductivity of the

silver layer have shown that coupling strength, number of electrons involved in coupling to a hybrid plasmonic resonance, can be the figure of merit in order to have the possibility to tune the optical dispersion of the investigated nanostructures.

It has been shown that the application of hybrid TPP-SPP modes and single Tamm plasmon polaritons to biosensing gives the possibility to enhance the optical response of the system. In particular, the hybrid TPP-SPP and strong coupling regime was used for the first time for biosensing application. It was found that the sensitivity of the hybrid plasmonic mode can be made controllable by using the strong coupling effect between the TPP and SPP components. This reduces the metal losses of the SPP component and, as a result, narrows the plasmonic resonance. The optimized sensitivity of the hybrid TPP-SPP mode was more sensitive to the BSA protein layer formed on the sensor surface compared with the conventional single SPR mode. A feature of optical dispersion of Tamm plasmon polaritons namely, the wavevector is always smaller than the vector of light in the vacuum and thus, direct excitation of TPP without additional coupler, gives the possibility to enhance the optical signal on the sensing surface for conventional ellipsometry without the use of total internal reflection (TIR). To the best of our knowledge this is the first study and application of the Tamm plasmon polaritons and a cavity mode in the combinatorial SE-QCM-D method for the enhanced readout of the ellipsometric parameters.

The direct laser writing technique was employed for fabrication of a lattice array of gold microbumps which support hybrid lattice plasmon polaritons modes. These hybrid plasmonic modes are a result of a propagated surface plasmon resonance and in-plane Bragg reflections from the gold microbumps. The hybrid lattice plasmon polaritons (HLPP) modes exhibit a modified dispersion relation from the conventionally propagated surface plasmon resonance. The coupling of the in-plane Bragg reflections with the propagated surface plasmon resonance leads to ultra-narrow widths of the hybrid plasmonic resonances which are comparable with surface resonances in purely dielectric structures with low losses or plasmonic nanostructures produced by conventional lithography methods. The presented lattice array fabrication method shows significant technological progress in the formation of large-scale metallic arrays by using a laser-based technique and opens new possibilities for plasmonic-based applications in integrated photonic devices, optical sensors, and nanolasers.

## **PRACTICAL VALUE**

The application of optical filters for the analysis of coupling between plasmonic resonances enable to evaluate if the strong coupling between two or more plasmonic excitations is present. This method is suitable for various nanophotonic structures, supporting surface resonant states under strong coupling.

Use of the hybrid plasmonic modes under strong coupling reduces the propagation losses for the plasmonic excitations and increase the quality factor of these resonances, thus the optical signal sensitivity of the plasmon based biosensor is enhanced.

The Tamm plasmon polaritons dispersion property of the light in free space wave vector being always larger than the wave vector of TPP, allows to obtain the TPP modes by direct excitation, thus a prism coupler is not needed. This property enhances the spectroscopic ellipsometry optical signal in a combined spectroscopic ellipsometry and quartz crystal microbalance (SE- QCM) method.

The direct laser writing shows the potential application of such method for production of microbump lattice arrays, supporting narrow hybrid lattice plasmon polaritons that are by quality comparable to the ones produced by lithography methods. This feature of direct laser writing reduces the cost and production time for such lattice arrays.

## **STATEMENTS TO DEFENCE**

- The strong coupling regime implies that it is always enough to directly excite only one plasmonic branch for the hybrid polaritonic mode to be generated, because both plasmonic branches in hybrid state are inextricably linked with each other.
- The strong coupling between the TPP and SPP reduces the metal (gold, silver) losses and narrows the plasmonic resonances, thus, leads to higher optical signal sensitivity for refractive index changes on the sensing surface.
- The 1D plasmonic-nanophotonic structures supporting TPPs and cavity modes fabricated on the standard QCM sensor chip enhance the optical response of ellipsometric parameters  $\Psi(\lambda)$  and  $\Delta(\lambda)$  in the combinatorial SE-QCM method.
- The fabrication of large-scale lattice arrays of gold microbumps employing cost-effective direct laser writing technique enables to support

ultra-narrow hybrid lattice plasmonic surface resonances with reduced losses and tunable dispersion properties.

### **Structure of the dissertation**

The thesis is divided into four main chapters: the introduction, literature overview, methods and results. In the introduction section the motivation, tasks and scientific statements of the research are presented. The literature overview is divided into three parts, where strong coupling effect, nanophotonic structures and plasmonic excitations are discussed. Further in Chapter 3 the methods used in this research, such as ellipsometry, direct laser writing and protein layer formation are presented.

The chapter 4 is divided into 5 parts and covers the main results of the thesis. In the first part the results of strong coupling in hybrid Tamm – surface plasmon polaritons mode are presented, while in the second part the graphene monolayer influence on the strong coupling is demonstrated. The third and fourth parts, respectively, covers the hybrid Tamm – surface plasmon polaritons and Tamm plasmon polaritons application for enhanced biosensing. In the fifth section a hybrid lattice plasmon polaritons modes that are generated on gold microbump arrays, are presented.

At the end of the thesis the main conclusions (Chapter 5) of this research, summary in Lithuanian (Chapter 6) and references are presented.

### **List of scientific publications**

- P1. E. Bužavaitė-Vertelienė, V. Vertelis and Z. Balevičius. "The experimental evidence of a strong coupling regime in the hybrid Tamm plasmon-surface plasmon polariton mode", *Nanophotonics* **10**, 1565-1571, (2021). (IF=7.923)
- P2. E. Buzavaite-Verteliene, A. Valavicius, L. Grineviciute, T. Tolenis, R. Lukose, G. Niaura, Z. Balevicius, "Influence of the graphene layer on the strong coupling in the hybrid Tamm-plasmon polariton mode", *Optics Express* **28**, 10308-10319, (2020). (IF=3.833)
- P3. E. Buzavaite-Verteliene, I. Plikusiene, T. Tolenis, A. Valavicius, J. Anulyte, A. Ramanavicius, and Z. Balevicius, "Hybrid Tamm-surface plasmon polariton mode for highly sensitive detection of protein interactions", *Optics Express* **28**, 29033-29043, (2020). (IF=3.833)
- P4. I. Plikusiene, E. Bužavaitė-Vertelienė, V. Mačiulis, A. Valavičius, A. Ramanavičienė, Z. Balevičius, „Application of Tamm plasmon and cavity modes for biosensing in the combined spectroscopic ellipsometry

and quartz crystal microbalance method“, *Biosensors* **11**, 501, (2022). (IF=5.743)

- P5. E. Stankevičius, K. Vilkevičius, M. Gedvilas, E. Bužavaitė-Vertelienė, A. Selskis, Z. Balevičius, “Direct Laser Writing for the Formation of Large-Scale Gold Microbumps Arrays Generating Hybrid Lattice Plasmon Polaritons in Vis–NIR Range”. *Advanced Optical Materials* **9**, 2100027, (2021). (IF=10.050)

### **Other publications during this PhD**

- P6. E. Bužavaitė-Vertelienė, V. Maciulis, J. Anulytė, T. Tolenis, A. Baškys, I. Plikusiene, Z. Balevičius, “Total Internal Reflection Ellipsometry Approach for Bloch Surface Waves Biosensing Applications”, *Biosensors* **12**(8), 584, (2022). (IF=5.743)
- P7. I. Plikusiene, V. Maciulis, A. Ramanaviciene, Z. Balevicius, E. Buzavaite-Verteliene, E. Ciplys, R. Slibinskas, M. Simanavicius, A. Zvirbliene, A. Ramanavicius, “Evaluation of kinetics and thermodynamics of interaction between immobilized SARS-CoV-2 nucleoprotein and specific antibodies by total internal reflection ellipsometry”, *Journal of Colloid and Interface Science* **594**, (2021), 195-203. (IF=9.965)
- P8. G. Mickiene, I. Dalgėdienė, G. Zvirblis, Z. Dapkunas, I. Plikusiene, E. Buzavaite-Verteliene, Z. Balevicius, A. Rukšėnaitė, M. Pleckaityte, “Human granulocyte-colony stimulating factor (G-CSF)/stem cell factor (SCF) fusion proteins: design, characterization and activity”, *PeerJ* **8**, (2020) e9788. (IF=3.060)

### **Conferences**

- C1. E. Buzavaite-Verteliene, T. Tolenis, A. Valavicius, M. Narkauskaite, Z. Balevicius, Excitation of Bloch surface waves in periodic structures using spectroscopic ellipsometry, *62<sup>nd</sup> International conference for students of physics and natural sciences “Open Readings”*, Vilnius, Lithuania (2019). (poster)
- C2. E. Bužavaitė-Vertelienė, S. Tumėnas, T. Tolenis, A. Valavičius, R. Lukošė, Z. Balevičius, “Study of hybrid Tamm-plasmon polaritons mode by total internal reflection ellipsometry”, *8<sup>th</sup> International conference on spectroscopic ellipsometry (ICSE8)*, Barcelona, Spain (2019). (poster)
- C3. I. Plikusienė, E. Bužavaitė-Vertelienė, J. Talbot, T. Tolenis, A. Valavičius, A. Ramanavičius, A. Mickienė, Z. Balevičius, “Total internal



- reflection ellipsometry of hybrid Tamm – plasmon polaritons mode for biosensing application”, *8<sup>th</sup> International conference on spectroscopic ellipsometry (ICSE8)*, Barcelona, Spain (2019). (poster)
- C4. V. Grasyte, E. Buzavaite-Verteliene, Z. Balevicius, “Dispersion relation analysis of Bloch surface waves and surface plasmon polaritons using total internal reflection ellipsometry”, *63rd International conference for students of physics and natural sciences “Open Readings”*, Vilnius, Lithuania (2020) (canceled due to COVID-19). (poster)
- C5. V. Gradauskas, J. Anulytė, E. Bužavaitė-Vertelienė, I. Plikusienė, Z. Balevičius, “(In-situ) study of immobilized receptor binding kinetics by using planar photonic-plasmonic nanostructures for biosensing” *64<sup>th</sup> International conference for students of physics and natural sciences “Open readings”*, Vilnius, Lithuania (2021). (poster)
- C6. I. Plikusiene, E. Buzavaite-Verteliene, A. Lisaviciute, G. Mickiene, V. Maciulis, J. Talbot, Z. Balevicius, G. Zvirblis, S. Balevicius, A. Ramanavicius, “Label –free ellipsometric immunosensors based on interaction of genetically engineered ligands with different chimeric receptors”, *31<sup>st</sup> World Congress on Biosensors “Biosensors 2021”*, Online (2021). (poster)
- C7. E. Bužavaitė-Vertelienė, V. Vertelis, Z. Balevičius, „Evidence of a strong coupling regime in a photonic-plasmonic structure supporting hybrid Tamm-surface plasmon polaritons“, *23<sup>rd</sup> International Conference-School „Advanced Materials and Technologies 2021“*, Palanga, Lithuania (2021). (poster)
- C8. J. Anulytė, E. Bužavaitė-Vertelienė, I. Plikusienė, Z. Balevičius, „Hybrid Tamm-surface plasmon polaritons mode based on planar plasmonic photonic nanostructures for highly sensitive real time biosensing of GCSF and BSA proteins“, *23<sup>rd</sup> International Conference-School „Advanced Materials and Technologies 2021“*, Palanga, Lithuania (2021). (poster)
- C9. E. Bužavaitė-Vertelienė, I. Plikusienė, V. Mačiulis, A. Valavičius, A. Ramanavičienė, Z. Balevičius, „Tamm plasmons and cavity modes for biosensing application in a combined spectroscopic ellipsometry and quartz crystal microbalance method“, *65<sup>th</sup> International conference for students of physics and natural sciences “Open readings”*, Vilnius, Lithuania (2022). (oral)

## **Authors contribution**

The author of this dissertation performed ellipsometry measurements in all the experiments presented in scientific publications of this thesis, as well as participated in Raman spectroscopy measurements of the graphene layer used for strong coupling between Tamm plasmon-surface plasmon polaritons evaluation. The *in-situ* biosensing experiments, as well as preparation of the samples and protein immobilization process was also performed by the author. The manuscripts of 1, 2, 3 publications were prepared by the author and participated in preparation of 4, 5 as well as in reviewing process.

## 2 LITERATURE OVERVIEW

### 2.1 Strong coupling between two harmonic oscillators

In recent decades much attention has been paid to coupling in light-matter interaction systems, especially for strong coupling between them. Strong coupling is a phenomenon appearing between two (or more) oscillators, where the interaction between the modes is strong enough in a way that the energy levels of these modes are altered, compared to the single oscillators. Modes in strong coupling regime are called hybrid modes and appear in various systems [8,21–24], however, plenty of optical systems, such as atoms in cavities [25] has been investigated. When analyzing harmonic oscillator systems and coupling between them, these two or more oscillators must be able to exchange energy in order to be coupled. The energy of such systems becomes modified as new hybrid modes with different frequencies (compared to initial ones) are created. The frequency shift and the efficiency of energy exchange between them is determined by the strength of the coupling. Much attention has been paid for research on strong coupling between surface plasmon polaritons and excitons [2,4–6,26]. Strong coupling is an attractive phenomenon due to its possible applications in development of plasmonic

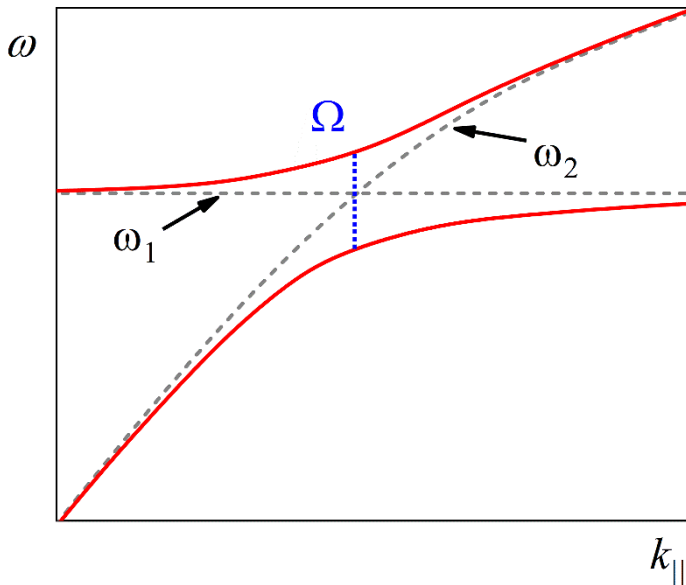


**Figure 2.1.1.** Strong coupling of two oscillator modes. The  $\omega_1$  and  $\omega_2$  are the initial frequencies of the modes marked as dashed lines, while the newly formed hybrid modes are marked as red lines.

lasers (SPASER) [27,28], integrated photonic devices [29,30] and control of chemical reactions [11,31].

Coupling between the two oscillators is usually described by the frequency shift  $\delta\omega$  from the initial  $\omega_0$  value. Each of these oscillators have their initial frequencies (Fig. 2.1.1 dashed line) that for light-matter interaction are either dispersive or non-dispersive. Given the right conditions their energies can overlap. However, the coupling strength (if strong or weak coupling regime operates) of the oscillators and the ability to couple is determined by the oscillator decay rates. If the coupling strength between two oscillators of the same energy exceeds their decay rates, the system is then strongly coupled and the system energy states split - new modes are created with a gap near the anti-crossing energy (Fig. 2.1.1 solid lines). The splitting between these two modes is called the Rabi gap or Rabi splitting ( $\Omega$ ) and it appears between an excited atom (or similar two-level system, such as quantum dots) and a cavity (resonator) [32]. When a quantum dot is embedded in a cavity, the cavity directs the emission into a single mode and reduces the lifetime of spontaneous emission [33], thus coupling depend on the resonance quality factor  $Q$  and volume ( $V$ ) ratio. The Rabi splitting can be written as [17]:

$$\Omega_R = \mu \sqrt{\frac{2\omega_0 N}{\epsilon V}}, \quad (2.1)$$

where  $N$  is the number of molecules/atoms in a volume  $V$ ,  $\epsilon$  is the dielectric permittivity of the medium,  $\omega_0$  is the resonant frequency and  $\mu$  is the dipole moment. Coupling in cavity modes can be enhanced by reducing the volume and increasing  $Q$ . However, the quality factor is dependent on the linewidth of the modes that vary based on losses due to emitter damping ( $\gamma$ ) and the light extinction in the cavity ( $\kappa$ ). Generally, the strong coupling parameter  $g$  should satisfy the condition  $g > \gamma, \kappa$  [33]. Various cavity structures, such as photonic crystals, micropillars and microdisks [34–36], microspheres [37] were used for investigation of strong coupling between the cavity modes and quantum emitters.

In coupled systems, the boundary between the weak and strong coupling regimes depends on the system itself. The damping plays a significant role, as the oscillators with larger damping than coupling between them approach the initial frequency value. In this case the coupling effect is negligible. In high frequency (optical) systems, the strong coupling is described as a significant frequency shift compared to the linewidth of the oscillator. Thus, from the experimental point of view, if the observed dispersion curves of the oscillators

(energy dependence on wave vector) are hardly indistinguishable, the system is in weak coupling. If the curves can be identified as separate modes, the strong coupling regime is present. However, the damping effect on the strong coupling should not be forgotten, as it reduces the size of the Rabi splitting. Thus, strict statement of “split size larger than width” in strong coupling context should be used more loosely as the width of oscillators can be a bit larger than the splitting. The newly created mode’s resonance at the anti-crossing point can be written as:

$$\omega_{\pm} = \frac{1}{2}(\omega_1 + \omega_2) - \frac{1}{4}i(\gamma_1 + \gamma_2) \pm \Omega_R, \quad (2.2)$$

where  $\omega_1$  and  $\omega_2$  are the frequencies of the oscillators and  $\gamma_1, \gamma_2$  – damping rates. The Rabi splitting can be rewritten as the frequency at which the energy between two modes oscillate [38]:

$$\Omega_R = \frac{1}{2} \sqrt{g^2 + (\omega_1 - \omega_2)^2 - \frac{1}{4}(\gamma_1 - \gamma_2)^2}. \quad (2.3)$$

Here the parameter  $g$  represents the coupling strength between the oscillators. Thus, the condition for the strong coupling regime between two oscillators (in this case plasmon and exciton) based on work done by Pelton et al. [38] must satisfy the condition:

$$g > \frac{1}{4}(\gamma_1 - \gamma_2). \quad (2.4)$$

If the damping between two (or more) oscillators exceeds the coupling strength, the oscillators approach the original frequency values. This is an important feature, as one of the strong coupling conditions is the coherence between the oscillators. The strong light-matter interaction between the surface plasmon polaritons (SPP) (see section 2.3.2) and the organic dye molecule excitons that are attractive due to a large (approx. 100-300 meV) Rabi splitting [39–41] compared to those achieved in inorganic semiconductors [42]. Excitons can be coupled to the SPPs in the near-field if the wave vector matching is realized, thus, the coupling depends on the distance between the dye molecule and metal surface. However, if the molecule is too close to the metal’s surface, the energy of the emitter will dissipate in the metal. As a result, an optimal distance between the emitter and

the metal surface is needed (typically 10-20 nm) [1]. In SPPs, the coherence decays faster due to the dissipative nature of surface plasmon polaritons, thus, few Rabi oscillations occur before the phase matching is lost (~10-100 fs) [43]. Since, losses experienced by surface plasmon polaritons due to metals is the main limiting factor for the strong coupling, various plasmonic excitations are being looked into in order to reduce this problem. One of such solutions is the use of long-range surface plasmon polaritons (LRSP) that have large (up to 250  $\mu\text{m}$ ) propagation length. The LRSPs are surface modes appearing in thin metal layer surrounded by dielectric. When the thickness of the metal layer is of the order of 10-20 nm, the plasmonic modes at two metal/dielectric interfaces can interact with each other and create hybrid modes. In order to achieve maximum coupling between these two modes, the wave vectors and the energies of these two plasmons has to be matched, thus, system has to be symmetrical. [44]. Strong coupling effects can be observed between long range surface plasmons and excitons [45,46]. In one case a thin silver slab (20 nm thick) with thin spin-coated J-aggregate layer is embedded in poly(vinyl alcohol) and the strong coupling of 120 meV magnitude is observed [46]. Another plasmonic coupling example with significant reduction of losses is the surface lattice plasmon resonances (SLPR) [47]. In SLPR samples the coupling is achieved by interaction between two nanoparticles that are matched in phase with the incident light due to periodic arrangement of the array and as a result compensates the energy losses in metal. The resonance of one nanoparticle affects the resonances of neighboring nanoparticles, thus enhancing the quality factor Q of the SLPR [48].

As the coupling between high frequency oscillators are extensively investigated, the analysis of the strong coupling in hybrid Tamm plasmons-surface plasmon polaritons (TPP-SPP) have not been extensively researched. First report of hybrid TPP-SPP modes were presented in the work done by Afinogenov et al. [18], where they show the dependence of the curves repulsion on the metal layer thickness. However, it has not been named as strong or weak coupling. The ability to control the coupling strength between plasmonic excitations, such as TPP-SPP modes or similar hybrid plasmonic modes, would allow to improve the quality and sensitivity of hybrid plasmon based sensors [49]. The investigation of strong coupling in hybrid plasmonic nanophotonic structures would benefit in control of chemical reactions and photo-bleaching in fluorescent biomarkers [31,50].

## 2.2 1D photonic crystals

For further analysis of hybrid plasmonic modes discussed in section 2.3, a concept of photonic crystals should be overviewed. Such structures are attractive due to their optical properties as well as cheap cost-effective manufacturing. Such easy control of forbidden band gap engineering influences optical properties of plasmonic resonances that can be generated in such structures. Also, these structures are widely used as optical filters [51], waveguides [52], antennas [53] and other applications [54].

Photonic crystals (PCs) are special, due to their feature to inhibit certain light frequencies from propagation in different geometrical configurations. They are synthetically produced macroscopic media derived from materials arranged in periodic structures (e. g. multilayer stack, layer with holes, synthetic or natural opals). Depending on the formed structure, thus, light propagation direction, the PCs are divided in 1D, 2D and 3D categories. These periodic structures under special conditions can forbid propagation of specific frequencies from propagation through the structure, forming a photonic band gap (PBG). It is a similar analogy as with energy band gaps for electrons in crystal structures, where electrons travelling in atom lattice are modulated by the periodic potential of the atoms. Similarly, photons are affected by the periodically changing dielectric function of PC, thus creating a PBG. If the photons energy falls into the forbidden range, the photon cannot pass through the photonic crystal in specific directions. These energies depend on the dielectric functions of the materials and on the lattice constant of the PC – wavelengths of incident photons must be similar to the period in order to fall in the PBG.

Here, the simplest case of 1D PC will be discussed. One of the first analysis of optical multilayer stack properties were discussed by Rayleigh [55]. When light is traveling through a multilayer periodic stack (Fig. 2.2.1 left), part of that light is reflected and part of it is transmitted at each interface. Due to the periodicity, the multiple reflected and forward beams interfere destructively eliminating forward propagating wave. Such reflective 1D PC structures are sometimes also referred to as Bragg mirrors. If the number of periods ( $a$ ) is large enough, the reflectivity of such structure becomes almost equal to unity. The formation of PBG can also be explained from the crystal structure perspective. In 1D PC structures the refractive index distribution is homogeneous in the  $xy$  plane and periodically changes in the  $z$  direction. Thus, incident light has different wave vectors: in-plane and perpendicular components  $k_{||}$  and  $k_z$ , respectively. Since the  $xy$  plane is homogenous, the wave vector  $k_{||}$  can have any value, however,  $k_z$  has finite interval of 1D

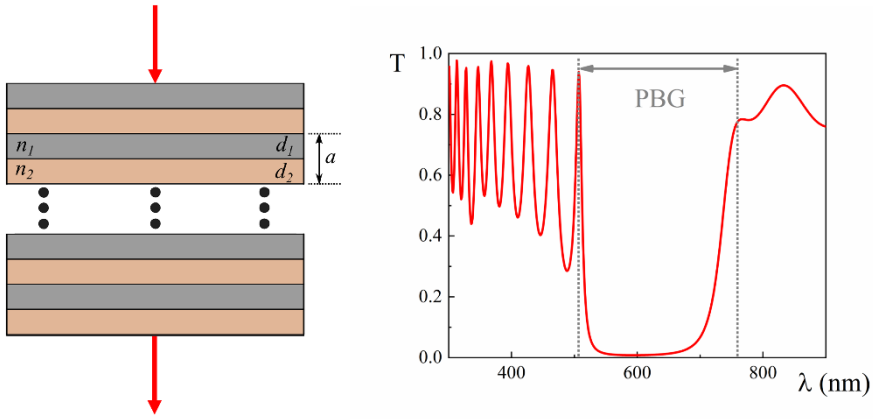


**Figure 2.2.1.** The schematic structure of 1D photonic crystal (left) and the transmission spectra of light after passing through the PC structure (right).

Brillouin zone values due to translational symmetry in  $z$  direction [56]. If the multilayered structure refractive index (RI) contrast is large enough, a frequency gap forms that experimentally can be seen as transmission intensity drop to 0 (Fig. 2.2.1 right). This means that regardless of the value of wave vector  $k_z$ , the frequencies in the PBG are not allowed to be transmitted.

With the increase of the RI contrast, the gap widens and width of the gap depends on thicknesses of layers as the reflected waves from each layer must be in phase. The central wavelength ( $\lambda_c$ ) and the width of the PBG ( $\Delta\lambda$ ) can be calculated from equations [54]:

$$m\lambda_c = 2a \sqrt{n_{eff}^2 - \sin^2 \theta}, \quad (2.5)$$

$$\Delta\lambda = \frac{4}{\pi} \lambda_c \left| \frac{n_2 - n_1}{n_2 + n_1} \right|, \quad (2.6)$$

where  $m$  is an integer,  $n_{eff}$  is the effective refractive index and  $\theta$  is the angle of incidence (AOI).

Though, the photons are not allowed to travel through the PC structure if its energy falls into the PBG, there are cases when specific energies are permitted within the PBG. For example, by using 1D PCs with more than two different RI layers, thus defective states can appear [57]. One of such crystal defect case will be discussed further in 2.3.1 section.



## 2.3 Plasmonic excitations

Surface electromagnetic waves (SEW) are of great interest in various applications such as sensors [58–61], integrated optics, lasing [62,63] and so on [64,65]. These types of waves are confined at the boundary between two different media. Due to field localization, SEW, such as plasmonic resonances, are extensively researched and as a result are of great interest due to their applications [66–68].

When incident light impinges on a plasmonic surface (thin metal layer or metal nanostructures), due to free charge fluctuations, resonant modes can appear. If the wave vector matching conditions for the incident light and free surface carrier oscillations are met (energy, angle of incidence, geometry of the structure and refractive index) surface waves, called plasmon polaritons can appear. Plasmonic surface waves are coupled polaritonic modes, where electromagnetic field (light) interacts with electric or magnetic dipole excitation. For the wave propagating from one medium to other, the wave vector in the second media is frequency dependent ( $k = \omega\sqrt{\varepsilon(\omega)}/c$ ), thus, such polaritonic modes can propagate in medium if  $\varepsilon(\omega) > 0$  at  $\omega$  frequency. However, in some materials there are frequency ranges, where  $\varepsilon(\omega) < 0$ , such as metals and semiconductors below plasma frequency, where the wave vector is imaginary due to evanescent wave nature. As a result, such waves have only the evanescent part penetrating into second material and a solution of Maxwell's equations exist for wave vector parallel to the interface of the two materials. This solution of Maxwell's equation is the surface polariton (surface electromagnetic wave).

In this Chapter plasmonic surface polaritons – the Tamm plasmon polaritons (TPP), surface plasmon polaritons (SPP), hybrid TPP-SPP modes and hybrid lattice plasmon polaritons (HLPP) and their features will be discussed.

### 2.3.1 Tamm plasmon polaritons

As mentioned in section 2.2, when a defect is introduced in PC structure, a defect state can be created within the PBG [69], allowing propagation of specific energy photons. One of such cases is the optical Tamm state (OTS) appearing in structures containing two dielectric Bragg mirrors with different lattice periods [70,71]. These optical Tamm states are an analogy to the electron states at the crystal surface proposed by I. Tamm [72] that can occur in the energy band gap. However, these optical states can appear only at the interface between the two PCs with overlapping PBGs and OTS lies in the

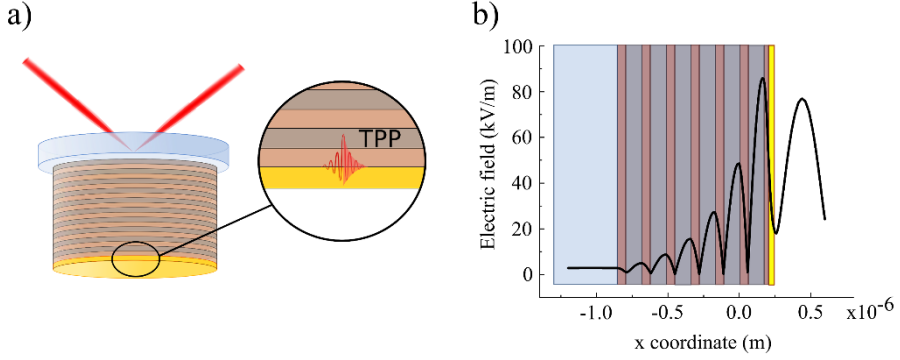


**Figure 2.3.1.** The TPP excitation scheme (a) and the electric field distribution in the 1D PC/metal structure (b).

overlapped PBG of the PCs. These modes are special due to their dispersion that lies inside the light cone, thus allowing direct excitation. However, such structures must be produced precise, so that the PBGs would overlap and OTS would be excited. Another way to excite optical Tamm states is by using a 1D PC with thin metal layer which can be used to generate Tamm plasmon polaritons at the 1D PC and metal boundary that were first experimentally observed by M. E. Sasin et al. [73].

Tamm plasmon polariton surface electromagnetic waves appearing at the boundary of 1D PC (also called Bragg mirror) and a metal that can be directly excited with light (Fig. 2.3.1 a). The Bragg mirror consist of layers A and B with thickness  $d_1$ ,  $d_2$  and refractive index  $n_1$ ,  $n_2$ , respectively, so that  $n_1 d_1 = n_2 d_2 = \pi c/2\omega_{Br}$ , where  $\omega_{Br}$  is the Bragg frequency. If the oscillations of the modes created in a Bragg/metal structure are of the same (or nearly the same) frequency, the resonant frequency conditions for TPP excitation are met. For this reason, the normal modes can be imagined as two reflections at the metal's and A layer's interface that counter propagate. The field for the resonant mode can be written using transfer matrix method through the two counter propagating reflections:

$$C \begin{pmatrix} 1 \\ r_{\leftarrow} \end{pmatrix} = \begin{pmatrix} \exp i\Phi & 1 \\ 1 & \exp -i\Phi \end{pmatrix} \begin{pmatrix} r_{\rightarrow} \\ 1 \end{pmatrix}, \quad (2.7)$$

where  $C$  is a constant,  $r_{\leftarrow}$  and  $r_{\rightarrow}$  are the left and right propagating waves, respectively, and  $\Phi$  is the phase change of the wave propagating from one interface to the other. The electric field in PC/metal structure (Fig. 2.3.1 b) is enhanced at the PC and metal interface. By eliminating  $C$ , we get:

$$r_{\leftarrow} r_{\rightarrow} \exp 2i\Phi = 1. \quad (2.8)$$

Since the boundary for both waves is the same, the phase difference here is equal to 0, as there is no distance to propagate. The reflection amplitudes can be rewritten as  $r_M$  – coefficients for wave incident on the metal from the A layer of the PC and  $r_{Br}$  – coefficient for the wave incident from layer A to the Bragg mirror. Then from Eq. 2.8 the condition for the resonant mode at metal/A layer interface becomes:

$$r_M r_{Br} = 1. \quad (2.9)$$

The reflection amplitudes of  $r_M$  and  $r_{Br}$  is given by:

$$r_M = \frac{n_1 - n_M}{n_1 + n_M}, \quad (2.10)$$

$$r_{Br} = \pm e^{\frac{i\beta(\omega - \omega_{Br})}{\omega_{Br}}}, \quad (2.11)$$

where  $n_M$  in Eq. 2.10 and Eq. 2.11 is the metal's refractive index, the – sign is for the  $n_1 > n_2$  case and + sign is  $n_1 < n_2$  case and  $\beta = \pi n_1 / |n_1 - n_2|$ . For the  $n_1 > n_2$ , the resonant frequency can be written as [74]:

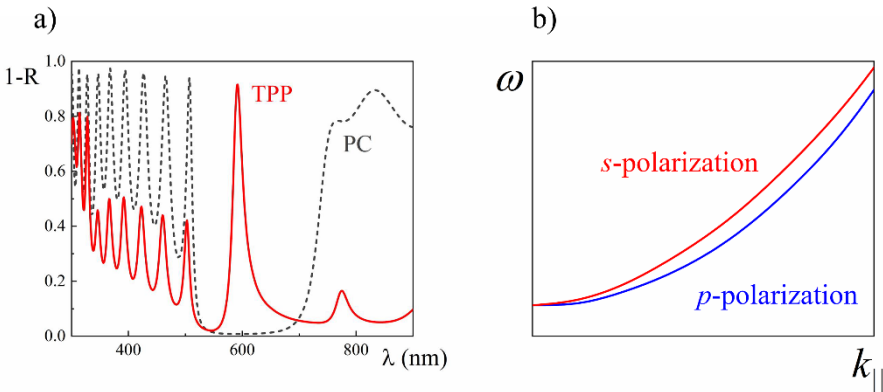


**Figure 2.3.2.** The optical response of the Tamm plasmon polaritons (a), where the TPP mode appears in the PBG, and the dispersion of TPP for both p- and s-polarization states (b).

$$\omega_{TPP} \approx \frac{\omega_{Br}}{1 + \frac{2n_1\omega_{Br}}{n_a\beta\omega_p}}, \quad (2.12)$$

where  $n_a$  is the ambient RI and  $\omega_p$  is the metals plasma frequency.

The TPP mode can be generated in both transverse electric (TE) and transverse magnetic (TM) polarization states that appears in PBG (Fig. 2.3.2 a) and its in-plane dispersion is parabolic (Fig. 2.3.2 b). The splitting between TE and TM polarization states increase quadratically with the in-plane wave vector [74].

Tamm plasmons were applied for sensing [75–78] and lasing [79] due to their low losses and direct excitation with light. It has been theoretically [80,81] and experimentally [82] shown that optical Tamm states and Tamm plasmons can be in strong coupling with excitons. Various structures, suitable for Tamm plasmon lasers that confines the field has been investigated by [83–85].

### 2.3.2 Surface plasmon polaritons

Surface plasmon polaritons became attractive due to their potential applications for medicine and chemistry [59,86–88], photonic devices [9,63,89,90], subwavelength optics [91,92] and photonics for electronic circuit elements [93–95].

Surface plasmon polaritons (SPP, also often referred as surface plasmons) are optical surface electromagnetic waves generated at the metal/dielectric boundary when an electromagnetic field interacts with resonance of conduction electrons at the metal's (or n-type semiconductor's) surface. In order to analyze such light matter interaction let's consider TM polarization light incident from dielectric medium to metal. Such interaction can be derived from Maxwell's equations with boundary condition  $k_d/k_m = -\varepsilon_d/\varepsilon_m$ , where  $k_d$  and  $k_m$  are components of wave vector perpendicular to the interface in the dielectric and metal, respectively. From the boundary conditions one can obtain the dispersion relation for the SPP wave:

$$k_{SPP} = \frac{\omega}{c} \sqrt{\frac{\varepsilon_m \varepsilon_d}{\varepsilon_m + \varepsilon_d}}. \quad (2.13)$$

The solutions of Maxwell's equations for electric field perpendicular to the interface take form of evanescent decay in both, dielectric and metal media.

The  $\epsilon_m$  is a complex number, thus, the SPP wave vector is as well complex due to absorbing nature of metals. Then the wavelength of the SPP  $\lambda_{SPP}$  is inversely proportional to  $k_{SPP}$ . The penetration depth of the electric field into the dielectric ( $\delta_d$ ) and metal ( $\delta_m$ ) materials can be derived from  $k_d$  and  $k_m$  and can be written as [96]:

$$\delta_d = \frac{1}{k_d} = \frac{\lambda}{2\pi} \sqrt{\frac{\epsilon_d + \epsilon_m}{-\epsilon_d^2}}, \quad (2.14)$$

$$\delta_m = \frac{1}{k_m} = \frac{\lambda}{2\pi} \sqrt{\frac{\epsilon_d + \epsilon'_m}{-\epsilon_m^2}}. \quad (2.15)$$

However, when TE wave is considered, there is no solution to the Maxwell's equations and SPP cannot exist in this polarization. If  $k_{SPP} \rightarrow \infty$ , the dispersion curve approaches plasma frequency ( $\omega_p$ ) value (Fig. 2.3.3). The size (modulus) of the SPP wave vector ( $k_{SPP}$ ) is always larger than the wave vector of free space, thus the wave vector component of incident light that is parallel to the interface is not enough to excite the  $k_{SPP}$  at any angle of incidence. Thus,

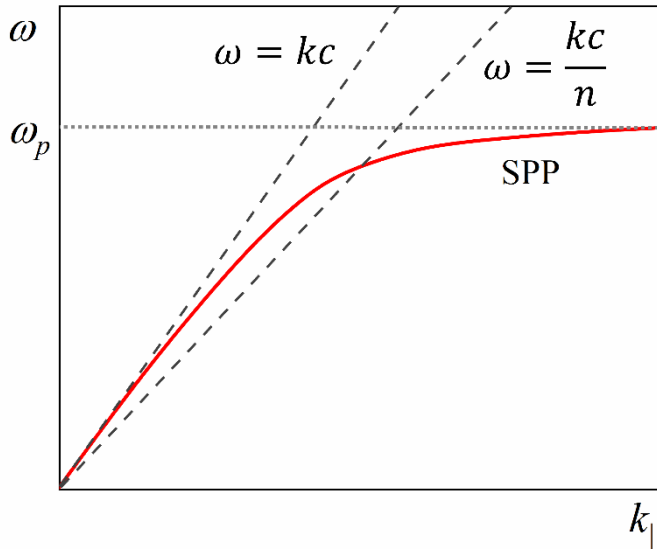


**Figure 2.3.3.** Surface plasmon polariton dispersion relation. Where  $\omega = kc$  is the light cone in vacuum and  $\omega = kc/n$  is the light dispersion in prism coupler.

the surface plasmons are non-radiative modes propagating along the interface. The SPP wave will travel along the interface until the energy will dissipate as heat in metal. And the propagation length can reach up to the order of cm [93].

The dispersion of SPP (Fig. 2.3.3) lies below the plasma frequency, thus in order to achieve wave vector matching conditions, the incident light wave vector component parallel to the interface must be increased. There are few optical configurations that can be used to achieve wave vector matching condition. The most commonly used mechanisms for light coupling to surface plasmons are the prism ( $n > 1$ ) and grating. When a prism is used there are two geometries used: Otto [97] and Kretschmann [98] (Fig. 2.3.4). In Otto configuration (Fig. 2.3.4 left), the prism is introduced near the metals surface, however, there is a gap between the prism base and metal layer. Duo to prism higher refractive index, compared to free space, the wave vector of incident light becomes:

$$k = \frac{\omega}{c} n_p \sin \theta_i , \quad (2.16)$$

where  $\theta_i$  is the angle of incidence and  $n_p$  is prism refractive index. Due to total internal reflection, the field of surface wave at the prism base can only transfer its energy and excite SPP if the distance is of the order of penetration depth in dielectrics. And the SPP is generated at the metal/dielectric interface at the inner side – between prism and metal. Because of the small gap between the prism base and metal, the Otto geometry are less practical in sensing applications. For this reason, another configuration – Kretschmann (Fig. 2.3.4 center) can be used, as it is more applicable. In this type of geometry, thin metal film (~on the order of few tens of nm) is directly deposited on prism base. The electric field from the base of the prism penetrates through metal and thus is excited at the outer side – between metal and ambient. The Kretschmann geometry is often used for surface plasmon sensing applications, especially in liquid ambient. However, the use of prisms is not very suitable in the development of nano-optics components. This can be solved by SPP excitation via grating (Fig. 2.3.4 right). If the metal surface is formed so that there are grooves of period  $a$ , the light incident upon the grating will satisfy the wave matching condition if:

$$k_{SPP} = k_0 n \sin \theta_i \pm \frac{2\pi m}{a} , \quad (2.17)$$

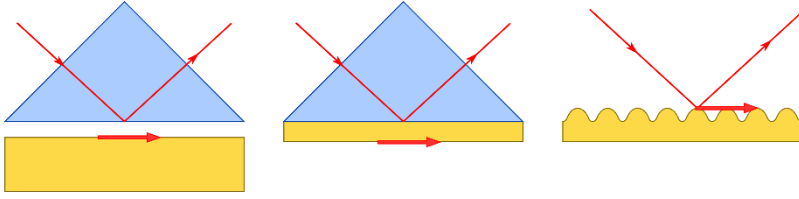


**Figure 2.3.4.** The SPP excitation configurations using prism coupler: Otto (left), Kretschmann (center), and grating (right).

where  $m$  is an integer and  $n$  is the refractive index of the ambient.

Surface plasmons compared to the Tamm plasmons, discussed in 2.3.1 section, have higher sensitivity to refractive index changes, due to the direct SPP contact with the ambient material. For this reason, they are more widely used in sensing applications. However, surface plasmons have lower quality factor than TPP, because of higher SPP losses due to absorption in metal, rather than in TPP.

### 2.3.3 Hybrid Tamm plasmon-surface plasmon polaritons

The energy losses in plasmonic excitations (such as SPP) can be reduced by coupling it to another plasmonic excitation [99], either of the same or different origin. By introducing specific conditions, strong coupling regime

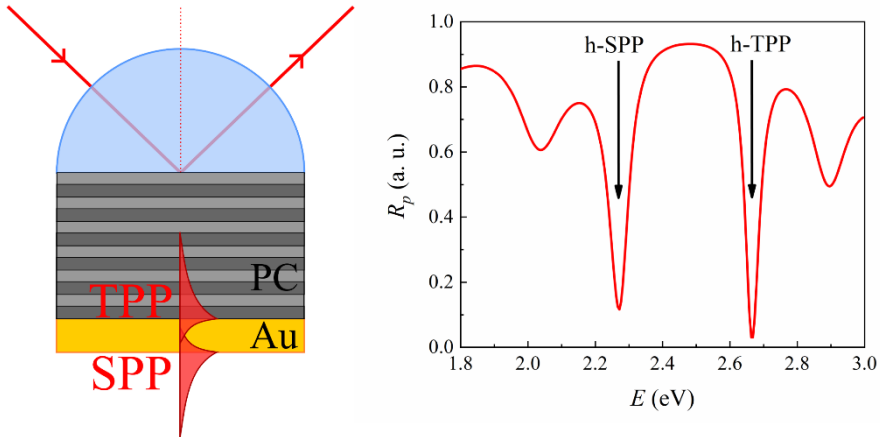


**Figure 2.3.5.** The excitation configuration of the hybrid Tamm plasmon-surface plasmon polaritons (left) and the p-polarization reflection spectra (right).

can be achieved. Here a hybrid Tamm plasmon polariton and surface plasmon polariton mode will be discussed.

Tamm plasmons–surface plasmon polaritons (TPP-SPP) are hybrid electromagnetic surface waves generated in 1D PC with thin metal layer structure under total internal reflection geometry. By combining the PC/metal structure, needed for TPP excitation, and prism, used for SPP excitation, one can generate a new hybrid TPP-SPP mode. Recently, these modes gained interest [100], especially in sensing applications [101,102,20].

The hybrid TPP-SPP optical response (Fig. 2.3.5 right) is excited using scheme presented in Fig. 2.3.5 left. Depending on the AOI the optical response of the structure changes. The dispersion curves (Fig. 2.3.6) of the hybrid mode do not coincide with dispersion of single modes. At the angles below TIR threshold, the dispersion of the TPP component in TPP-SPP mode it follows the single mode curve. With the increasing AOI, the energy of TPP component increases, due to diminishing of the perpendicular to the surface wave vector component, thus, the parallel component increase. The SPP

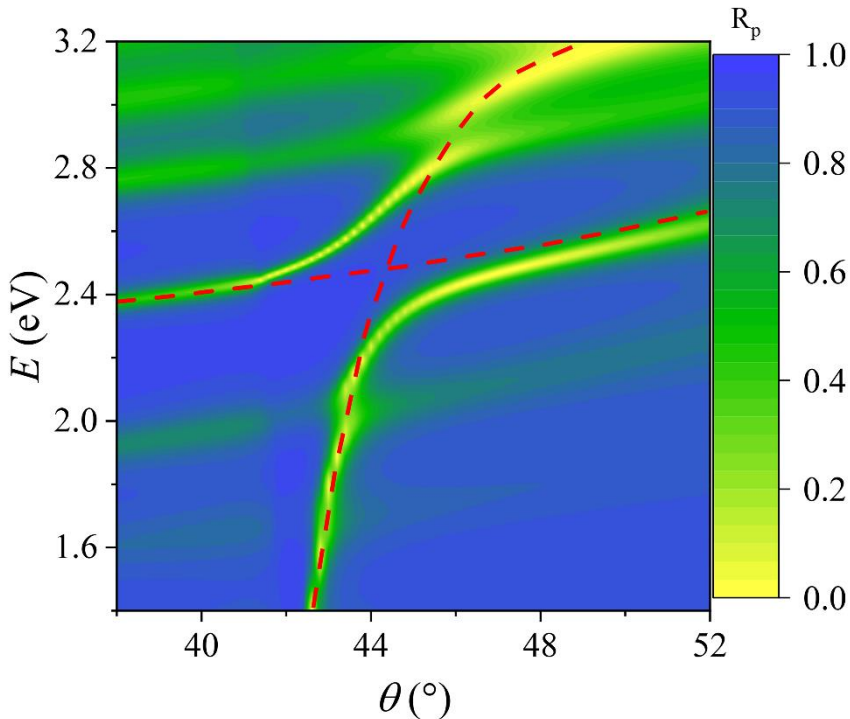


**Figure 2.3.6.** Dispersion relation of the hybrid Tamm plasmon-surface plasmon polaritons mode. The red dashed curves are the calculated single TPP and SPP modes.



component appears only when the TIR and wave vector matching conditions are reached. As the  $k$  increase, the SPP approaches the energy of the TPP, where eventually at specific energy and  $k$  values, both resonances should cross. However, the TPP and SPP components are shifted compared to their initial values. The dispersion curves then form a hybrid Tamm plasmon-surface plasmon polariton mode. It is important to mention that single SPP and TPP modes cannot be generated simultaneously in such structure under TIR, as the TPP-SPP is a mode created due to coupling between these two modes. The hybrid mode is determined by structure itself and the split between the two modes is restricted by the angle of incidence and the structure. However, it has been shown [20] that, by real time detection of mercury vapor one can have changes of the gap size between the two TPP-SPP excitation components because of the alteration of metal layer conductivity.

The first experimental observation of hybrid TPP-SPP states were done by Afinogenov et al. [18]. The repulsion of TPP and SPP in a hybrid mode was investigated, where authors demonstrated the splitting dependence on metal layer thickness. Due to repulsion between the curves, both, TPP and SPP components of the hybrid TPP-SPP mode, are pushed more into the dielectric and the energy losses due to metal are reduced. However, the coupling strength as a key factor of the splitting size between the modes in Ref. [18] is not mentioned. If the appropriate metal layer thickness and AOI are selected, the TPP and SPP components of the hybrid excitation satisfy the condition (Eq. 2.4) for the strong coupling regime.

It is important to analyze the coupling between plasmonic modes, as the strong coupling in such structures that support hybrid plasmonic excitations can be used for enhanced sensitivity detectors, as well as integrated photonic devices due to reduced energy losses. The aspects of strong coupling in hybrid TPP-SPP mode will be discussed in the research presented in this PhD thesis.

#### 2.3.4 Hybrid lattice plasmon polaritons

The reduced energy losses in plasmonic systems, such as hybrid TPP-SPP modes, are attractive due to their possible applications. However, if integrated photonics, plasmonic lasers or similar compact device applications are considered, the excitation using prisms becomes a non-compact method. For excitation of narrow coupled resonances, various periodic nanoparticle arrays, supporting plasmonic excitations, are considered and investigated [103,104]. The most recent are the surface lattice plasmon resonances (SLPR) and hybrid lattice plasmon polaritons (HLPP) that appear on a periodically arranged nanoparticle arrays.

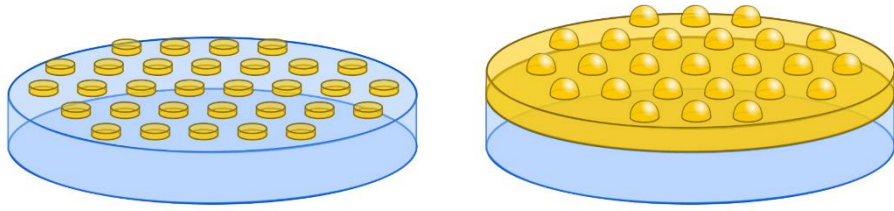


**Figure 2.3.7.** The schematic of the SLPR (left) and HLPP (right) array structures.

Surface lattice plasmon resonances are collective coupled local surface plasmons (LSP) generated on periodic nanoparticle lattices (Fig. 2.3.7 left), whose optical response can be altered by changing the shape, size and material of the nanostructure. When light is incident on a metal nanoparticle whose size is smaller than the light wavelength, the oscillating electromagnetic field drives the conduction electrons of the nanoparticle, thus creating resonance. Such coupling of light and free electrons is called local surface plasmons that manifests as wide (FWHM  $\sim 100$  nm) non-dispersive dip, whose width depends on the particle size and dielectric function of the metal and ambient. However, if the nanoparticles are arranged in an orderly manner, so that the period would be similar to the incident wavelength, the LSP excitations combined with Bragg reflections from the periodic lattice create the SLPR mode [47,105]. Due to small distance between nanoparticles, the near-fields of plasmon resonances can interact with each other and further confine the fields [106], thus compensating losses and as a result producing narrow resonance width ( $\sim 10$  nm) [48,104]. These types of nanoparticle arrays became of interest due to their possible application in plasmonic lasers [107–110].

The periodically arranged nanoparticle structures (gratings) rapid intensity variations of various diffracted spectral orders can appear, where such effects are called anomalies and was first discovered by Wood [111] and later described by Rayleigh [112] that manifested as narrow bands in the spectrum. These anomalies in spectra can be weakened or totally removed by reducing the depth of the groove. It has been noticed that the bands appear in *s* polarization ( $\mathbf{E}$  is perpendicular to the grating ripples) – called S anomalies, while P anomalies for the *p* polarization ( $\mathbf{E}$  is parallel to the grating), were later for deep grooves. Recently much attention has been paid to Rayleigh’s anomaly occurring in 2D arrays of either nanoholes [113,114] or nanoparticles [103,115]. Apart from anomalous effects, Bragg reflections can also appear in periodic structures, where Bragg modes can couple with surface plasmon polaritons. The Bragg coupling condition [113] in 2D array can be written as:

$$\text{Re} \left[ \frac{\omega}{c} \sqrt{\frac{\varepsilon_m \varepsilon_d}{\varepsilon_m + \varepsilon_d}} \right] = |\mathbf{k}_0 \sin \theta + i\mathbf{G}_x + j\mathbf{G}_y|, \quad (2.18)$$

where  $\omega$ ,  $c$  and  $\mathbf{k}_0$  are the frequency, speed and wave vector of free space light, and  $\varepsilon_d$  and  $\varepsilon_m$  are dielectric functions of ambient and metal, respectively. The  $\mathbf{G}_x$  and  $\mathbf{G}_y$  are the lattice wave vectors in x and y directions, while  $i$  and  $j$  denote the coupling mode number. The lattice wave vector  $\mathbf{G} = 2\pi/a$ . Under these conditions SPP wave is generated, however, Rayleigh anomalies can also occur. These anomalies appear when light is diffracted parallel to the grating surface (tangential propagation). Compared with the Bragg coupling condition, Rayleigh's anomaly does not depend on the metal dielectric function and only on ambient dielectric function and the grating geometry:

$$\frac{\omega}{c} \sqrt{\varepsilon_d} = |\mathbf{k}_0 \sin \theta + i\mathbf{G}_x + j\mathbf{G}_y|. \quad (2.18)$$

Nanoparticles for SLPR generation in visible spectral range can be produced using lithography method. However, the production of such structures is expensive and has low production area. For this reason, production of periodic structures on metal film can be replaced by using direct laser writing (DLW) [116,117]. It has been shown that by forming periodic arrays on metal films (by lithography) narrow resonances can also be generated [118]. These types of modes consist of coupling between surface plasmon polaritons and Bragg modes and are usually called lattice plasmon resonances, however, here it will be referred to as hybrid lattice plasmon polaritons (HLPP) (Fig. 2.3.7 right). Usually nanostructures, supporting HLPP, are produced by lithography if the optical response is expected in the visible range. On the contrary, laser applications, such as laser interference lithography can be used for creation of nanostructures [119] that as application for periodic nanostructure production would be cost effective, allowing production of large areas.

## 3 METHODS

### 3.1 Optical measurement methods

#### 3.1.1 Spectroscopic ellipsometry

Ellipsometry is an optical measurement method, used for characterization of thin film optical and structural properties by the changes of polarization state upon reflection from the samples surface. This method is often used for the determination of refractive index or thickness of thin films, especially in deposition techniques where precise real time measurements are needed [120–122].

If the incident electromagnetic is of known polarization, so that both p- and s-polarization components are present, the changes of reflected beam polarization state from the thin film will be measured. The measured quantities are ellipsometric angles  $\Psi$  and  $\Delta$  and they are defined by the reflection coefficients ratio of p- and s-polarization components [123]:

$$\rho = \frac{r_p}{r_s} = \tan \Psi e^{i\Delta}, \quad (3.1)$$

where  $r_p$  and  $r_s$  are the complex reflections p- and s-polarization components, expressed as:

$$r_p = \frac{n_t \cos \theta_i - n_i \cos \theta_t}{n_t \cos \theta_i + n_i \cos \theta_t}, \quad (3.2)$$

$$r_s = \frac{n_i \cos \theta_i - n_t \cos \theta_t}{n_i \cos \theta_i + n_t \cos \theta_t}. \quad (3.3)$$

In Eq. 3.2 and Eq. 3.3  $n$  is the refractive index and indices  $i$  and  $t$  marks the incident and transmitted beam, respectively. The ellipsometric angle  $\Psi$  characterizes the change in amplitude of both polarization components, while  $\Delta$  characterizes the phase difference between the p- and s-polarization components. Since the angle of  $\Psi$  is  $\tan^{-1}\Psi$ , the range of angle values are  $0^\circ < \Psi < 90^\circ$  and phase difference will have a range  $0^\circ < \Delta < 360^\circ$ . The preferred angle of incidence in SE measurements is the Brewster's angle, as the amplitude difference between the p- and s-polarization components is the largest.

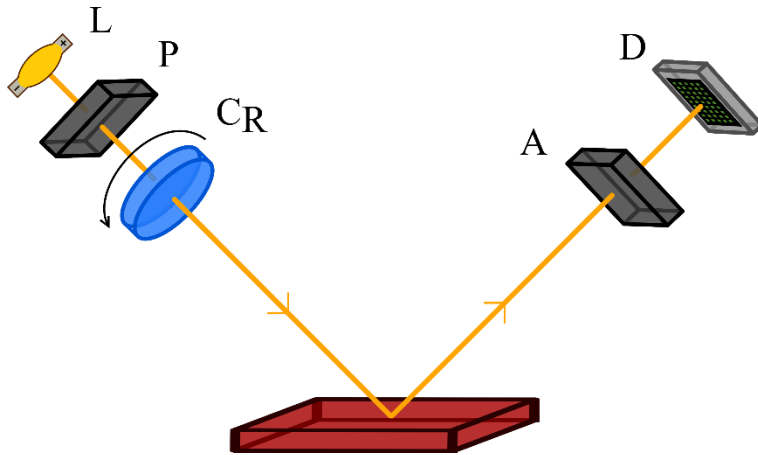


**Figure 3.1.1.** Schematic of spectroscopic ellipsometry measurement technique, where L is the light source, P – polarizer, C<sub>R</sub> – rotating compensator, A – analyzer and D – detector.

The principal scheme of spectroscopic ellipsometry measurements is presented in Fig. 3.1.1. The light coming from light source (L) becomes linearly polarized after passing through the polarizer (P) and then travels through a rotating compensator (C<sub>R</sub>), where the beam becomes elliptically polarized. After reflection from the sample, the reflected wave passes through analyzer (A) and then into detector (D), where the signal is registered.

### 3.1.2 Total internal reflection ellipsometry

A beam of light, incident on a boundary from a material with a higher refractive index  $n_1$  into a material with lower refractive index  $n_2$ , will not pass into lower RI material if the angle of incidence  $\theta_i$  exceeds the critical angle  $\theta_c$ , where  $\theta_c = \sin^{-1}(n_2/n_1)$ . Such case where all the energy of light is reflected back into  $n_1$  medium is called total internal reflection (TIR). The combination of ellipsometry and TIR methods is called total internal reflection ellipsometry (TIRE).

The TIRE method scheme consists of a prism attached to sample embedded in SE optical scheme. When the angle of incidence from the prism to the other dielectric with lower refractive index is larger than critical angle, then  $\sin \theta_i > 1$  and the transmitted angle becomes complex with imaginary cosine function, thus the reflection coefficients become complex and the phase difference between p- and s-polarization components then can be expressed as:

$$\Delta = \delta_p - \delta_s = 2 \arctan \frac{\sqrt{\sin^2 \theta_i - \sin^2 \theta_c}}{\sin \theta_i \tan \theta_i}. \quad (3.4)$$

When TIR conditions (angles over  $\theta_c$ ) are achieved, the sensitivity of ellipsometric parameter  $\Delta$  is more enhanced than that of an external reflection [124]. Thus, for thin film measurements such configuration in ellipsometry, allows to have enhanced sensitivity for thin film measurements.

### 3.1.3 Types of ellipsometers

The photonic-plasmonic structures presented in section 4 of the thesis were measured using two types of ellipsometers: J. A. Woollam's "M-2000X" (Chapters 4.2, 4.3 and 4.4) and "RC2" (Chapters 4.1, 4.5) models. These ellipsometers were used for SE, TIRE and *in-situ* measurements.

The "M-2000X" is a horizontal variable angle spectroscopic ellipsometer with rotating compensator before the sample. The spectral range is 245 – 1000 nm and the angle of incidence ranges from 45° to 90°. For the excitation of the Tamm plasmons, a conventional configuration of variable angle spectroscopic ellipsometry (VASE) without a prism coupler was used. For the excitation of the SPP and hybrid TPP-SPP modes, a total internal reflection (TIR) configuration of spectroscopic ellipsometry with 45°, 70° and cylinder prism couplers. For the sample in section 4.2 due to small area of graphene, the micro spot focusing optics were used. The longer axis of the

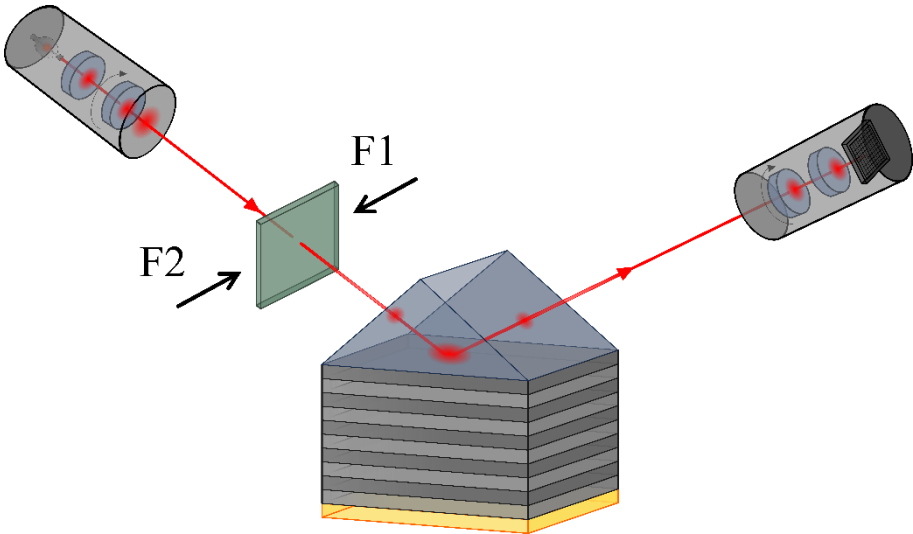


**Figure 3.1.2.** The scheme of TIRE (with RC2 ellipsometer) configuration for strong coupling measurements with filters.

light spot of the ellipse was about 180  $\mu\text{m}$  in the case of VASE measurements and  $\sim 290$   $\mu\text{m}$  in TIRE configuration due to slightly defocused beam. The measured ellipsometric spectra  $\Psi(\lambda)$  and  $\Delta(\lambda)$  were then analyzed and compared to the multi-layer model designed with a CompleteEASE™ software. By using the regression analysis method, the thicknesses and the optical constants of the layers were determined.

The “RC2” is a vertical ellipsometer with two rotating compensators – one before and other after the sample. The spectral range of “RC2” is 210 – 1700 nm and the range for AOI is 20° - 90°. VASE configuration was used and for the excitation of HLPP modes and the hybrid TPP-SPP mode (section 4.1), a total internal reflection (TIR) configuration with a 45° prism coupler was used. The experimental evaluation of the strong coupling was performed by embedding filters in the “RC2” ellipsometer’s optical scheme (Fig. 3.1.2).

## 3.2 Sample production methods

### 3.2.1 Structures supporting Tamm plasmon polaritons states

The production methods for structures, supporting hybrid Tamm plasmon – surface plasmon polaritons and TPP modes, will be presented in this section. The structures consisted of 1D PC with thin metal layer deposited by ion beam sputtering (IBS) and magnetron sputtering.

The PCs were constructed of  $\text{TiO}_2$  and  $\text{SiO}_2$  layers, produced using the ion beam sputtering technique. The IBS (IBS@LAB) chamber was evacuated to  $\sim 7 \times 10^{-6}$  mbar and then filled with argon (Ar) and oxygen ( $\text{O}_2$ ) gas (>99.999 % pure). For the  $\text{TiO}_2$  and  $\text{SiO}_2$ , the deposition rates were 0.09 nm/s and 0.14 nm/s, respectively. The 1D PC used for the samples presented in sections 4.1 and 4.2 consisted of 6 bilayers of  $\text{TiO}_2/\text{SiO}_2$  (60 nm/110 nm) deposited on a BK-7 glass slide substrate with 30 nm  $\text{TiO}_2$  on top and the PC presented in section 4.3 was constructed with thicker  $\text{TiO}_2/\text{SiO}_2$  (120 nm/200 nm) bilayers. For the structure used in section 4.4 10 bilayers of  $\text{TiO}_2/\text{SiO}_2$  (60 nm/110 nm) were deposited on a commercial quartz crystal microbalance (QCM) sensor chip, consisting of 300  $\mu\text{m}$  monocrystalline quartz substrate with 200 nm Au layer.

Further, the top of 1D PCs were covered in 40 nm gold (sections 4.1, 4.3, 4.4) by magnetron sputtering (Kurt J. Lesker PVD 225). The average deposition rate of the gold was 0.22-0.24 nm/s. The PC from section 4.2 was covered by 40 nm silver using glancing angle deposition method [125] and on top of Ag graphene monolayer was deposited. A commercially available single layer graphene (SLG) deposited via chemical vapor deposition (CVD)

growth onto Cu film with a poly(methyl methacrylate) (PMMA) layer on top was used [126]. The Cu film was then chemically dissolved from the Cu/SLG/PMMA structure, leaving the single layer graphene with the PMMA floating on the surface of the solution. The SLG/PMMA was then transferred onto the surface of the sample.

### 3.2.2 Hybrid lattice plasmon polaritons formed by direct laser writing

Large-scale thin gold film (thickness  $\sim 50$  nm and 25 nm) arrays, supporting HLPP modes (presented in section 4.5), were produced using a direct laser writing (DLW) technique with second-harmonic (515 nm) of 300-fs laser pulses generated by Yb:KGW based fs-laser (Pharos, Light Conversion Ltd.). The femtosecond laser beam was tightly focused to  $\sim 1$   $\mu\text{m}$  spot with 0.5 numerical aperture (NA) of the lens. Single-pulse irradiation of a thin gold film leads to the formation of a gold microbump [116,127], which is a key element of the fabricated array (section 4.5). The gold bumps formation in the Au film process is shown in Fig. 3.2.1 left. Each gold bump was fabricated using a single laser pulse with 1.5 nJ energy. The sample translation speed and pulse repetition rate were 2.8 mm/s and 4 kHz, respectively, to keep a 0.7  $\mu\text{m}$  distance between bumps in the scanning direction ( $x$ -axis). The distance between bumps in the  $y$ -axis direction (perpendicular to beam scanning) was kept 0.7  $\mu\text{m}$  by moving the translation stage. The formation of the gold bumps in the film is caused by the thermal stresses generated in a solid film using laser pulse energy below the melting threshold [128]. After irradiation of gold film deforms due to plastic deformation and as a result a bump is formed. Since the laser beam has a

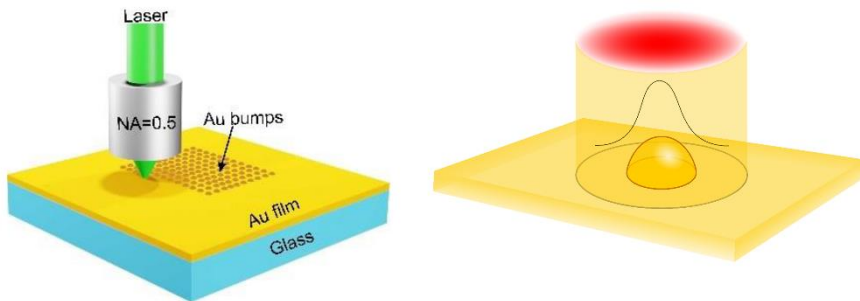


**Figure 3.2.1.** Illustration of Au bumps formation in a thin gold film using direct laser writing technique (left) and the laser beam energy distribution upon gold film surface (right).



Gaussian intensity distribution, the main part of the pulse energy is concentrated in the central part of the laser beam (Fig. 3.2.1 right). Therefore, the size of the fabricated gold bumps is smaller than the focused laser beam spot.

### 3.3 Sample characterization methods

#### 3.3.1 Raman spectroscopy

Raman spectroscopy was used to ensure that the graphene (for sample from section 4.2) was deposited onto the surface of the Ag layer. The Raman spectra were recorded using an inVia Raman (Renishaw, UK) spectrometer equipped with a thermoelectrically cooled ( $-70\text{ }^{\circ}\text{C}$ ) CCD camera and a microscope. The Raman spectra were excited with 532 nm wavelength light from a continuous-wave diode-pumped solid-state laser (Renishaw, UK). A 20x/0.40 NA long working distance objective lens and a grating (1800 lines/mm) were used to record the Raman spectra. The accumulation time was 100 s. To avoid damage to the sample, the laser power at the sample was restricted to 0.06 mW. The Raman scattering wavenumber axis was calibrated by the polystyrene Standard Raman spectrum. The parameters of the bands were determined by

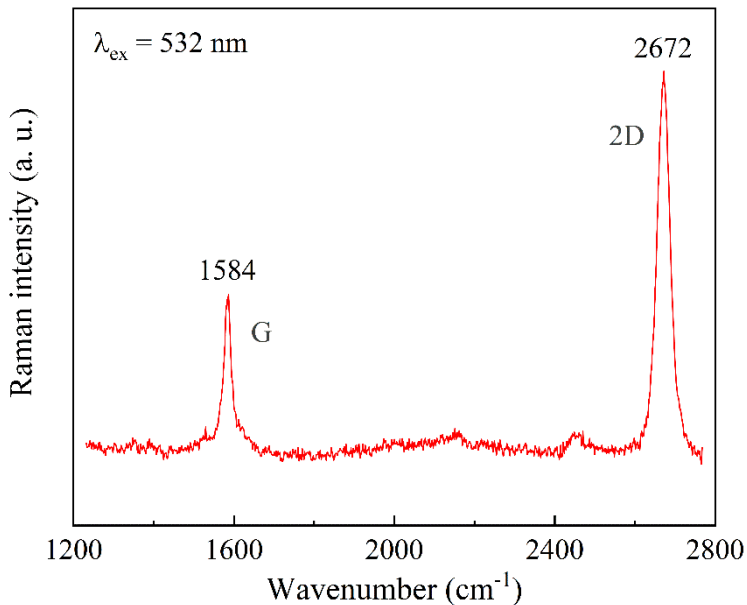


**Figure 3.3.1.** Resonance Raman spectrum of graphene monolayer on the PC/Ag substrate. The excitation wavelength is 532 nm (0.06 mW).

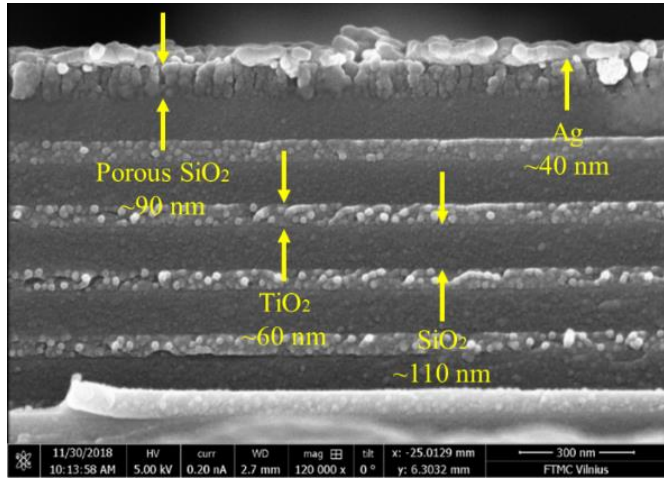


**Figure 3.3.2.** Cross section of the sample. A PC composed of 6 TiO<sub>2</sub> and SiO<sub>2</sub> bilayers of 60 nm and 110 nm respectively, with a 90 nm thick layer of porous SiO<sub>2</sub> and a thin coat (40 nm) of Ag on top.

fitting the experimental spectra with Gaussian-Lorentzian shape components using GRAMS/A1 8.0 (Thermo Scientific) software.

Resonance Raman (RR) spectroscopy is able to provide significant structural information on graphene-based materials [129–132]. The number of graphene layers can be determined from an analysis of the intensity ratio of the 2D and G bands ( $I_{(2D)}/I_{(G)}$ ) [133,134]. The Resonance Raman spectrum of the graphene layer on the 1D PC/Ag sample is shown in Fig. 3.3.1. An enhancement of the  $I_{(2D)}/I_{(G)}$  ratio is expected for single layer graphene; usually this is  $I_{(2D)}/I_{(G)} > 2$ . However, other factors such as a charge-transfer or a stacking order may affect the  $I_{(2D)}/I_{(G)}$  ratio [130,135]. In the case of our studied sample, the  $I_{(2D)}/I_{(G)}$  ratio was found to be 2.4. This was consistent with the previously reported data for single layer graphene [133–135]. The defects in the graphene structure can be probed by an analysis of the D band (“disorder induced” band) near  $1350\text{ cm}^{-1}$  [134]. Such band is not visible in RR spectrum (Fig. 3.3.1), indicating the high structural quality of the graphene film being studied.

### 3.3.2 Scanning electron microscopy

The morphology of the PC/metal structures used in sections 4.1-4.4 and bump arrays on gold films (section 4.5) were evaluated from scanning electron microscopy (SEM) micrographs. The SEM micrographs of the samples BK7/1D PC/Ag and QCM/1D PC/Au cross-sections are presented in

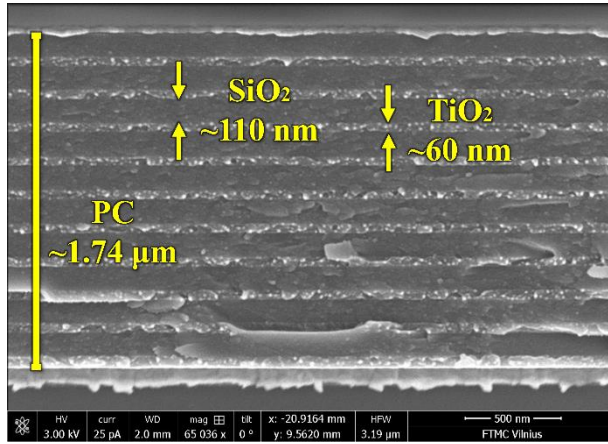


**Figure 3.3.3.** SEM micrograph of the modified QCM sensorchip.

Figures 3.3.2 and 3.3.3, respectively. The thicknesses of TiO<sub>2</sub> and SiO<sub>2</sub> layers determined from SEM micrographs by analysis software ImageJ were approximately 60 nm and 110 nm thick, respectively. In Fig. 3.3.2 an additional 90 nm layer of porous SiO<sub>2</sub> on top of 110 nm SiO<sub>2</sub> can be seen. The PC structures consisted of 6 and 10 bilayers of TiO<sub>2</sub>/SiO<sub>2</sub> for Fig. 3.3.2 and Fig. 3.3.3 samples, respectively.

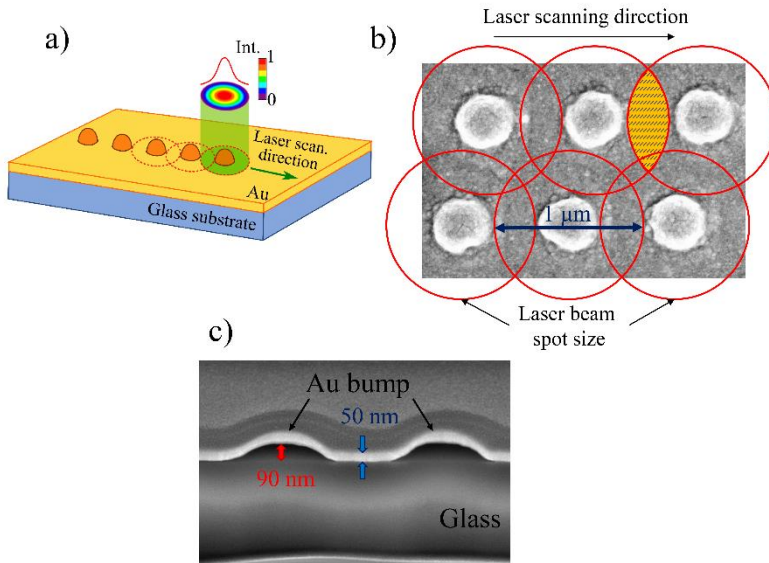


**Figure 3.3.4.** a) Illustration of the formation process of Au bump; b) the irradiated gold film areas with a laser beam (red circles) in the gold bumps fabrication process; c) SEM micrograph of gold bumps cross-section.

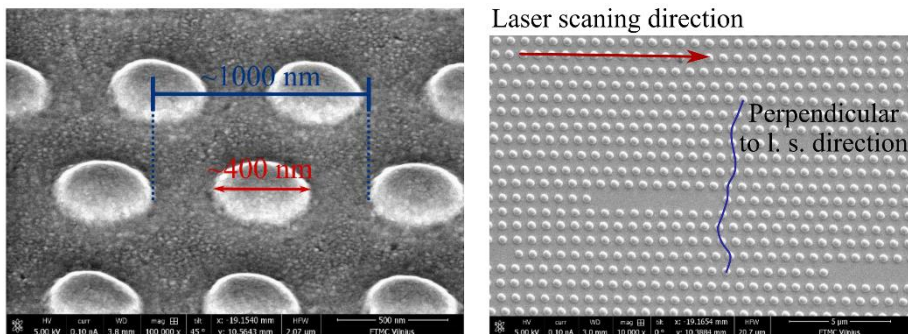


**Figure 3.3.5.** SEM micrographs of the formed bump arrays. The bump is  $\sim 400$  nm diameter (left) and orderly in the laser scanning direction (right).

The laser pulse, used for bump array formation, overlapped at each step (Fig. 3.3.4 a and b). The SEM micrographs of the top gold bump array shows the orderly distribution of the bumps and from the cross-section (Fig. 3.3.4 c) a hollow bump structure can be seen. The height of micro bumps is  $\sim 90$  nm and the size of the bumps depends on the gold film thickness and laser processing parameters.

The diameter of micro bumps in 50 nm gold film was approx. 400 nm and the period is  $\sim 700$  nm (Figure 3.3.5). The diameters of gold bumps were evaluated using the analysis of SEM micrographs with image processing and analysis software (ImageJ) [136]. The bumps are periodic in laser scanning direction, while in the perpendicular direction is not as orderly as the parallel (Fig. 3.3.5 right).

### 3.4 Protein adsorption on sensor surfaces

The protein adsorption to a gold surface process is performed through several stages. For the granulocyte colony-stimulating factor receptor (GCSF-R) immobilization, performed on 4.3 section samples, a self-assembling monolayer – SAM (11-Mercaptoundecanoic acid (11-MUA) (98%)) was formed. The carboxyl groups of formed SAM were then activated by using a 50/50 solution of N-hydroxysuccinimide (NHS) and N-(3-dimethylaminopropyl)-N'-ethylcarbodiimide hydrochloride (EDC). Further the protein G was attached to the surface for covalent immobilization of receptor. The recombinant extracellular domain of the human GCSF-R protein, which was fused with a human Fc region of IgG1 (GCSF-R) was kindly supplied by Profarma (Vilnius, Lithuania).

A commercially available SPR chip (XanTec bioanalytics GmbH), consisting of BK-7 substrate with 2 nm Cr adhesion layer and a 50 nm gold

layer that was used for the conventional SPR-based measurements. The PC/Au structure grown on a BK-7 substrate was used for the generation of hybrid TPP-SPP mode. Both samples were first cleaned using a plasma cleaner, then the sensors were immersed in a 1mM 11-mercaptoundecanoic acid (11-MUA) solution in methanol for 18 h. A self-assembled monolayer (SAM) was formed over the surfaces of both samples. Then the sensing chips of the BK-7 glass/Cr-Au and the BK-7 glass/PC/Au with the formed SAM, consisting of the 11-MUA, were rinsed with pure methanol (99,9 %) and dried using pressurized nitrogen gas. Both samples with the 11-MUA modified SAM were then attached to a semi-cylindrical BK-7 glass prism and mounted on a TIRE cell for ellipsometric measurement in liquids.

The TIRE cell was filled with high purity deionized water and a baseline was established for 40 min. In order to covalently immobilize the GCSF-Receptors, a solution of 0.1 M (NHS) and 0.4 M (EDC) was used to activate the carboxyl groups on the 11-MUA SAM. For this purpose, a prepared solution of 0.1 M NHS and 0.4 M EDC was injected into the TIRE cell and incubated for 20 min. The TIRE cell was then washed with deionized water, which was then replaced with a 10 mM sodium acetate buffer (pH=4) until the baseline signal settled and did not change. Then, when a steady-state TIRE signal was reached, a solution containing 100 µg/mL of Protein-G in a 10 mM sodium acetate buffer was injected and incubated until signal saturated over time. After 79 min of incubation, the cell was rinsed with pH=4 for 10 min, then changed to a 1M ethanolamine hydrochloride, pH=8.5, solution for the blocking of the remaining unbound activated carboxyl groups over the next 15 min. After this, the nonspecifically bounded Protein-G was removed by washing it with a 10 mM solution of glycine, pH=3.0, for 10 min. The glycine solution was then changed to the phosphate buffer solution (PBS), pH=7.4, until steady state conditions were again reached after 15 min.

The next step of the experiment was the immobilization of the GCSF-Receptor (GCSF-R) [137]. The PBS solution, pH=7.4, containing  $5.32 \cdot 10^{-8}$ M of GCSF-R, 140 mM of NaCl, 2.7 mM of KCl, 10 mM of  $K_3PO_4$  was injected into the TIRE cell for 62 min. After washing the unbounded analyte with the PBS, the oriented GCSF-R layer was formed.

The covalent immobilization of the Bovine serum albumin (BSA) measurements were performed for the optimized hybrid TPP-SPP mode (section 4.3) and the TPP mode excitation (section 4.4). The cleaning protocol was the same as mentioned above for both samples. The substrate was modified by activation of the carboxyl groups onto the 11-MUA SAM using EDC/NHS. The TIRE cell was washed with PBS solution (pH=7.4), and then 100 µg/ml BSA in PBS was injected. For the biosensing experiments with

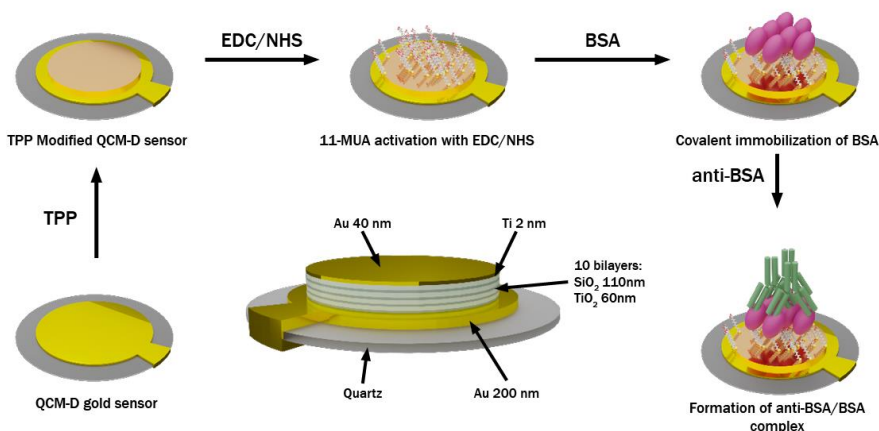


**Figure 3.4.1.** A scheme representing formation of BSA and anti-BSA proteins on a modified QCM-D sensorchip.

Tamm plasmon modes (section 4.4), the samples were cleaned in an ultrasound bath for 3 min, then washed with hexane and methanol and immersed in a solution of 1 mM 11-MUA in methanol for the formation of self-assembled monolayer (SAM) for 18 h. SAM modified sensor discs were placed in QSense ellipsometry (combined quartz crystal microbalance and spectroscopic ellipsometry) module. QSense chamber was filled with deionized water and the baseline was established. Then EDC/NHS solutions mixed by equal parts were injected into the chamber for 15 min to activate the carboxylic groups. During the next step, the chamber was washed with deionized water and filled with PBS pH 7.4. For covalent BSA immobilization on the 11-MUA SAM, the solution of BSA 1 mg/mL was injected into the chamber. When steady state conditions were established, the chamber was rinsed with PBS. Finally, 0.5 mg/mL solution of anti-BSA in PBS pH 7.4 was injected. When the monolayer of antibodies was formed (Figure 3.4.1) and steady state conditions were reached, the chamber was washed with PBS. During all modification steps for both samples QCM-D and mQCM-D, SE and QCM-D measurements of the kinetics were monitored simultaneously in real time.

## 4 RESULTS

### 4.1 The experimental evidence of strong coupling between tamm and surface plasmon polaritons modes

#### 4.1.1 Introduction

The existence of hybrid modes has been shown to exist between two different plasmonic excitations – surface plasmon polaritons (SPP) and Tamm plasmon polaritons (TPP) [18]. If the conditions for the excitations are satisfied for both resonances of the SPPs and TPPs, hybrid modes of both non-overlapped excitations can be generated. In such systems, the TPP and SPP resonances exist in a broad range of angles of light incident (AOI) to the prism. At certain AOIs to the prism corresponding to the same wavevectors at which both the SPPs and TPPs can be excited, the reflectance spectrum is changed, and the dispersion relations of both excitations are modified. These changes in the reflectance and dispersion relations indicate in most cases a strong coupling regime between the TPPs and SPPs. It should be noted that these alterations of the plasmonic resonances in the wavelength spectra also indicate their dynamics in the time domain at frequencies that correspond to their splitting into the hybrid mode [14]. This leads to an exchange of energy between SPPs and TPP during the time of the coherence. Pump-probe spectroscopy is usually used to investigate the dynamics of strongly coupled oscillators [2]. However, the decay times for the plasmon modes are about  $\sim 100$  fs, which indicate that the coherent energy exchanges are even shorter in time. Thus, the observation of these processes becomes rather challenging [138,139], while the measurement of the reflection-transmission spectra in the wavelengths (frequency domain) remains much simpler. On the other hand, the analysis of the experimental reflectance spectra can be rather complicated and ambiguous as the strong coupling can be confused with other effects such as Fano-like interference (or exciton-induced transparency) [140].

In this study, unambiguous experimental evidence of strong coupling between the TPP and SPP resonances in the hybrid TPP-SPP mode by tuning of the reflectance spectra with the optical filters, using the total internal reflection ellipsometry (TIRE) method [124,141] is presented. Simple optical methodology using optical filters to cut the part of incident light spectra was proposed. Using optical filters measured energy spectra was divided into two parts where in each range only one branch of the hybrid TPP-SPP plasmonic mode was excited directly by the incident light. Present experimental studies have shown that if the investigated system is in strong coupling, this is always

enough to excite only one component of the hybrid excitation. Thus, its dispersion relation will be the same as when the excitation is done with a whole spectrum.

The results presented in the following Chapter were originally published in: E. Bužavaitė-Vertelienė, V. Vertelis and Z. Balevičius. “The experimental evidence of a strong coupling regime in the hybrid Tamm plasmon-surface plasmon polariton mode” *Nanophotonics* **10**(5), 2021, pp. 1565-1571. <https://doi.org/10.1515/nanoph-2020-0660>.

#### 4.1.2 Experimental demonstration of strong coupling regime

Three different TIRE spectra were measured (Fig. 4.1.1). First, the full spectra (Fig. 4.1.1, grey curve) of hybrid TPP-SPP mode was measured. Both, the TPP and SPP components manifested themselves at the 533 nm and 641 nm wavelengths, respectively. Different optical filters were used to excite only one resonance (either the TPP or SPP). Due to this, some parts of source light

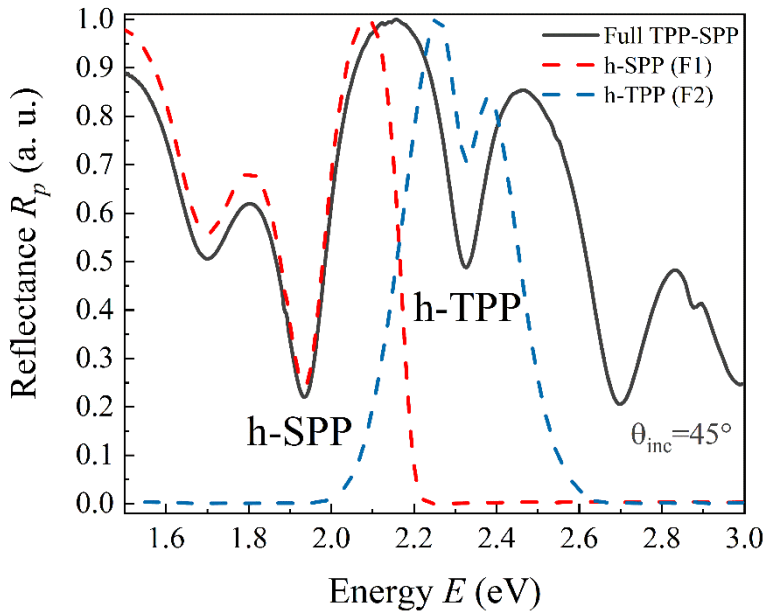


**Figure 4.1.1.** The experimental p-polarisation reflectance spectra (at  $45^\circ$  AOI) of a hybrid TPP-SPP mode (grey curve) and the spectra measured with filters F1 (red curve) and F2 (blue curve) which cut out the h-SPP and h-TPP parts, respectively.



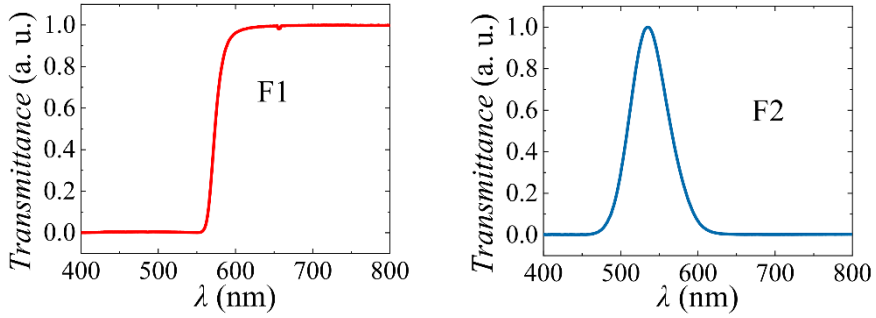


**Figure 4.1.2.** The transmittance spectra of the filters F1 (red line) and F2 (blue line).

were cut. An optical filter Schott VG 14 (F2), whose transmission spectrum is presented in Fig. 4.1.2 right, was used to cut a part of the white light source in order to leave only the TPP resonance (Fig. 4.1.1, blue dashed curve). Afterwards, the SPP component (Fig. 4.1.1, red dashed curve) in the hybrid mode was left and the TPP was cut with filter Schott OG 590 (F1). All three types of the spectra were measured in light angles of incidence in the range of  $40.5^\circ$ - $49.5^\circ$  and the experimental dispersion relations were determined. The measured spectra (Fig. 4.1.1) were normalized to the bandpass filter (Fig. 4.1.3). From figure A it can be clearly seen that filter F1 totally cuts the part of the spectra below 550 nm in which TPP component was generated, meanwhile for the figure B the filter F2 cuts out the spectra with SPP component, yet not well enough, as noisy signal partially replaced the line shape of SPP component. This fact is also related with sensitivity of TIRE method where the ratio of reflected field amplitudes p- and s-polarization actually measured and reflection intensity are calculated from ellipsometric parameters. Thus, the miniscule intensity reflection due to the filter F2 imperfection is detected by spectroscopic ellipsometer. As the main goal of this study was to experimentally prove the concept of the strong coupling, therefore, in the manuscript we present the intensity spectra of p-polarized reflection normalized to 1.

The strong coupling regime has been found and widely studied in the various exciton and surface plasmon supporting systems [2,6,16]. Nanostructures supporting Tamm plasmons have also begun to be widely used to couple these surface states with excitons [82,142,143]. It has been found [18] that both the TPP and SPP surface modes can be excited simultaneously on the same metal layer and interact with each other when suitable conditions

are satisfied. In such cases, a new hybrid TPP-SPP mode appears and the anti-crossing of the TPP and SPP resonances has been revealed [18,20].

When the energy exchange between the two harmonic oscillators exceeds the damping rate, the system is in a strong coupling regime. Under such conditions, the original resonant frequencies of the single oscillators are modified and a new hybrid mode appears in which the coupled oscillators are inextricably linked with each other [140]. In this study, the simultaneously excited TPP and SPP components corresponded to the two coupled oscillators. The definition of the strong coupling regime [14] implies that if the external excitation source has a frequency range suitable to excite only one component (the TPP or SPP), still both parts of the hybrid mode should be generated, because one component excited by an external source will coherently transfer energy to the second component of the coupled oscillators. As a result, the behavior of the directly excited plasmonic components should follow the dispersion relation of the hybrid mode instead of the uncoupled ones.

To confirm this statement, the experimentally measured energy spectra (Fig. 4.1.1) was divided into two parts where in each range only one branch of the hybrid TPP-SPP plasmonic mode was excited directly by the incident light. The variable angle TIRE measurements were conducted to evaluate and compare the dispersion relations of the separate components with the general spectra. The general spectra are presented as a reflectance map of the TM-polarization and the separate components marked as the dots on the map in Fig. 4.1.4 (a). Also, the other modes have contribution to the whole optical response. The dispersion curves lower than 1.75 eV corresponds to the edge of the photonic stop band and interference of the Bragg mirror. As can be clearly seen, both components (TPP and SPP), excited separately, are generated exactly at the same energies as in the general spectra when both components

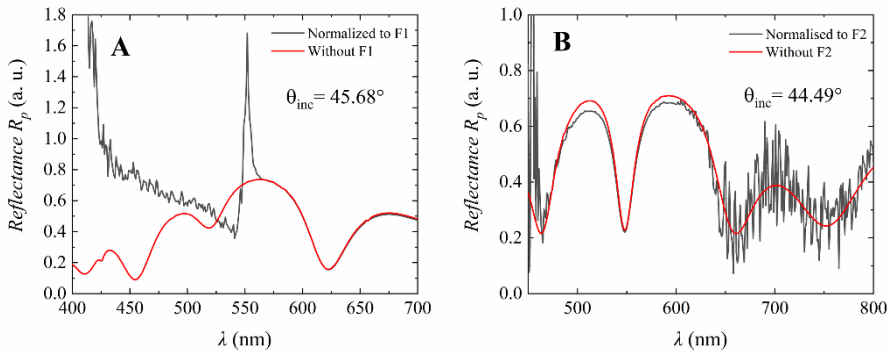


**Figure 4.1.3.** The reflectance spectra of hybrid TPP-SPP modes normalized to the transmission of bandpass filters F1 (A) and F2 (B).

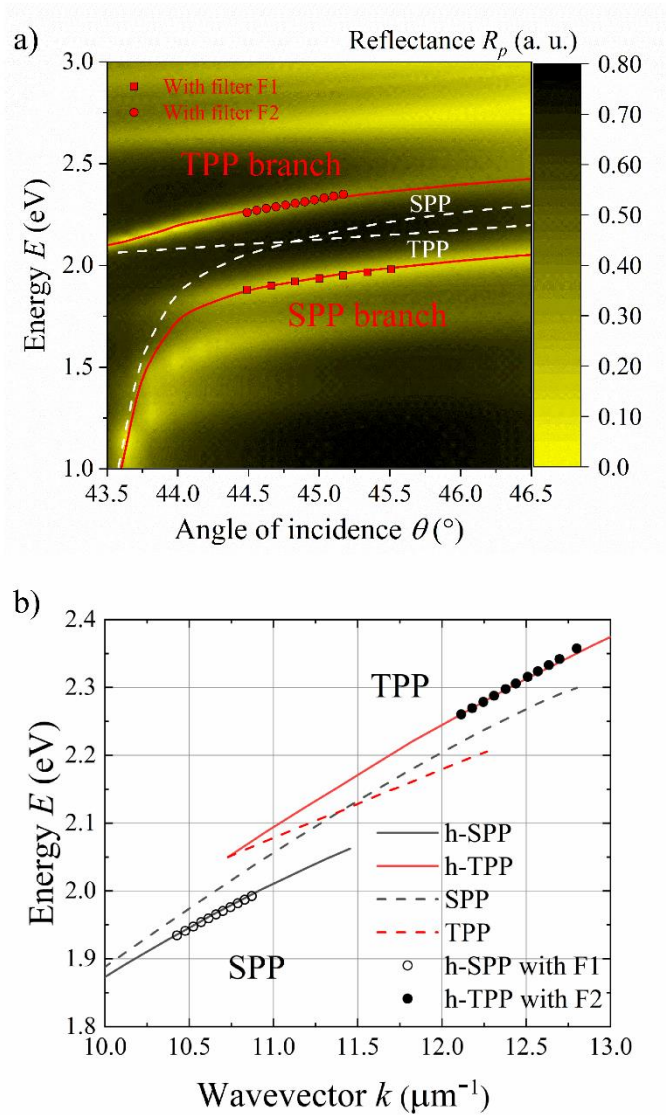


**Figure 4.1.4.** a) The experimental dispersion relation of the hybrid TPP-SPP mode (red lines) with the calculated non-coupled single TPP and SPP modes (white lines) and the experimental results of the hybrid mode with filters incorporated into an optical scheme (squares TPP branch and circles SPP branch). b) The dispersion relation of the hybrid TPP-SPP mode (solid lines), the h-TPP, h-SPP with filters F1, F2 (circles) and the dispersion of the uncoupled single plasmonic TPP and SPP modes (dashed lines).

were excited simultaneously. The modelled uncoupled TPP and SPP dispersion curves are presented as the white crossed curves in Fig. 4.1.4 (a), while the separately excited TPP and SPP branches (dots) follow the dispersion relation of coupled general spectra (map). Such behavior can be realized only in the case when the separate excitations of the hybrid plasmonic modes are influenced by the presence of the other components. This, however, implies that the system should be in the strong coupling regime, as otherwise, the separate plasmonic components should follow the dispersion relations of their uncoupled excitations.

The strong coupling between the TPP and SPP leads to the alteration of their initial frequencies. Thus, due to the anti-crossing effect, the two plasmonic branches form the gap in the frequency spectra called the vacuum Rabi splitting [14]. The value of the Rabi splitting allows one to determine whether the system is in a strong coupling regime or not. In the field of plasmonics and photonics, this strong coupling regime is usually defined as the range of splitting which exceeds the linewidths of the two coupled systems. It has been reported that in order to more precisely evaluate the coupling strengths between the two coupled oscillators, it is necessary to analyze a plot of the wave vector vs. energy, instead of the angle of incidence vs. energy, which is directly obtained from the reflectance measurements [6]. The exact Rabi splitting for the hybrid TPP and SPP modes can be seen in the Fig. 4.1.4 (b) and was about 105 meV. It should be noted that for the hybrid TPP-SPP plasmonic modes, the differences in the gap when the angle of incidence is monitored instead of the wave vector can be overestimated by more than 3 times.

As has been shown before [38], the interference effect usually makes a noticeable contribution to the optical response and can distort the peaks of the coupled excitations. In order to evaluate the coupling strength and to distinguish the strong coupling from the weak and the other interference effects such as Fano resonances [38], a fitting procedure of the whole spectra needs to be conducted. The coupled plasmonic excitations were modelled as two Lorentz oscillators which influence each other with equal strength [144]:

$$\begin{cases} \ddot{x}_{TPP} + \gamma_{TPP}\dot{x}_{TPP} + \omega_{TPP}^2 x_{TPP} = F + g x_{SPP} \\ \ddot{x}_{SPP} + \gamma_{SPP}\dot{x}_{SPP} + \omega_{SPP}^2 x_{SPP} = F + g x_{TPP} \end{cases} \quad (4.1)$$

Where  $g$  is the coupling strength,  $\omega_j$  the resonance frequencies, and  $\gamma_j$  the damping terms that correspond to the linewidths of the TPPs and SPPs, respectively.  $F = F_0 e^{i\omega t}$  was the external driving force. We looked for solutions

in the form of  $x_j = X_j e^{i\omega t}$ . Thus, the resulting complex amplitudes for the oscillators were:

$$X_{TPP} = F_0 \frac{W_{SPP} + g}{W_{TPP}W_{SPP} - g^2}. \quad (4.2)$$

$$X_{SPP} = F_0 \frac{W_{TPP} + g}{W_{TPP}W_{SPP} - g^2}. \quad (4.3)$$

Where:

$$W_j = -\omega^2 + j\gamma_j\omega + \omega_j^2. \quad (4.4)$$

Assuming there was no detuning and no damping, the resulting hybridized frequency for the oscillators is given by:

$$\omega_{\pm} = \frac{\sqrt{\omega_{TPP}^2 + \omega_{SPP}^2 \pm \sqrt{4g^2 + (\omega_{TPP}^2 - \omega_{SPP}^2)^2}}}{\sqrt{2}}. \quad (4.5)$$

We treated  $\omega_j = \omega_j(\theta)$  as a function of the angle of incidence. Furthermore, to determine whether the investigated multilayer structure was in a strong coupling regime or not, the coupling strengths between two coupled plasmonic oscillators were analyzed by regression analysis (fitting).

#### 4.1.3 Fitting of the experimental results

The value of the strength of the coupling parameter  $g$ , however, does not give a direct answer as to whether the system is in strong coupling regime or not since the system is in the strong coupling regime only when parameter  $g$  is larger than [38]:

$$g > \frac{1}{4}(\gamma_{TPP} + \gamma_{SPP}). \quad (4.5)$$

Thus, for a more precise evaluation of the strong coupling parameters, only the TM-polarized reflectance spectrum was used for the regression analysis instead of the total reflection intensity spectra, where both the TE- and TM-polarizations had contributions to the optical response. This was done because

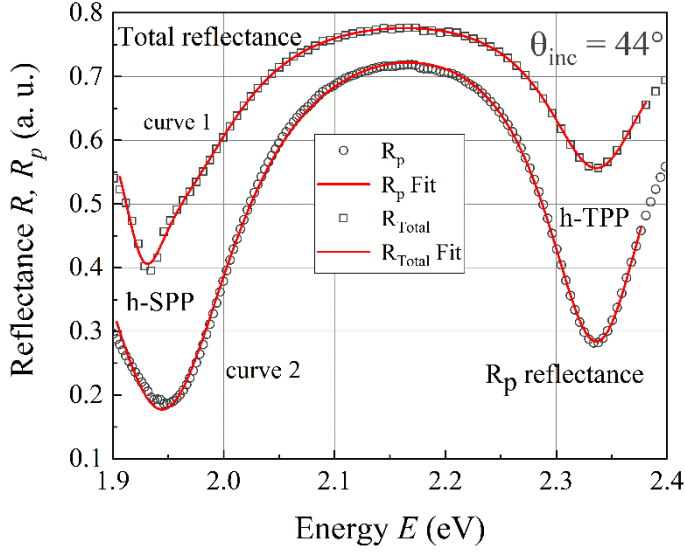


**Figure 4.1.5.** The hybrid TPP-SPP mode experimental (curve 2) TM-polarization reflection spectra and the total reflectance (curve 1) for the angle of incidence  $\theta=44^\circ$ . The red curves are the fitting results.

the coupling between the Tamm plasmon polariton and the surface plasmon polariton can only be realized for TM-polarized light. In the intensity reflection spectra, the TE-polarization, which is not involved in the coupling with the surface plasmon, distorts and partially masks the two coupled plasmonic oscillators related to the hybrid TPP-SPP mode. This can be clearly seen from the spectra in Fig. 4.1.5, where the sharp dip at the 1.88 eV in the curve with total reflectance is related to the Tamm plasmon for TE-polarization. The fitting results (Fig. 4.1.6) of the TM-polarized reflection  $R_p$  at different AOI show that the strength parameter  $g$  had larger values than right side of the inequality (2), indicating the strong coupling regime (Table 1). The residual square or coefficient of determination (COD) of the fitting varied from 0.97622 to 0.99782.

It should be noted that applied rather simple coupled oscillator model do not take into account the multiple coupling with other modes such as edge of the photonic stop band of the Bragg mirror. This fact has influence to the evaluation of strong coupling parameter  $g$  and fitting errors (Fig. 4.1.6 (inset), Table 1) which increases at the angles of incidence ( $43.98^\circ$ ,  $44.32^\circ$  and  $45.68^\circ$ ,  $46.02^\circ$ ) further from the anti-crossing point (Fig. 4.1.4 a, white dashed lines). However, the fitting procedure was sensitive enough to evaluate whether the system is in a strong coupling regime or not between TPP and SPP branches.

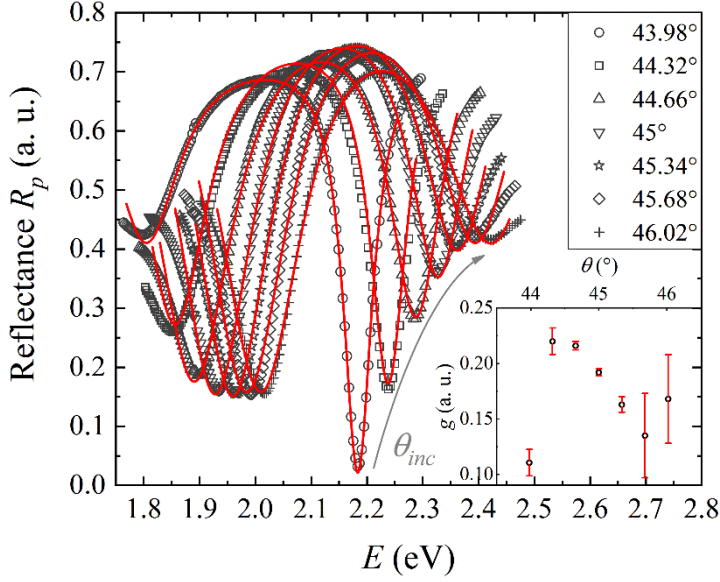


**Figure 4.1.6.** The hybrid TPP-SPP mode experimental (shapes) TM-polarization reflection spectra and those calculated by using the expression 4 (solid red line) curves. The inset on the bottom right shows the values of the coupling parameter  $g$  and its error bars.

**Table 1.** Fitting parameters of the p-polarized reflection spectra at different angles of incidence ( $\theta_i$ ). Parameters  $\omega_{SPP}$  and  $\omega_{TPP}$  are the resonance frequencies (eV),  $\gamma_{SPP}$ ,  $\gamma_{TPP}$  (eV) are the damping terms (FWHM) of the hybrid mode excitations h-SPP and h-TPP, respectively, and the parameter  $g$  indicates the coupling strength. The \* marks  $\pm 10^{-3}$  error limit.

$\theta_i^\circ$	$\omega_{SPP}^*$	$\omega_{TPP}^*$	$\gamma_{SPP}^*$	$\gamma_{TPP}^*$	$g$ (eV)
43.98	1.809	2.184	0.185	0.067	0.11 ( $\pm 1.2 \cdot 10^{-2}$ )
44.32	1.863	2.238	0.184	0.092	0.22 ( $\pm 1.2 \cdot 10^{-2}$ )
44.66	1.903	2.282	0.174	0.123	0.216 ( $\pm 3.8 \cdot 10^{-3}$ )
45	1.94	2.325	0.18	0.161	0.192 ( $\pm 3 \cdot 10^{-3}$ )
45.34	1.968	2.361	0.177	0.183	0.163 ( $\pm 7 \cdot 10^{-3}$ )
45.68	1.992	2.395	0.175	0.201	0.135 ( $\pm 3.8 \cdot 10^{-2}$ )
46.02	2.014	2.426	0.195	0.216	0.168 ( $\pm 4 \cdot 10^{-2}$ )

## Summary

Summarizing, we propose a simple optical methodology using optical filters which gives unambiguous experimental evidence of the strong coupling regime in the hybrid TPP-SPP mode. Present experimental studies have shown that if the investigated system is in strong coupling, this is always enough to excite only one component of the hybrid excitation. Thus, only a part of the incoming light and its dispersion relation will be the same as when the excitation is done with a whole spectrum. In the case of the TPP-SPP hybrid mode where strong coupling is realized only in TM-polarized light, the fitting results have shown that the strongest coupling will be at the point where the non-interacting TPP and SPP curves should be crossing. As the plasmonic widely applied for realizing the strong coupling and many of these excitations are polarization dependent, the evaluation of the coupling strengths can be better conducted in a spectrum where only the state of the light polarization responsible for the strong coupling is involved. Polarization based optical methods such as spectroscopic ellipsometry thus can serve as advanced optical methods having the ability to analyze in detail the strong coupling effect. Application of strong coupling of hybrid TPP-SPP excitations could be valuable due to the reduction of energy losses in the metals and tunability in the desired spectral range. If one component is excited at resonant wavelength, the other is also present and can be controlled by strong coupling between TPP and SPP. The energy conversion between TPP and SPP shows potential applications of hybrid TPP-SPP modes for integrated photonic devices.



## 4.2 Graphene influence on strong coupling between tamm and surface plasmon polaritons

### 4.2.1 Introduction

Graphene physics and plasmonics have become the subjects of wide spread studies and have led to numerous fundamental investigations and applications to novel optical devices [118,145,146]. Moreover, these fields strongly overlap, not only due to the intrinsic plasmons in graphene, which can be tunable in broadband range of wavelengths, but also due to the hybrid nanostructures of graphene and noble metals [147,148], where enhanced light-matter interactions can be expected [149]. Graphene is a 2D crystal consisting of carbon atoms arranged in a honeycomb lattice [150]. Such a crystal structure has very high quantum efficiency for light-matter interaction [118]. The unique optical properties and strong light-matter interactions which arise from the quasiparticles in graphene satisfies a linear dispersion relation [145]. However, the optical absorption of the graphene atomic monolayer is 2.3%, which is a rather large amount for a single layer, but is usually not enough to achieve an effective light-matter interaction for optical modulation, optical sensing and other purposes [151]. The combination of graphene with the traditional plasmonics on noble metals produce opportunities for the enhanced optical features of graphene, for example in Raman spectroscopy [152]. On the other hand, graphene could also be used to influence the optical responses of such hybrid graphene-plasmonic nanostructures [118,153]. These graphene-metal hybrid structures provide a number of advanced applications for conventional plasmonics [154,155].

The optical response of graphene layer in PC/metal structures which supports hybrid plasmonic modes in strong coupling has been studied by numerical simulations [156,157]. A rather small number of works have been dedicated to experimental studies on the influence of graphene layers on coupled plasmonic excitations [118]. In this sense, the behavior of the dispersion relations of the hybrid Tamm-plasmon polariton modes in a strong coupling regime under the influence of graphene have not been investigated before, although such newly acquired knowledge could be a substantial contribution to the development of advanced optical elements and nanodevices with reduced Ohmic losses due to such hybrid modes. In these studies, spectroscopic ellipsometry, TIRE and Raman spectroscopy were used for the characterization of the hybrid TPP-SPP mode generated in a hybrid 1D photonic crystal structure with a thin layer of silver and graphene/PMMA. The motivation of this work was to evaluate the variation of coupling strength due

to the graphene and PMMA layers. The interest in the study of systems which are able to support the strong coupling effect arises from their promising applications to optical information processing, lasing, also to fundamental studies of light-matter interaction and even for employing such structures in biosensors. The Raman spectroscopy showed a consistent monolayer graphene present on the Ag layer. As the TIRE measurements showed a decrease of the TPP and SPP dip components in the hybrid TPP-SPP mode can be explained by the changes of the conductivity of the silver layer due to the presence of graphene/PMMA structure on top of Ag. The design of these hybrid plasmonic/graphene-based nanostructures have attractive capabilities for the development of advanced optical sensors and integrated optical circuit technologies.

The results presented in the following Chapter were originally published in: E. Buzavaite-Verteliene, A. Valavicius, L. Grineviciute, T. Tolenis, R. Lukose, G. Niaura and Z. Balevicius. "Influence of the graphene layer in the hybrid Tamm-plasmon polariton mode" *Optics Express* **28**(7), 2020, pp. 10308-10318. <https://doi.org/10.1364/OE.384079>.

#### 4.2.2 Study of graphene influence on strong coupling

During this study, two different measurement configurations, the conventional variable angle spectroscopic ellipsometry and the TIRE, were used for the excitation of the single TPP and hybrid TPP-SPP modes, respectively. VASE measurements were first conducted in order to examine the optical response of the PC/SiO<sub>2</sub>/Ag structure with the single layer graphene (SLG) and PMMA on top of the Ag. In it, the single TPP excitations manifested themselves as a dip in the ellipsometric spectra of  $\Psi(\lambda)$ . The dependence of the ellipsometric spectra  $\Psi(\lambda)$  and  $\Delta(\lambda)$  on the angle of incidence ( $\theta_{\text{inc}}$ ) can be seen in Fig. 4.2.1 a. The PC/SiO<sub>2</sub>/Ag sample's incident angle measurement range was 45° – 75° degrees. Accordingly, the dips of the TPP optical states (Fig. 4.2.1 a) corresponded to 555 nm, 536 nm, 519 nm, 505 nm for the 45°, 55°, 65° and 75° angles, respectively. The ellipsometric spectra of the sample, before and after the SLG and PMMA deposition, were compared at a 65° angle of incidence (Fig. 4.2.1 b), where the contribution to the optical response of the SLG/PMMA layers were the greatest. The TPP resonance dips can be seen at 519 nm for the PC/SiO<sub>2</sub>/Ag, 520 nm for the PC/SiO<sub>2</sub>/Ag/PMMA and 522 nm for the PC/SiO<sub>2</sub>/Ag/SLG/PMMA, respectively. A red shift of ~1 nm in the ellipsometric spectra  $\Psi(\lambda)$  was observed after deposition of PMMA onto the PC/SiO<sub>2</sub>/Ag sample and a ~3 nm

shift to longer wavelengths in the PC/SiO<sub>2</sub>/Ag/PMMA and the PC/SiO<sub>2</sub>/Ag/SLG/PMMA samples.

For the measurement of the VASE ellipsometric spectra of the PC/SiO<sub>2</sub>/Ag structure with typical TPP curves, the optical model consisted of a BK-7 glass substrate, a PC constructed of 6 bilayers of TiO<sub>2</sub>/SiO<sub>2</sub> of 60 nm/110 nm thicknesses and a 90 nm porous SiO<sub>2</sub> layer on its top with a 40 nm Ag layer

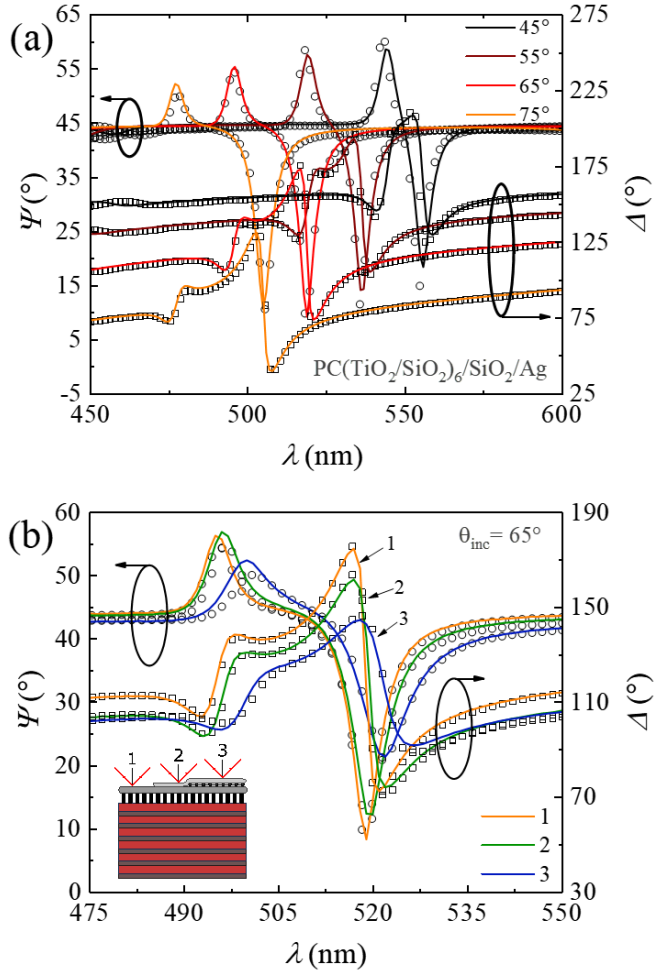


**Figure 4.2.1.** Modeled (solid lines) and experimental (circles and squares) results of (a) a single Tamm plasmon-polariton  $\Psi$  and  $\Delta$  spectra for the PC/SiO<sub>2</sub>/Ag structure at different angles ( $\theta_{inc} \in [45^\circ - 75^\circ]$ ), (b)  $\Psi$  and  $\Delta$  parameters of the samples PC/SiO<sub>2</sub>/Ag (1 - orange), PC/SiO<sub>2</sub>/Ag/PMMA (2 - green) and PC/SiO<sub>2</sub>/Ag/SLG/PMMA (3 - blue) at an angle of incidence of  $65^\circ$ .

over it. The porous SiO<sub>2</sub> layer was defined by effective media approximation (EMA) with a percentage composition of 70% SiO<sub>2</sub> and 30% void. A regression analysis of the PC/SiO<sub>2</sub>/Ag structure was then conducted where the thicknesses of the layers were the fitting parameters. Secondly, the TPP optical state supporting structures with the PMMA and the SLG/PMMA on the top of the silver surface were fitted. The model parameters of the PC obtained before were then fixed, while the thicknesses of the porous SiO<sub>2</sub>, Ag, PMMA and SLG were varied. From the fitting procedure of the PC/SiO<sub>2</sub>/Ag/PMMA structure, the obtained thickness of the PMMA layer was ~10 nm. From the regression analysis of ellipsometric spectra where the SLG was between the Ag and PMMA layers, the obtained SLG thickness was about ~0.8 nm (1 – 2 graphene layers), while the PMMA thickness stayed the same (~10 nm). The optical constants of the Ag and the graphene layers were taken from the literature [158,159] and others (SiO<sub>2</sub>, TiO<sub>2</sub>, PMMA) were obtained from the CompleteEASE™ program software package.

Regression analysis in its conventional VASE configuration for the TPP excitation showed that the values for the substrate structure supporting the TPP excitation, namely the PC/ SiO<sub>2</sub>/Ag layer, were very close (Table 2) to those obtained from the SEM cross-section (Fig. 3.3.2), which were used as the starting values in fitting procedure for the thicknesses of the SiO<sub>2</sub>, TiO<sub>2</sub> and Ag layers. The evaluated ratio of the graphene peaks (2.4) in the Raman spectra, which were measured at five different spots, supports the assumption that the most probable dominating structure on the silver surface was the single layer of graphene (0.34 nm as stated in the literature [160,161]) and this was taken as the starting value in the fitting procedure. The regression analysis showed that the thickness of the graphene layer was about 0.8 nm. Since the light spot diameter was ~250-300 μm, the optical response gave the average value of the graphene layer, which might have some wrinkles or non-homogeneities due to the influence of the PMMA layer on its top. It is thus possible that the average thickness may be thicker. The simulated data were fitted to the experimental VASE results in the range of AOI 45°–75° simultaneously with mean square error (MSE) values of about 20 for the TPP excitation. Also accounted for were the ~1.33±0.06 nm thick mix of Ag and porous SiO<sub>2</sub>. The thicknesses of the PC layers obtained from the PC/SiO<sub>2</sub>/Ag model corresponded to 57±0.1 nm and 110.6±0.2 nm for the TiO<sub>2</sub> and SiO<sub>2</sub>, respectively.

**Table 2.** Thicknesses of the investigated sample layers and the porosity of the SiO<sub>2</sub> determined from regression analysis. EMA expresses the percentage of air in the SiO<sub>2</sub> layer. Numbers 1, 2 and 3 are for structures PC/Ag, PC/Ag/PMMA and PC/Ag/SLG/PMMA, respectively.

	$d_{\text{porous}}$ (nm)	EMA (%)	$d_{\text{Ag}}$ (nm)	$d_{\text{PMMA}}$ (nm)	$d_{\text{SLG}}$ (nm)
1	93±0.1	33.2±0.06	41.4±0.1	-	-
2	92.6±0.1	33.6±0.06	39.8±0.1	9±0.05	-
3	93±0.1	30.5±0.6	42.3±0.1	9±0.05	0.79±0.02

The TIRE configuration was used in order to achieve the hybrid TPP-SPP mode excitation and to study the influence of the graphene layer on the strong coupling regime between the TPP and SPP components. The dependence of the ellipsometric parameter  $\Psi$  ( $\lambda$ ) on the AOI of the PC/SiO<sub>2</sub>/Ag structure is shown in Fig. 4.2.2. The experimental results are presented as circles and the

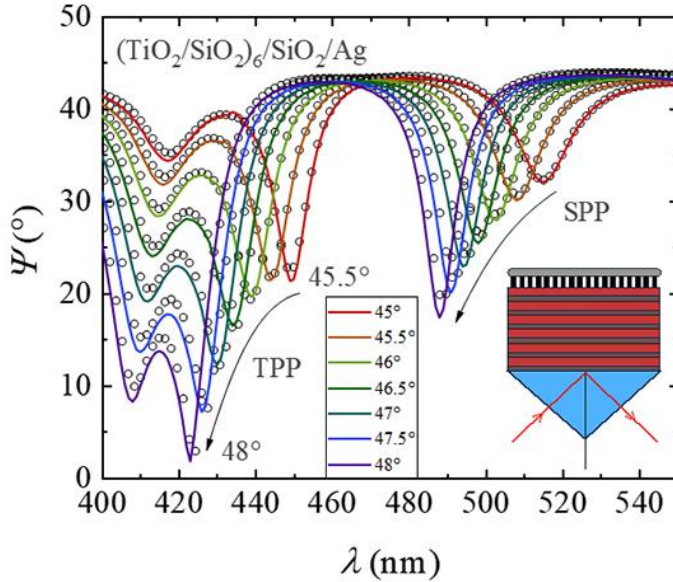


**Figure 4.2.2.** Hybrid TPP-SPP mode ellipsometric parameter  $\Psi$  spectral dependence on the incident angle in a PC/SiO<sub>2</sub>/Ag structure. The dots and solid curves correspond to the experimental and theoretical results, respectively.

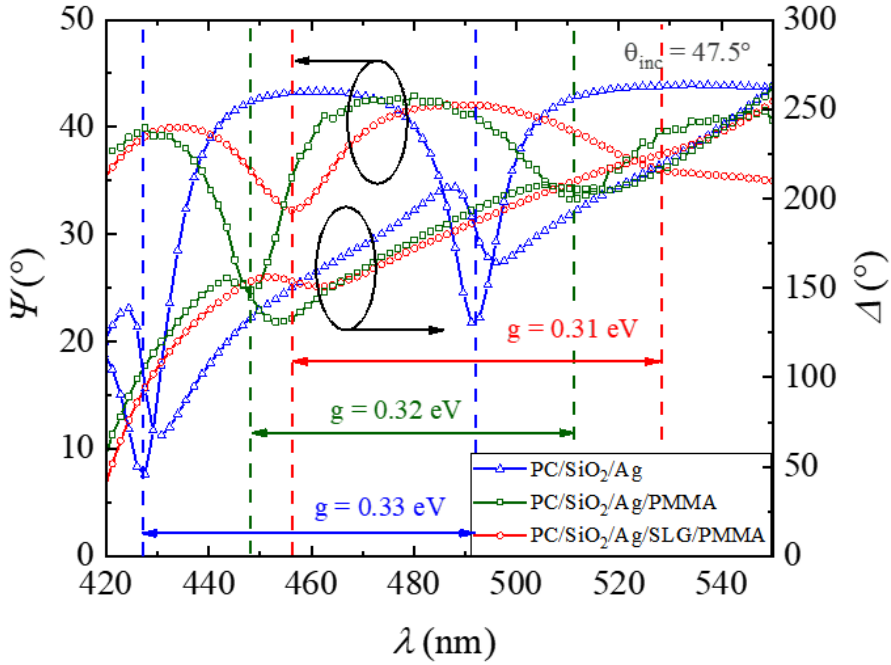


**Figure 4.2.3.** Experimental data of the ellipsometric  $\Psi$  and  $\Delta$  parameters at three different stages of the sample: plain PC/SiO<sub>2</sub>/Ag (blue), after PMMA is added (green), with graphene and PMMA (red). The angle of incidence is 47.5

solid lines show the fitting results. For the TIRE configuration, the same approach of optical model design and regression analysis was applied as for the VASE, taking into consideration the inverse problem of the multi-layer model and the prism coupler. The fitting procedure gave values of the thicknesses, which were very close to those of the VASE. The only corrections involved were due to the glass prism. The contributions of the graphene monolayer to the optical response of the PC/SiO<sub>2</sub>/Ag/SLG/PMMA structure were measured at 47.5° AOI due to the broad gap between the TPP and SPP components in hybrid mode, thus indicating their intense interaction in a strong coupling regime [14].

The experimental TIRE results of the PC/SiO<sub>2</sub>/Ag, PC/SiO<sub>2</sub>/Ag/PMMA and PC/SiO<sub>2</sub>/Ag/SLG/PMMA structures at  $\theta_{inc}=47.5^\circ$  are shown in Fig. 4.2.3. The TPP and SPP excitation dips in ellipsometric parameter  $\Psi$  ( $\lambda$ ) of the PC/SiO<sub>2</sub>/Ag structure (Fig. 4.2.3 blue line) were at 427 nm and 492 nm, respectively. After the PMMA deposition (Fig. 4.2.3 green line) on the top of the PC/SiO<sub>2</sub>/Ag, the hybrid TPP-SPP mode shifted to 448 nm (TPP) and 511 nm (SPP). The red shifts of the TPP and SPP components in their hybrid plasmonic mode were 21 nm and 19 nm, respectively. For the

PC/SiO<sub>2</sub>/Ag/SLG/PMMA structure with the graphene layer between the silver layer and the PMMA (Fig. 4.2.3 red line), the plasmonic components manifested themselves at 456.4 nm (TPP) and 527.7 nm (SPP). The shift to longer wavelengths (29.4 nm (TPP) and 35.8 nm (SPP)) corresponded to those of the PC/SiO<sub>2</sub>/Ag structure. Thus, the difference between the corresponding TPP and SPP resonances with and without the graphene layer were 8.4 nm for the TPP and 16.7 nm for the SPP. The spectral distance, which indicates the coupling strength between the TPP and the SPP excitations in their hybrid mode was 65 nm, 63 nm and 71.3 nm for the PC/SiO<sub>2</sub>/Ag, PC/SiO<sub>2</sub>/Ag/PMMA and PC/SiO<sub>2</sub>/Ag/SLG/PMMA structures, respectively.

The graphene and PMMA layers noticeably modify the optical response of the hybrid TPP-SPP mode and hence change the coupling strength between TPP and SPP components in their hybrid plasmonic mode. In Fig. 4.2.3, the green curve corresponds to the evolution of the hybrid plasmonic component dips due to presence of the PMMA layer on the silver surface. The diminishment of both the TPP and SPP states indicates non-optimal resonance conditions, while the red shift of both resonances can be attributed to an increase of the refractive index due to the PMMA. The red curve in Fig. 4.2.3 shows the optical response of the ellipsometric parameters due to presence of the graphene layer between the silver layer and the PMMA. The graphene layer slightly increases the spectral gap between the TPP and SPP components. At the same time, it weakens the SPP resonance due to changes of metal layer conductivity. It should be noted that the TPP and SPP components in the hybrid TPP-SPP mode show different behavior when the SLG/PMMA layer is deposited on the top of the silver surface. As is well-known [18,20] the TPP and SPP resonances excited at the different interfaces, the TPP at the inner, while the SPP at the outer. Therefore, the SPP is more sensitive to changes of the refractive index on the top of the metal surface, while the changes of the optical response of the TPP is more related to the alteration of the coupling strength between the TPP and SPP in their hybrid TPP-SPP mode.

The graphene transfer via polymer does not permit one to measure the amount of pure graphene on the PC/Ag structures without the PMMA layer. Moreover, as was shown before [38], this variation of the coupling strengths is not directly equal to the change of the general optical response of the system. The conducted evaluation takes into account not only the gap  $\Omega$  (Rabi splitting) between resonances, but also the widths (FWHM) of both resonances. As was shown, the ambiguities in distinguishing between the

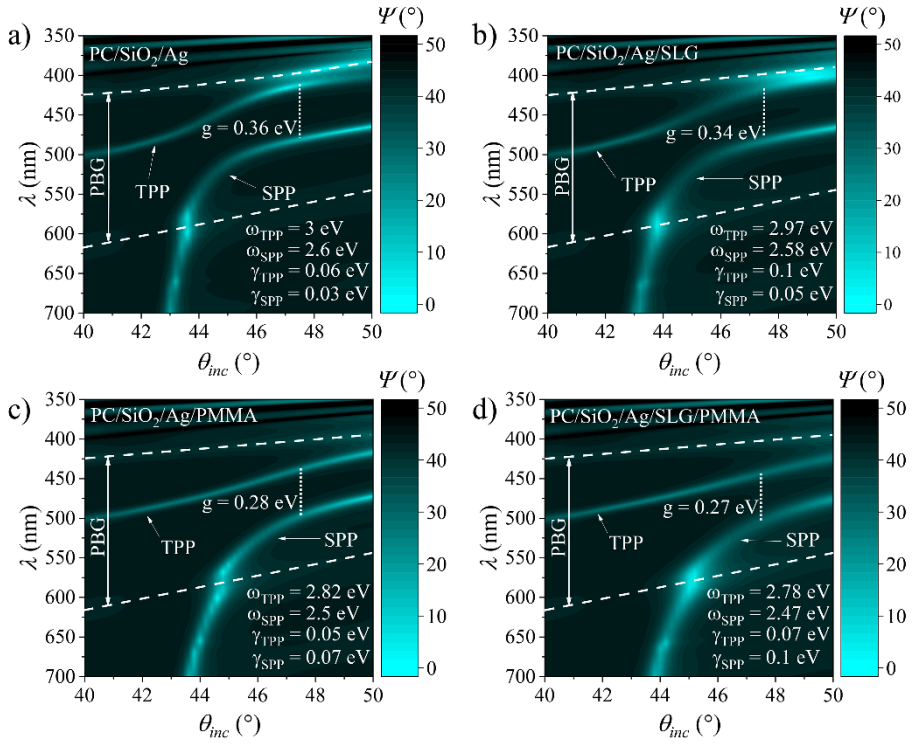


**Figure 4.2.4.** Image plot of the modeled ellipsometric parameter  $\Psi$  of the PC/SiO<sub>2</sub>/Ag (a), PC/SiO<sub>2</sub>/Ag/SLG (b), PC/SiO<sub>2</sub>/Ag/PMMA (c), PC/SiO<sub>2</sub>/Ag/SLG/PMMA (d) samples. The photonic band gap (PBG) edges are marked with the white dashed line. The yellow dot line marks the gap between the TPP and SPP modes.

strong and weak coupling were raised in various systems, especially in the widely studied exciton-plasmon based structures [38,162]. In order to reveal the varying in the coupling strength between TPP and SPP components, we applied the expression proposed in the previously mentioned study:

$$g = \sqrt{\Omega^2 - \frac{1}{4}(\omega_{SPP} - \omega_{TPP})^2}. \quad (4.6)$$

The system is in the strong coupling regime when:

$$g > \frac{1}{4}(\gamma_{SPP} + \gamma_{TPP}), \quad (4.7)$$



$$\Gamma = \frac{1}{4}(\gamma_{SPP} + \gamma_{TPP}). \quad (4.8)$$

Where  $g$  is the coupling strength,  $\Omega$  is the Rabi splitting,  $\omega_{SPP}$  and  $\omega_{TPP}$  – SPP and TPP are the resonance positions in the spectra,  $\gamma_{SPP}$  and  $\gamma_{TPP}$  are the corresponding widths of the resonances. According to these evaluations, the strong coupling regime were estimated for all three cases of experimentally studied multi-layered structures as being: PC/Ag ( $g = 0.33$  eV;  $\Gamma = 0.034$  eV;  $\omega_{TPP} = 2.9$  eV;  $\omega_{SPP} = 2.5$  eV;  $\gamma_{TPP} = 0.1$  eV;  $\gamma_{SPP} = 0.06$  eV), PC/Ag/PMMA ( $g = 0.32$  eV;  $\Gamma = 0.052$  eV;  $\omega_{TPP} = 2.7$  eV;  $\omega_{SPP} = 2.3$  eV;  $\gamma_{TPP} = 0.08$  eV;  $\gamma_{SPP} = 0.14$  eV) and PC/Ag/SLG/PMMA ( $g = 0.31$  eV;  $\Gamma = 0.053$  eV;  $\omega_{TPP} = 2.7$  eV;  $\omega_{SPP} = 2.4$  eV;  $\gamma_{TPP} = 0.1$  eV;  $\gamma_{SPP} = 0.11$  eV). The obtained results have shown that such changes in the optical response of hybrid mode were sensitive enough to distinguish the variation of coupling strength being contributed by the graphene layer. It should be noted that the general optical response of the system masks the variations of the coupling strength.

Additionally, to reveal the contribution of the graphene single layer and PMMA to the coupling strength in the hybrid TPP-SPP mode, numerical simulations were performed. This evaluation was conducted using the same parameters of the model structure as in the TIRE experiment. The map of the ellipsometric parameter  $\Psi$  was chosen, because the plasmonic minima of TPP and SPP in  $\Psi(\lambda)$  resemble the minima observed in the reflectance intensity of the plasmonic resonances. The shape of these minima in  $\Psi$  is close to the square root of the plasmonic reflectance, which indicates that the  $\Psi$  minima, in fact, are sharper than corresponding plasmonic minima in reflectance [163]. This advantage gives more precise detection of the gap and the widths of the TPP and SPP components in the hybrid mode, which have an influence to the coupling strength. The dependence of the ellipsometric parameter  $\Psi(\lambda)$  on the angle of incidence was modeled (Fig. 4.2.4), which allowed an estimation of the dispersion relation of the hybrid TPP-SPP mode. The spectral gap between the components in the hybrid mode for the PC/SiO<sub>2</sub>/Ag, PC/SiO<sub>2</sub>/Ag/SLG, PC/SiO<sub>2</sub>/Ag/PMMA and PC/SiO<sub>2</sub>/Ag/SLG/PMMA structures were evaluated at  $\theta_{inc} = 47.5^\circ$  and was found to be 68.5 nm, 67.3 nm, 59.4 nm and 60.7 nm, respectively. These calculation results clearly demonstrated that both resonances were red-shifted after the graphene and PMMA deposition. The evaluated coupling strength between the TPP and SPP components weakened due to the graphene layer ( $g = 0.34$ ;  $\Gamma = 0.038$ ) (Fig. 4.2.4 b). In Fig. 4.2.4 c the decreased bending of dispersion curves was observed and the evaluated coupling strength was ( $g = 0.28$ ;  $\Gamma = 0.03$ ). When the analyzed structure contained the SLG/PMMA layers (Fig. 4.2.4(d)), the

Rabi splitting  $\Omega$  and the widths of both resonances increase, what leads to the decrease of the coupling strength for ( $g = 0.27$ ;  $\Gamma = 0.043$ ). Despite the fact that the dispersion curves of the TPP and SPP components slightly increased for the SLG/PMMA structure, both excitations were diminished, and the widths of the resonances became wider (Fig. 4.2.4 d). The coupling strength also slightly decreased. As can be seen in graphs Fig. 4.2.4 c and d, the bending of the TPP and SPP dispersion branches diminishes, however, the strong coupling conditions were still satisfied for Fig. 4.2.4 c and d. This decrease of the TPP and SPP dip components in the TPP-SPP hybrid mode can be explained by changes of the conductivity of the silver layer due to the addition of the SLG/PMMA structure and, as a result, the creation of non-optimal resonance conditions for the hybrid plasmonic mode. The numerical calculations and the evaluation of the coupling strengths for equations 4.6 and 4.7 clearly show the hybrid origin of the coupled TPP and SPP optical states. The modified positions of the TPP and SPP components in the wavelength spectra, compared with their original, separate excitations, indicate the strong coupling regime [14]. The alteration of the splitting modes (the gap between the TPP and SPP dips and the widening of the resonances) indicate a variation of the coupling strength  $g$  [14]. In TIRE configuration, the TPP and SPP states cannot be generated separately at a given angle or wavelength. Hence, both excitations are in superposition and satisfy the same wave equation [18]. This leads to the hybrid modes and the coupling of the TPP and SPP.

### Summary

Summarizing, the TIRE method was used for the generation and study of the hybrid TPP-SPP modes on a PC structure with a thin layer of silver and SLG/PMMA. Raman spectroscopy showed the presence of a consistent graphene monolayer on the Ag layer. Recent studies have shown that noticeable changes in the general optical response can have a rather weak impact on strong coupling. Despite of this, the variation of the coupling strength between the PMMA and SLG/PMMA structures in the hybrid plasmonic mode was big enough to evaluate the differences between them. The higher sensitivity was achieved in the hybrid TPP-SPP plasmonic mode, than during the single TPP optical state excitation, due to the optical response to the PMMA and SLG/PMMA. The analysis of the in-plane wave vector, which the plasmonic mode gives, allows one to obtain more sensitive optical responses from such graphene-based hybrid nanostructures. The widening of the TPP and SPP resonance width weakens the coupling strength and decreases the Q-factor. Moreover, the monitoring of the coupling strength

between the TPP and SPP components gives additional information about the optical responses of such hybrid optical devices.

## 4.3 Application of hybrid tamm plasmon-surface plasmon polaritons modes to biosensing

### 4.3.1 Introduction

Surface plasmon resonance (SPR) electromagnetic waves have become one of the most widely used indicators for the detection of interactions between various biomolecules on solid-liquid interfaces [59,164]. The label-free, high sensitivity and real time monitoring ability of this optical signal makes SPR a very attractive tool for the evaluation of antibody-antigens [165], the assessment of regulatory protein interactions with cell receptors [166], allergen detection in food [167], immunosensors [168], the validation of protein-based drugs [141,169] and for many other uses. Plasmonic-based optical sensors can also be used for the detection of various gases [88,170]. High sensitivity is achieved due to the strong localization of the electric field at the metal/dielectric interface when resonance conditions for such light-matter interaction are satisfied [1]. However, the rather broad width of such SPR resonances, caused by large absorption and scattering losses in the metal layer, limits the further improvement of the sensitivity of this type of optical sensors.

The sensitivity could be enhanced by reducing losses in metal. This can be done by using hybrid TPP-SPP modes, if the conditions are satisfied for both TPP and SPP excitations – the anti-crossing effect of their dispersion curves [18]. The repulsion of these dispersion curves changes the dispersion relation of both components in the hybrid TPP-SPP plasmonic mode and, as a result, reduces the losses of the SPP resonance, which become narrower compared with that of the SPR. This anti-crossing effect indicates a strong coupling regime and the presence of a hybrid TPP-SPP mode in which the TPP state exchanges energy with the SPP state [14]. The excitation of hybrid TPP-SPP plasmonic mode requires conditions of total internal reflection and these states are polarization sensitive. A detailed analysis of the polarization properties in a TIR setup can be achieved by using total internal reflection ellipsometry (TIRE) [163] and spectroscopic ellipsometry setup in TIR configuration is very useful for the monitoring of the interaction between proteins at solid/liquid interfaces [171,172].

Recently, some attempts have been made to apply the Tamm plasmons polaritons effect to optical sensors [77,173]. These applications, however, were dedicated for the most part to sensing gases [173] or temperature [75], or for processes which occurs inside the photonic crystal at the interface of the PC and the metal [174]. Single TPP states are not very suitable for the

detection of biological processes, which, in most cases, occur at the outer interface (metal/dielectric ambient). However, if the hybrid TPP-SPP mode is applied, the SPP component acts as a direct probe.

In this study, the hybrid TPP-SPP mode was applied for sensing of protein layer formation. The increased sensitivity of the ellipsometric parameters in the TIRE configuration, due to the changes of the two strongly coupled plasmonic excitations were monitored, analyzed and compared with that of a conventional single SPR. The TIRE method was used for the excitation and study of the sensitivity properties of the hybrid TPP-SPP and single surface plasmon resonance (SPR) modes of the GCSF receptor immobilization. Additionally, the optimized sensitivity of the hybrid TPP-SPP mode was investigated and compared with the single SPR mode when the BSA proteins formed a layer on the gold surface. The dispersion relations for the hybrid TPP-SPP and single SPR modes were used to explain the enhanced sensitivity of the ellipsometric parameters for the hybrid TPP-SPP mode over the conventional SPR. The SPP component of the hybrid TPP-SPP mode was about 6.4 times more sensitive than single SPR for the BSA protein layer on the gold film. It was found that the sensitivity of the hybrid plasmonic mode can be made controllable by using the strong coupling effect between the TPP and SPP components. The strong coupling regime reduces absorption and scattering losses of the metal for the SPP component in the hybrid TPP-SPP mode and, as a result, narrows the plasmonic resonance.

The results presented in the following Chapter were originally published in: E. Buzavaite-Verteliene, I. Plikusiene, T. Tolenis, A. Valavicius, J. Anulyte, A. Ramanavicius and Z. Balevicius. "Hybrid Tamm-surface plasmon polariton mode for highly sensitive detection of protein interactions" *Optics Express* **28**(20), 2020, pp. 29033-29043. <https://doi.org/10.1364/OE.401802>.

#### 4.3.2 TIRE for detection of GCSF-R immobilization on surface

In this research two different samples were investigated: a commercially available SPR chip for the excitation of SPP and nanophotonic structure consisting of distributed Bragg reflector (1D PC) with thin (40 nm) gold layer, supporting hybrid TPP-SPP modes. The single SPR and hybrid TPP-SPP measurements were conducted in total internal reflection (TIR) geometry, using a half-cylinder prism made of BK-7 glass (Fig. 4.3.1). The half-cylinder prism has been cut at the base of it and the 1 mm thick glass slide was attached through refractive index matching liquid. To ensure there are no refraction of incident light, two plano concave lenses with the same radius curvature as the

prism envelope were attached to the prism via refractive index matching liquid. Thus, the incoming light is always incident normal to the prism surface. The GCSF-R immobilization measurements were conducted at  $70^\circ$  angle of incidence (AOI) and  $62.5^\circ$  for the SPR and hybrid TPP-SPP modes, respectively, while the adsorption of BSA was performed at  $70^\circ$  AOI and  $64.6^\circ$  for SPR and hybrid TPP-SPP, respectively. For the BSA adsorption the hybrid TPP-SPP mode was optimized by selecting the angle of incidence so that the in-plane wavevector of the incident photons best matched the oscillations of the energy of the free electrons at the surface of the metal layer. When the plasmon dip in the reflectance spectra of ellipsometric parameters dropped to a near zero value, it had reached these optimized conditions.

The TIRE measurements were first conducted in order to determine the optical response of the GCSF receptor on the standard SPR chip, which were obtained only from the thin (45 nm) gold layer. The PC/Au nanostructure was also tested with the same receptor. The single SPR and the hybrid TPP-SPP excitations manifested themselves as dips in the ellipsometric spectra of  $\Psi(\lambda)$  and the enhanced amplitude of the  $\Delta(\lambda)$ . The single SPR resonance TIRE optical response of parameters  $\Psi(\lambda)$  and  $\Delta(\lambda)$  to GCSF-R can be seen in Fig. 4.3.2 a and Fig. 4.3.2 b. Before injecting the GCSF-R, the dip of the SPR resonance was at 689.7 nm and after incubation of GCSF-R, the resonance red-shifted to 702.3 nm. The value of ellipsometric parameter  $\Psi$  at the fixed wavelength  $\lambda=677.4$  nm was  $10.4^\circ$  to  $18.7^\circ$  before and after the GCSF-R immobilization. This difference was equal to  $\delta\Psi=8.3^\circ$ . The value of the

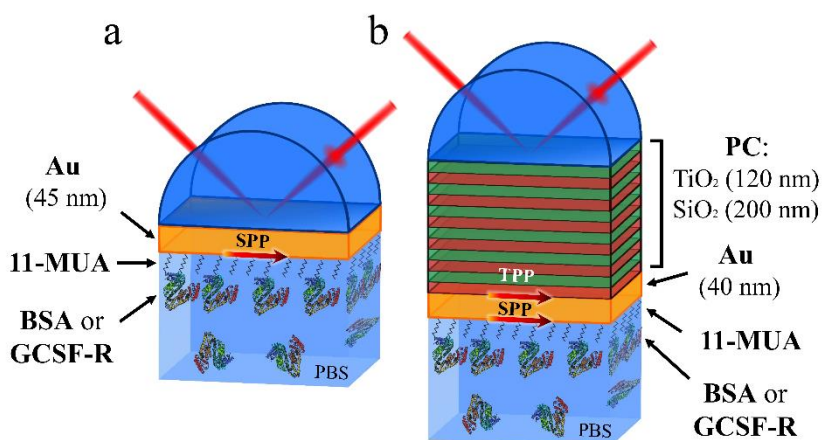


**Figure 4.3.1.** Total internal reflection geometry schematic of the Au (left) and PC/Au (right) samples with a self-assembling monolayer (11-MUA) and the GCSF-R or BSA protein in PBS solution.

ellipsometric parameter  $\Delta$  (Fig. 4.3.2 b) at fixed 697.3 nm wavelength was equal to  $357.8^\circ$  and  $201^\circ$  before and after the GCSF-R immobilization, respectively. The difference was  $\delta\Delta=156.8^\circ$  for the single SPR. The shift of the single SPR to longer wavelengths was determined to be  $\delta\lambda=12.6$  nm. The dips of the TPP and SPP for the hybrid TPP-SPP mode (Fig. 4.3.2 c) corresponded to 762 nm, 763 nm, 867.5 nm and 873.7 nm for TPP and SPP components before and after the immobilization of the GCSF receptor, respectively. The value of  $\Psi$  in a hybrid TPP-SPP mode was equal to  $29.6^\circ$  and  $35.4^\circ$  at  $\lambda=760$  nm for the TPP and  $14.6^\circ$  and  $24.4^\circ$  at  $\lambda=861.6$  nm for the SPP components, before and after the GCSF-R immobilization, respectively. As for the  $\Delta$  parameter (Fig. 4.3.2 d), it was equal to  $281^\circ$  and  $238.5^\circ$  for the TPP and  $282.2^\circ$  and  $225.8^\circ$  for the SPP components before and after GCSF-R immobilization, respectively.

The ellipsometric spectra of the both samples, before and after surface modification by the GCSF receptor, were compared (Fig. 4.3.2), in the vicinity of plasmonic resonances where the contribution to the optical response was the greatest. A red shift of  $\delta\lambda=3$  nm and  $\delta\lambda=6.2$  nm in the ellipsometric spectra  $\Psi(\lambda)$  and  $\Delta(\lambda)$  was observed in the TPP-SPP hybrid mode for the TPP and SPP components, respectively. Such spectral shifts of the hybrid TPP-SPP resonances produce the following changes in the ellipsometric parameters:  $\delta\Psi=5.8^\circ$  and  $\delta\Delta=42.5^\circ$  for TPP;  $\delta\Psi=9.8^\circ$  and  $\delta\Delta=56.4^\circ$  for the SPP components. It has been shown [124] that the TIRE method, due to the phase measurements  $\Delta$ , has a higher sensitivity than the traditional p-polarized reflected light intensity detection of the SPR. Moreover, it is worth noting that even the p- and s-polarization amplitudes ratio  $\Psi$  has higher sensitivity, than the reflection intensity measurements. This is because  $\Psi$  is close to the square root of the SPR-reflectance. Because of this, the plasmonic resonance in the ellipsometric parameter  $\Psi$  is sharper, than the corresponding SPR in the reflection intensity spectra [171]. The origin of a rather wide SPR minimum, however, is determined by losses in the metals, which are necessary for the plasmonic wave's generation. At the same time, for the hybrid TPP-SPP mode, the SPP component become narrower due to the repulsion (anti-crossing) of the TPP and SPP dispersion curves, which indicates a decrease of the losses. In other words, the SPP component is pushed more away from metal layer to the dielectric, compared with the traditional SPR.

In order to determine the sensitivity properties of the hybrid TPP-SPP mode and single SPR, an analysis of the dispersion relations of both excitations was conducted. Numerical calculations were performed in order to

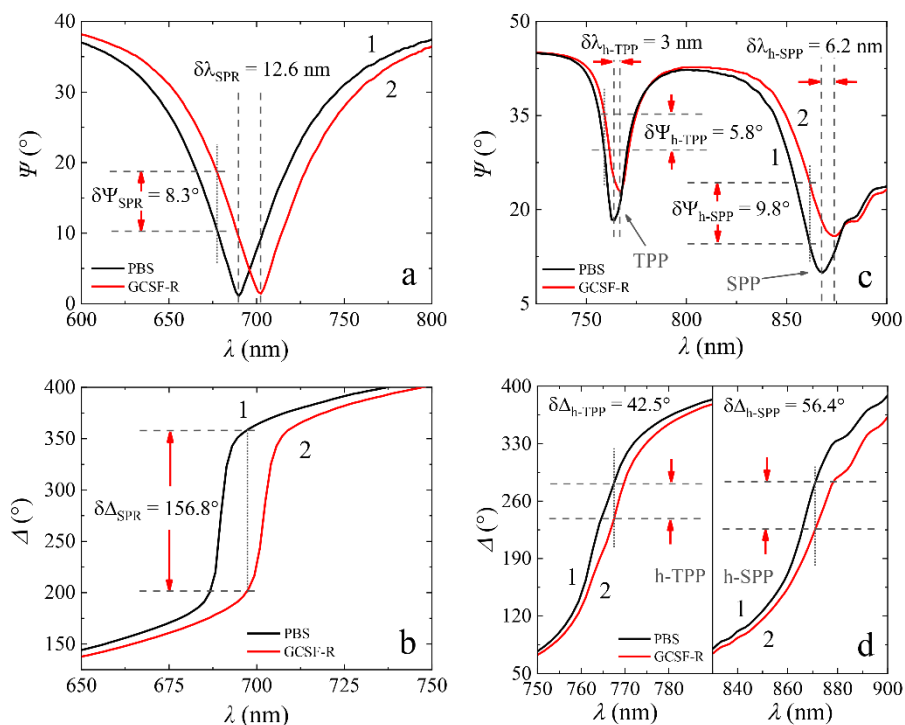


**Figure 4.3.2.** Spectra of ellipsometric parameters (a) -  $\Psi(\lambda)$  and (b) -  $\Delta(\lambda)$  for single SPR and for the hybrid TPP-SPP mode (c) -  $\Psi(\lambda)$  and (d) -  $\Delta(\lambda)$ , curve 1 – base line registered in PBS (pH 7.4), curve 2 – after immobilization of GCSF-R protein for 45 min.

show the differences in the sensitivity of the hybrid TPP-SPP mode and SPR on both sample surfaces that were immobilized on the GCSF receptor (Fig. 4.3.3 a - b). Calculation was conducted using the same parameters of the model structure as in the TIRE experiment for BK-7 glass/Cr/Au (single SPR) and BK-7 glass/PC/Au (hybrid TPP-SPP). Also, parameters for both samples were taken at the same time as in the experiment. The experimental results and simulations showed the stronger dependence of the wavelength shift on the angle of incidence for the SPR, than that for the hybrid TPP-SPP mode (Fig. 4.3.3 b). However, a considerably thinner dispersion line can be seen for the hybrid TPP-SPP mode, than for the SPR (Fig. 4.3.3 a), especially for the bigger AOIs. This effect increases the sensitivity of the ellipsometric parameters  $\Psi(\lambda)$  and  $\Delta(\lambda)$ . For the hybrid TPP-SPP mode, the  $\delta\Psi_{h-SPP}/\delta\lambda = 9.8^\circ/6.2 \text{ nm} \approx 1.58^\circ/\text{nm}$ ,  $\delta\Delta_{h-SPP}/\delta\lambda = 56.4^\circ/6.2 \text{ nm} \approx 9.1^\circ/\text{nm}$ ,  $\delta\Psi_{h-TPP}/\delta\lambda = 5.8^\circ/3 \text{ nm} \approx 1.9^\circ/\text{nm}$ ,  $\delta\Delta_{h-TPP}/\delta\lambda = 42.5^\circ/3 \text{ nm} \approx 14.2^\circ/\text{nm}$ . Meanwhile for the single SPR mode, the



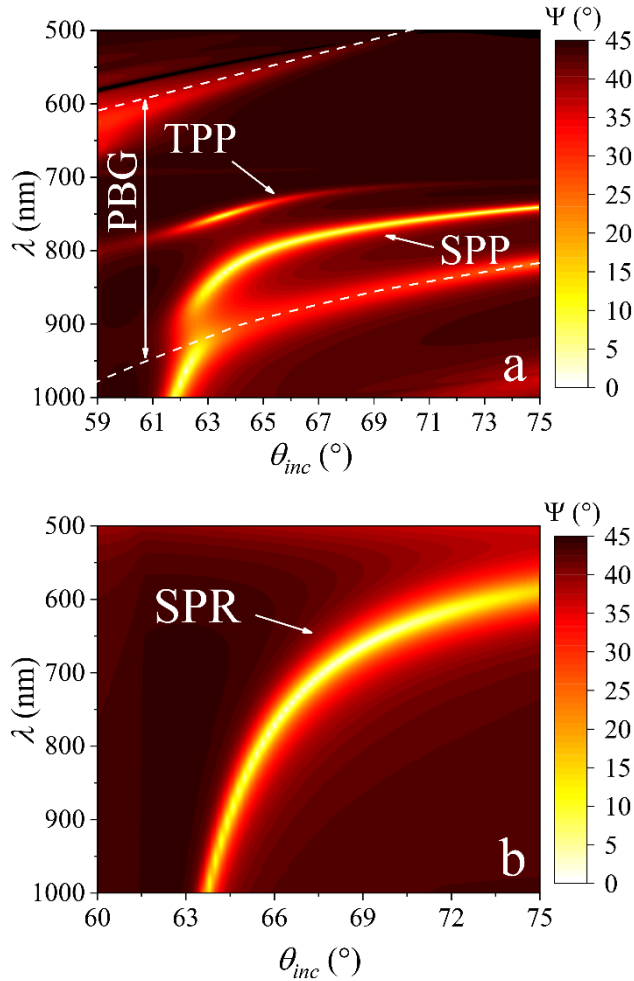


**Figure 4.3.3.** Comparison of the numerically calculated dispersion relations of the hybrid TPP-SPP mode (a) generated in the PC (TiO<sub>2</sub>/SiO<sub>2</sub> (120 nm/200nm))/Au (40 nm) structure and for the single SPR mode (b) in a Cr/Au (50nm) structure

$\delta\Psi_{\text{SPR}}/\delta\lambda = 8.3^\circ/12.6 \text{ nm} \approx 0.66^\circ/\text{nm}$ ,  $\delta\Delta_{\text{SPR}}/\delta\lambda = 156.8^\circ/12.6 \text{ nm} \approx 12.4^\circ/\text{nm}$  were registered. From the obtained values, we can clearly define that the relative sensitivity of the SPP component in its hybrid plasmonic mode overtakes the traditional SPR. However, the absolute changes of the ellipsometric parameter  $\Delta(\lambda)$  in the SPR are still bigger than that of the hybrid TPP-SPP mode. This can be explained by the non-optimized sensitivity of the SPP component in the hybrid mode. The depths of the minimums in  $\Psi$  were better for the SPR, than for the SPP component (Fig. 4.3.2 a and c). The

advantage of the single SPR is its sensitivity to the resonant wavelength shift in the spectra, which is related to changes of the wave vector when any processes occur at the sensing surface in which the refractive index of the medium changes [48,175]. In the hybrid TPP-SPP mode, attention should be paid to the TPP component, which pushes the SPP component away from the metal layer, thus decreasing the losses of SPP. The TPP component can also be used for the indirect monitoring of the processes which occur on the outer side of the gold layer. Having lower losses than the SPP excitation due to their origin, the TPP shares some features that are similar to the Bloch surface waves (BSW). It has been shown that the BSW can have comparable or even better sensitivity than the traditional SPR, due to the low losses in dielectric structures without metals [176]. In the TPP, these lower losses are obtained because a major part of surface wave is propagated in the dielectric layer of the PC at the interface with the metal layer. Thus, since a smaller part of the TPP penetrates into the metal, the resonance becomes narrower and leads to rather higher sensitivity. However, the main disadvantage of the TPP in practical biosensing applications is that these optical states excite at the inner interface between the metal and the last layer of the PC (Fig. 4.3.1) and as a result, are not directly accessible at the sensing surface (the outer interface). Therefore, the employment of the hybrid TPP-SPP mode for sensing exploits the TPP component in a strong coupling regime [20] much better, where one more indirect probe can provide additional information about the processes occurring on the sensing surface.

#### 4.3.3 Hybrid Tamm-surface plasmon polaritons mode for enhanced optical response of biosensor

In order to investigate the sensitivity capabilities of the hybrid TPP-SPP mode, the BSA protein was used as a model system in an optimized optical scheme. To achieve the best sensitivity, the plasmonic minimums for both the hybrid TPP-SPP and the single SPR samples needed to be as deep as possible. For the single SPR, this could be achieved by tuning the plasmon active metal layer (gold) or wavelength and/or angle of incidence at a fixed metal layer, which is a common situation in a real experiment. For hybrid TPP-SPP mode, an additional sensitivity tuning option had to be used. This was through the varying of the strong coupling effect, which allowed one to change the width of the SPP component by moving the TPP part closer to the SPP, so that the latter reached its deepest minimum and become narrower at the same time. The optical responses of the single SPR and the hybrid TPP-SPP modes for BSA immobilization were then compared at optimized conditions at 70° and

64.6° AOI, respectively. The optimized TIRE measurements of the BSA proteins showed that the hybrid SPP component and single SPR, manifesting themselves as the minimums in the ellipsometric spectra  $\Psi(\lambda)$ , were excited at 803.1 nm and 691.4 nm, respectively (Fig. 4.3.4 a and c). The 100  $\mu\text{g/mL}$  of BSA was then injected into the cuvette. Due to the binding of the BSA protein to the gold surface modified with the SAM and activated by the EDC-NHS, a BSA layer was formed. The ellipsometric parameters  $\Psi(\lambda)$  and  $\Delta(\lambda)$  of this were red shifted to 804.6 nm for the hybrid TPP-SPP mode and 697.6 nm for the SPR, respectively. Such a shift in the resonance wavelengths  $\delta\lambda_{\text{h-SPP}}=1.5$  nm and  $\delta\lambda_{\text{SPR}}=6.2$  nm gave corresponding changes in the hybrid SPP ellipsometric parameters  $\delta\Psi_{\text{h-SPP}}=3.7^\circ$ ,  $\delta\Delta_{\text{h-SPP}}=80.8^\circ$ ; for single SPR, this was  $\delta\Psi_{\text{SPR}}=3.8^\circ$ ,  $\delta\Delta_{\text{SPR}}=51.9^\circ$ . Thus, the detection sensitivity estimated from the data in figures 4 were equal to  $\delta\Psi_{\text{h-SPP}}/\delta\lambda=3.7^\circ/1.5\text{ nm}\approx 2.47^\circ/\text{nm}$ ,  $\delta\Delta_{\text{h-SPP}}/\delta\lambda=80.8^\circ/1.5\text{ nm}\approx 53.9^\circ/\text{nm}$  for the hybrid SPP component and

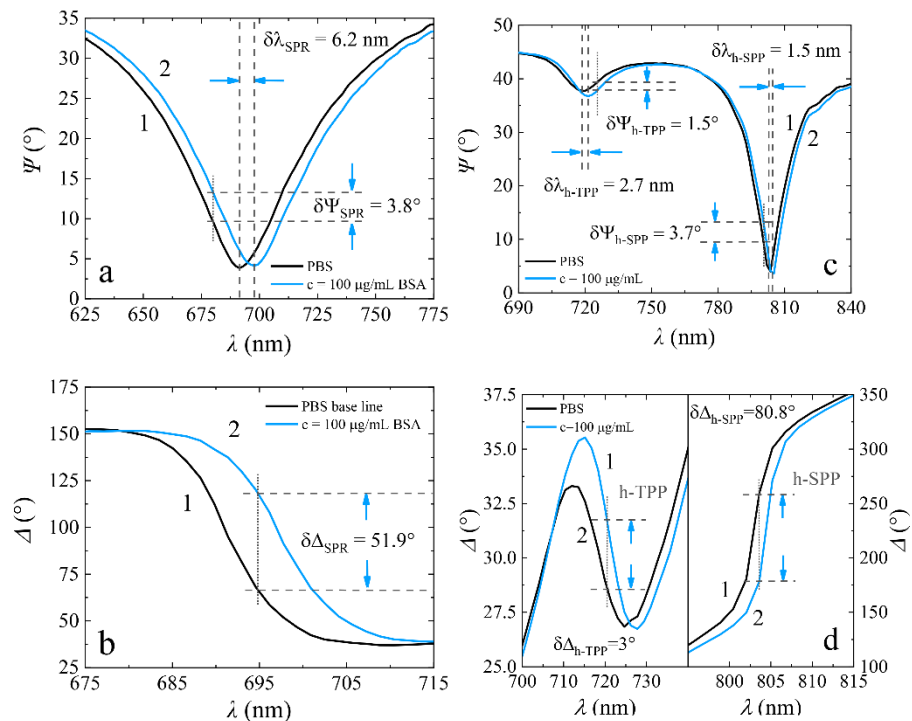


**Figure 4.3.4.** Spectra of ellipsometric parameters (a) -  $\Psi(\lambda)$  and (b) -  $\Delta(\lambda)$  for single SPR and for the hybrid TPP-SPP mode (c) -  $\Psi(\lambda)$  and (d) -  $\Delta(\lambda)$ , curve 1 – base line registered in PBS (pH 7.4), curve 2 – after incubation in 100  $\mu\text{g/mL}$  of BSA for 45 min.

$\delta\Psi_{\text{SPR}}/\delta\lambda=3.8^\circ/6.2\text{nm}\approx 0.61^\circ/\text{nm}$ ,  $\delta\Delta_{\text{SPR}}/\delta\lambda=51.9^\circ/6.2\text{ nm}\approx 8.4^\circ/\text{nm}$  for the single SPR. It can be clearly seen from figure 4 and its evaluated sensitivities that the hybrid TPP-SPP mode with the optimized sensing features of its SPP component overcomes the sensitivity of single SPR based sensors.

For biosensing applications, the layer thickness  $d$  and refractive index  $n$  of the layer obtained from the TIRE spectra is usually converted to the surface mass  $\Gamma$  which is attached to the sensor surface by means of the Feiter's formula [177]:

$$\Gamma = \frac{d(n - n_{\text{buffer}})}{dn/dC} \times 100. \quad (4.9)$$

This expression was used to evaluate the surface mass ( $\text{ng}/\text{cm}^2$ ), where  $dn/dC = 0.17\text{ cm}^3/\text{g}$  is the refractive index increment [178] for the layer material, depending on the protein concentration in the buffered solution,  $d$  and  $n$  are the thickness (nm) and refractive index of the protein layer obtained from regression analysis and  $n_{\text{buffer}}$  is the refractive index of the buffered solution.

The evaluated surface mass for the conducted TIRE experiments of the GCSF-R and BSA are summarized in Table 3 and are presented in  $\text{ng}/\text{cm}^2$ . The refractive index of the PBS was  $n=1.3335$  and  $n=1.3307$  at the wavelengths  $\lambda=632.8\text{ nm}$  and  $\lambda=803\text{ nm}$ , respectively. Both parameters, the film thickness and refractive index were determined from the regression analysis of the experimental TIRE data.

**Table 3.** Calculated thickness  $d$ , refractive index  $n_{\text{prot}}$ , surface mass  $\Gamma$  and experimental values of the ellipsometric  $\Psi$  and  $\Delta$  parameters of the BSA and GCSF-R layers formed on the thin gold layers of samples Cr/Au and PC/Au.

	$d$ (nm)	$n_{\text{prot}}$	$\Gamma$ ( $\text{ng}/\text{cm}^2$ )	$\delta\Psi$ ( $^\circ$ )	$\delta\Delta$ ( $^\circ$ )
SPR <sub>BSA</sub>	5.9	1.3632	103	3.8	51.9
TPP-SPP <sub>BSA</sub>	3	1.3607	53	3.7	80.8
SPR <sub>GCSF-R</sub>	12	1.3632	210	8.3	156.8
TPP-SPP <sub>GCSF-R</sub>	12.7	1.3607	224	9.8	56.4

## Summary

The TIRE method was used for the excitation and study of the sensitivity properties of the hybrid TPP-SPP and single SPR modes of the GCSF receptor immobilization. The optimized sensitivity of the hybrid TPP-SPP mode was investigated and compared with the conventional SPR mode when the BSA proteins formed a layer on the modified gold surface. The experimental data and the numerical calculations of the dispersion relations for the hybrid TPP-SPP and single SPR modes were used to explain the enhanced sensitivity of the ellipsometric parameters for the hybrid TPP-SPP mode over the conventional SPR. Specifically, the SPP component ( $\delta\Delta_{h-SPP}/\delta\lambda=53.9^\circ/\text{nm}$ ) of the hybrid TPP-SPP mode was about 6.4 times more sensitive than conventional SPR ( $\delta\Delta_{SPR}/\delta\lambda=8.4^\circ/\text{nm}$ ) in the case of the BSA protein immobilization, thus allowing detection of lower concentrations. It was found that the sensitivity of the hybrid plasmonic mode can be made controllable by using the strong coupling effect between the TPP and SPP components. This reduces the metal losses of the SPP component and, as a result, narrows the plasmonic resonance. Moreover, by employing the TPP resonance as an indirect probe, this in some cases can provide additional information, which is useful for the analysis of adsorption processes at the interfaces. The employing of hybrid TPP-SPP mode for strong interaction with excitons in various labelled proteins, light harvesting complexes and organic layers are promising platform for the advanced study of interaction between proteins.

## 4.4 Application of tamm plasmons and cavity modes for biosensing in combined spectroscopic ellipsometry and quartz crystal microbalance method

### 4.4.1 Introduction

The combination of different sensing methods on one platform has become a growing interest for advanced sensing technologies [179–181]. The possibility to perform simultaneous signal monitoring with different sensing methods on the same platform opens possibilities to gain more precise and deeper information about the investigated process [179,182]. One of the sensing methodologies which combine the two methods on the same sensing platform is spectroscopic ellipsometry (SE) and quartz micro balance with dissipation (QCM-D) method [183,184]. The combination of these two methods has been widely used for studies of thin polymer layers [185,186] and others. The main advantage of this combined method is that the thickness of the formed layer on the surface of gold can be evaluated by both methods [184].

However, the nanometric gold layers are widely employed for nanophotonic devices with planar profiles [187] and plasmonic based optical biosensing, such as SPP that significantly improves sensitivity of the method [59], but requires a prism coupler. Thus, all advances given by TIR configuration are not available for spectroscopic ellipsometry in combination with QCM-D, because SE is used in the conventional configuration and as a result the sensitivity of SE part is significantly smaller than plasmon based optical methods [49]. The signal can be enhanced by introducing 1D photonic crystal (PC) structure with thin metal layer that supports Tamm plasmon polaritons. The advantage of simple [73] excitation configuration of TPP, makes them useful to enhance the optical signal at the surface of the modified QCM-D sensor chip for the optical response of ellipsometric parameters.

In this study, the 1D plasmonic nanophotonic structures, supporting Tamm plasmon polariton together with cavity modes, were generated on the modified QCM-D chip and was applied for sensing of protein layer formation in the combinatorial spectroscopic ellipsometry and quartz crystal microbalance method. The increased sensitivity of the ellipsometric parameters  $\Psi(\lambda)$  and  $\Delta(\lambda)$  due to the excitation of Tamm plasmon polaritons and cavity modes were monitored, analyzed and compared with that of a conventional SE combined with QCM-D. This study showed that Tamm plasmon and cavity modes exhibits about 23 and 49 times, respectively, better performance of ellipsometric parameters for refractive index sensing, than the standard

spectroscopic ellipsometry on QCM-D sensor chip. The different origin of Tamm plasmon polaritons (TPP) and cavity mode (CM) gives additional advances and can determine whether the surface (TPP) or bulk process (CM) is dominating.

The results presented in the following Chapter were originally published in: I. Plikusienė, E. Bužavaitė-Vertelienė, V. Mačiulis, A. Valavičius, A. Ramanavičienė and Z. Balevičius. “Application of Tamm Plasmon Polaritons and Cavity Modes for Biosensing in the Combined Spectroscopic Ellipsometry and Quartz Crystal Microbalance Method” *Biosensors* **11**(12), 2021, pp. 501. <https://doi.org/10.3390/bios11120501>.

#### 4.4.2 Refractive index sensing

The optical response of ellipsometric parameters  $\Psi(\lambda)$  and  $\Delta(\lambda)$  in such modified structure have shown the presence of the Tamm plasmon polariton optical states and resonant cavity modes in the Bragg mirror between two gold layers. In order to analyze in details such optical response the spectroscopic

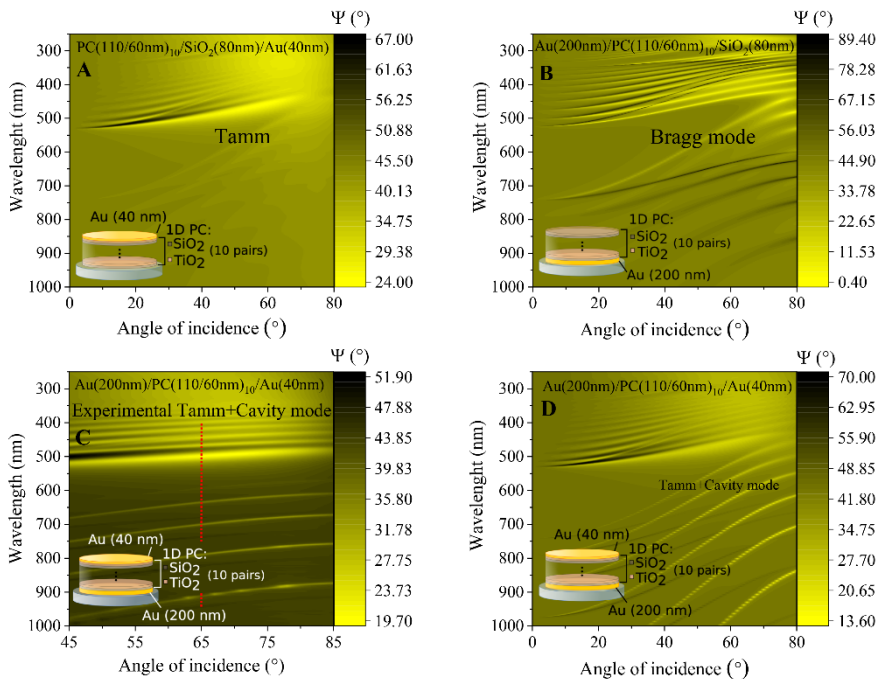


**Figure 4.4.1.** Dispersion relations of calculated TPP (a), cavity mode (CM) (b) and TPP+CM (d) and an experimental dispersion of the investigated modified QCM-D sensorchip, supporting TPP and CM (c). Red dashed line in (c) marks a cross-section at  $\theta_i=65^\circ$ .

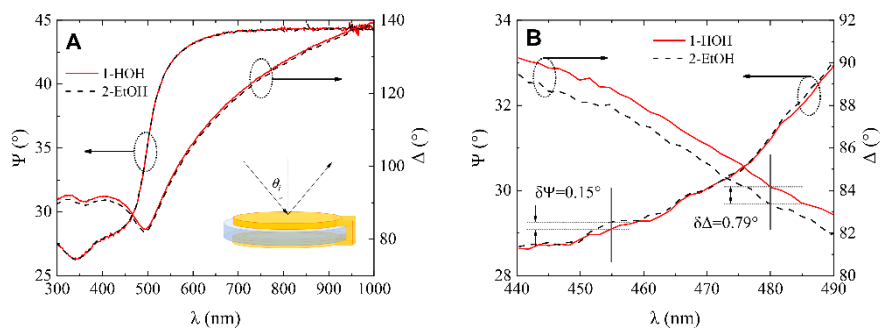


**Figure 4.4.2.** Ellipsometric parameters  $\Psi$  and  $\Delta$  (a) and zoomed view (b) of ellipsometric parameters dependence on wavelength  $\lambda$  for 1- QCM-D chip in water (red curves), 2- QCM-D chip in ethanol (dashed curves) with sensitivity parameters  $\delta\Psi$  and  $\delta\Delta$ .

ellipsometry measurements firstly were conducted in the air ambient to determine the optical dispersion of QCM-D sensor chip modified with 1D PC made from ten bilayers of  $\text{TiO}_2/\text{SiO}_2$  and a thin (40 nm) gold layer on the top. Variable angle spectroscopic ellipsometry measurements were performed in wide range of AOI (45-85°) (Figure 4.4.1). In the  $\Psi$  ellipsometric parameter map, the dispersion branch starting at 550 nm corresponds to the Tamm plasmon polariton, meanwhile the lower periodic branches attributed to the cavity mode generated in the 1D PC between the two gold mirrors (Figure 4.4.1 c, d). The rather wide spectral resonance of Tamm plasmon polaritons was at the 450 nm, meanwhile the narrow periodic dips of cavity modes manifested themselves at the 580 nm, 620 nm, 680 nm and 800 nm, respectively. To prove the origin of the following optical features in the spectra of ellipsometric parameters the numerical simulation of the multilayered structure was conducted. Foremost, the dispersion relation of the 1D PC and thin gold layer were modelled (Figure 4.4.1 a). The dispersion map of ellipsometric parameter  $\Psi(\lambda, \theta)$  shows the branch of the Tamm plasmon polariton at the 550 nm and very weak oscillations of cavity modes marked with dashed lines. It is clearly seen that such multilayered structure generated optical states of Tamm plasmons which arises at the interface between 1D PC and thin gold layer. In order to analyze the contribution of bottom gold layer to the whole optical response of modified mQCM-D sensor chip, the dispersion relation of ellipsometric parameter  $\Psi(\lambda, \theta)$  for the substrate/200 nm Au/1D PC were simulated (Figure 4.4.1 b). As can be seen the noticeable enhancement of Bragg oscillations appears due to the bottom gold layer, meanwhile the absence of the thin gold layer on the top eliminates the Tamm



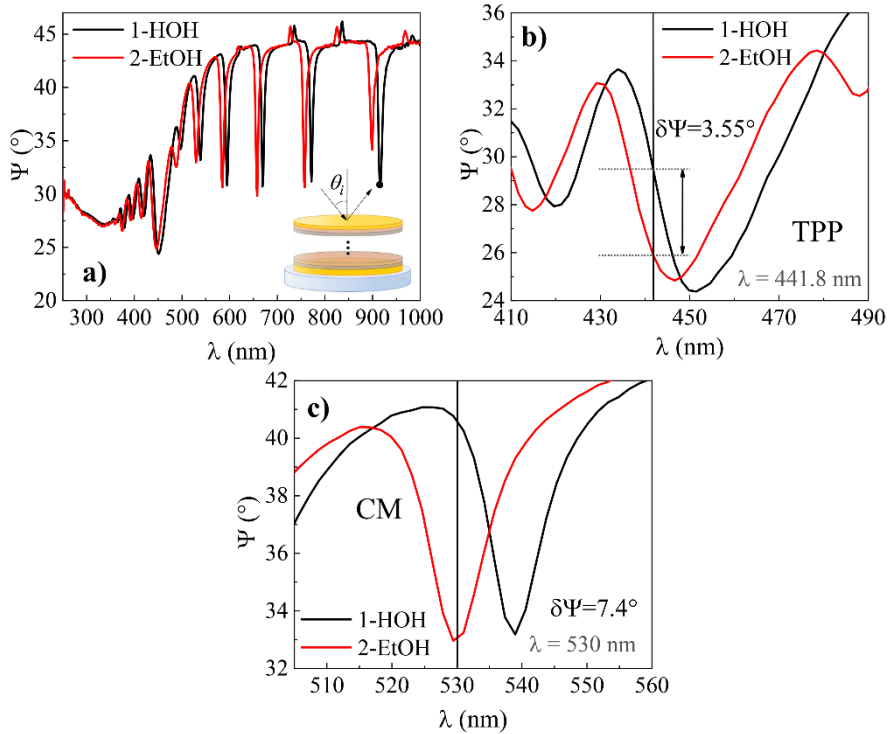


**Figure 4.4.3.** (a) Ellipsometric parameter  $\Psi$  dependence on wavelength  $\lambda$  for 1- mQCM-D in water-filled cell, 2- QCM-D/TPP in ethanol-filled cell, and zoomed view of (a) for TPP (b) and CM (c) components.

plasmon polaritons excitation. The yellow and black branches correspond to the p- and s-polarizations, respectively. Finally, the numerical simulation was conducted with the multilayered structure (Figure 4.4.1 d) which was used for experimental measurements with both gold layers (Figure 4.4.1 c). The map of dispersion relation follows the measured experimental dispersion relation and both optical effect of Tamm plasmon polariton and Bragg modes which were simulated in the Figures 4.4.1 a and b were clearly recognized in the measured dispersion map of Figure 4.4.1 c.

In order to compare the optical signal sensitivity of standard QCM-D sensor chip covered by 200 nm gold (QCM-D) and modified QCM-D sensor chip supporting Tamm plasmon polariton (TPP) and cavity modes, both were tested varying the refractive index of ambient by changing the deionized water to the ethanol in the SE-QCM-D chamber for measurements in liquids. This chamber was filled with high purity deionized water and spectra of ellipsometric parameters  $\Psi(\lambda)$  and  $\Delta(\lambda)$  were measured for both samples, standard QCM-D sensor chip and modified QCM-D/TPP+CM at the

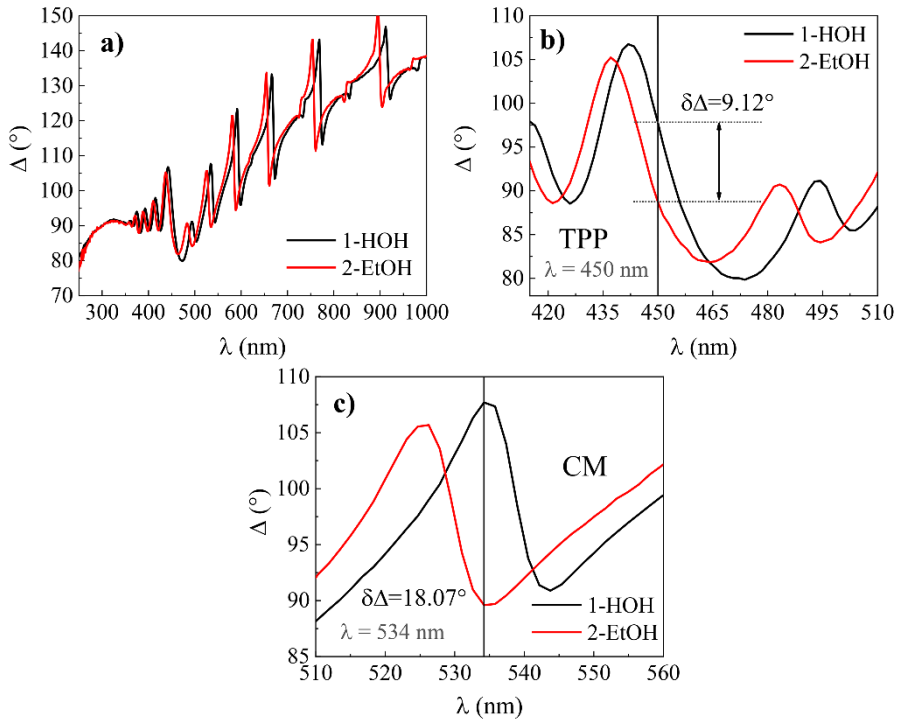


**Figure 4.4.4.** (a) Ellipsometric parameter  $\Delta$  dependence on wavelength  $\lambda$  for 1- QCM-D/TPP in water filled cell, 2- QCM-D/TPP in ethanol filled cell, and zoomed view of (a) for TPP (b) and CM (c) components.

AOI=65°. Firstly, the chamber was filled with high purity water which acted as a bulk media having refractive index  $n=1.333$  at  $\lambda=600$  nm. After that, high purity deionized water was changed to ethanol bulk media which refractive index was  $n=1.361$  at  $\lambda=600$  nm.

Spectroscopic ellipsometry measurements have shown that for standard QCM-D sensor chip the changes of the ellipsometric parameters  $\Psi(\lambda)$  and  $\Delta(\lambda)$  due to variation of refractive index of ambient liquids was miniscule. The differences registered at  $\lambda=455$  nm wavelength, was equal for  $\delta\Psi=0.15$  and  $\delta\Delta=0.79$ . No clear differences for the ellipsometric parameter  $\Psi$  values were observed between curves 1 and 2 in Figure 4.4.2 a. Close up view of Figure 4.4.2 a is presented in Figure 4.4.2 b. For the ellipsometric parameter  $\Delta$  the difference between high purity water and ethanol (Fig. 4.4.2 a) was registered 84.15° and 83.36° at  $\lambda=480$  nm wavelength for high purity water and ethanol, respectively (Fig. 4.4.2 b).

Further, the same spectroscopic ellipsometry measurements were conducted for modified QCM-D/TPP+CM sensor chip. The optical response of ellipsometric parameters  $\Psi(\lambda)$  and  $\Delta(\lambda)$  have shown that the dip of Tamm plasmon polariton observed at 451 nm for  $\Psi(\lambda)$  in the water and blue shifted to the 446 nm in the ethanol (Figure 4.4.3 a and b). At 441.8 nm  $\Psi$  obtained for water was  $29.47^\circ$  and for ethanol  $25.92^\circ$ , respectively. The calculated difference values at 441.8 nm were  $\delta\Psi=25.92^\circ-25.47^\circ=3.55^\circ$ . For ellipsometric parameter  $\Delta$  the Tamm plasmon polariton was observed at 465 nm and 475 nm in water and ethanol, respectively (Fig. 4.4.4 a and b). The difference in ellipsometric parameter  $\delta\Delta=98.01^\circ-88.89^\circ$  at the  $\lambda=450$  nm was  $9.12^\circ$ .

As the modified mQCM-D structure also supports cavity modes together with TPP, it makes it possible to employ these modes for sensing of refractive index changes. In the spectra of ellipsometric parameters, cavity modes manifested themselves as the narrow dips in the  $\Psi(\lambda)$  and abrupt changes of  $\Delta(\lambda)$  in the vicinity of resonance Fig. 4.4.3 c and Fig. 4.4.4 c, respectively.

The difference of ellipsometric parameter  $\Psi$  values at  $\lambda=530$  nm between water and ethanol filled SE-QCM-D chamber was estimated to be  $\delta\Psi=7.4^\circ$ . The value of ellipsometric parameter  $\Delta$  for cavity mode in high purity water at  $\lambda=534$  nm was  $107.67^\circ$  and in ethanol was  $89.6^\circ$ . The difference was  $\delta\Delta=18.07^\circ$ .

The difference of refractive indexes between two bulk medias was  $n_{(\text{Eth})}-n_{(\text{H}_2\text{O})}=1.361-1.333=0.028$ . After that, sensitivity to refractive index unit (RIU) of ellipsometric parameters for standard QCM-D sample, mQCM-D/TPP and mQCM-D/CM samples were evaluated. The data of sensitivity are presented in Table 4.

**Table 4.** Sensitivity and relative sensitivity of ellipsometric parameters changes to refractive index unit (RIU).

Sensitivity	
$\Psi = 0.15/0.028 = 5.4 \text{ RIU}^{-1}$	$\Delta = 0.79/0.028 = 28.2 \text{ RIU}^{-1}$
$\Psi_{\text{TPP}} = 3.55/0.028 = 127 \text{ RIU}^{-1}$	$\Delta_{\text{TPP}} = 9.12/0.028 = 325 \text{ RIU}^{-1}$
$\Psi_{\text{CM}} = 7.4/0.028 = 264 \text{ RIU}^{-1}$	$\Delta_{\text{CM}} = 18.07/0.028 = 645 \text{ RIU}^{-1}$
Relative sensitivity	
$\Psi_{\text{TPP}}/\Psi = 23.7$	$\Delta_{\text{TPP}}/\Delta = 11.5$
$\Psi_{\text{CM}}/\Psi_{\text{TPP}} = 2.1$	$\Delta_{\text{CM}}/\Delta_{\text{TPP}} = 2$
$\Psi_{\text{CM}}/\Psi = 49.3$	$\Delta_{\text{CM}}/\Delta = 22.9$

In case of standard QCM-D sample the calculated sensitivity was  $\Psi = 5.35$  RIU<sup>-1</sup>,  $\Delta$  sensitivity was  $\Delta = 28.21$  RIU<sup>-1</sup>. For TPP component in a modified mQCM-D sample, the sensitivity of ellipsometric parameters to RIU was  $\Psi_{\text{TPP}} = 126.78$  RIU<sup>-1</sup> and  $\Delta_{\text{TPP}} = 325$  RIU<sup>-1</sup>. For cavity mode in a modified mQCM-D the sensitivity  $\Psi_{\text{CM}} = 264$  RIU<sup>-1</sup> and  $\Delta_{\text{CM}} = 645$  RIU<sup>-1</sup>. The ellipsometric parameter  $\Psi_{\text{TPP}}$  sensitivity was 23.7 times higher and  $\Psi_{\text{CM}}$  sensitivity was 49.3 times higher in comparison to the standard  $\Psi$  sensitivity to RIU. The  $\Psi_{\text{CM}}$  was 2.1 times more sensitive to bulk RIU changes than  $\Psi_{\text{TPP}}$ . Relative sensitivity of ellipsometric parameter  $\Delta$  was 11.5 higher in the case of  $\Delta_{\text{TPP}}$  and 22.9 times in the case of  $\Delta_{\text{CM}}$  than standard  $\Delta$ . The ellipsometric parameter of cavity mode  $\Delta_{\text{CM}}$  was about 2 times more sensitive than  $\Delta_{\text{TPP}}$ , similarly to the compared sensitivities of the ellipsometric parameter  $\Psi$ . In this study the main focus was on the enhanced sensitivity performance of ellipsometric parameters compared with standard SE-QCM method, however, the spectral shift of the TPP and cavity mode resonances were also registered when ambient were changed from water to ethanol and for TPP it was about 10 nm, meanwhile for cavity mode of about 9 nm shift to longer wavelength. Such a spectral shift gives sensitivity of 352 nm/RIU for TPP and 321 nm/RIU for cavity mode, respectively. The comparison of refractive index sensing of various nanophotonic structures is presented in the Table 5.

**Table 5.** Comparison of various nanophotonic structures for refractive index sensing.

Method	Materials used	Sensitivity	Ref.
Tamm plasmons	Porous Si 1D PC/Au	139 nm/RIU	[188]
Fabry-Perot cavity	Porous Si	140 nm/RIU	[189]
PC nanostructures	Free standing Si membrane	103 nm/RIU	[190]
Tamm plasmons	Au coated nanoporous alumina PC	106 nm/RIU	[161]
Hybrid Tamm and surface plasmons in strong coupling	PC(TiO <sub>2</sub> /SiO <sub>2</sub> )/Au TIRE 5 bilayers	3200 nm/RIU	[49]
<b>This study</b>			
TPP	PC(TiO <sub>2</sub> /SiO <sub>2</sub> )/Au 10 bilayers	352 nm/RIU	
CM		321 nm/RIU	

#### 4.4.3 Application for biosensing

Protein adsorption at solid surfaces plays an important role in many natural processes and thus has a huge research interest in various areas including medicine, pharmaceutical sciences, analytical sciences, biotechnology, cell biology, or biophysics [191]. To demonstrate the capability of planar plasmonic-nanophotonic structure for biosensing application, bovine serum albumin (BSA) monolayer was formed on 11-MUA modified surface of QCM-D and mQCM-D. In addition, an affinity interaction with specific antibodies anti-BSA was established. In all steps, ellipsometric parameters  $\Psi$  and  $\Delta$  vs wavelength were recorded and presented in Figure 6. It was shown before [183] that combination of electrostatic and hydrophobic interaction which is supported by 11-MUA self-assembled monolayer allow to attach more BSA protein on the surface that with other SAM's. Also, it was reported [161] that graphene oxide monolayer instead of SAM,s on the gold surface can significantly improve the SPR signal response for biosensing. To evaluate the sensitivity and perform detailed analysis, the magnified view of ellipsometric parameter  $\Psi$  (Fig. 4.4.5 a) for TPP (Fig. 4.4.5 b) and cavity

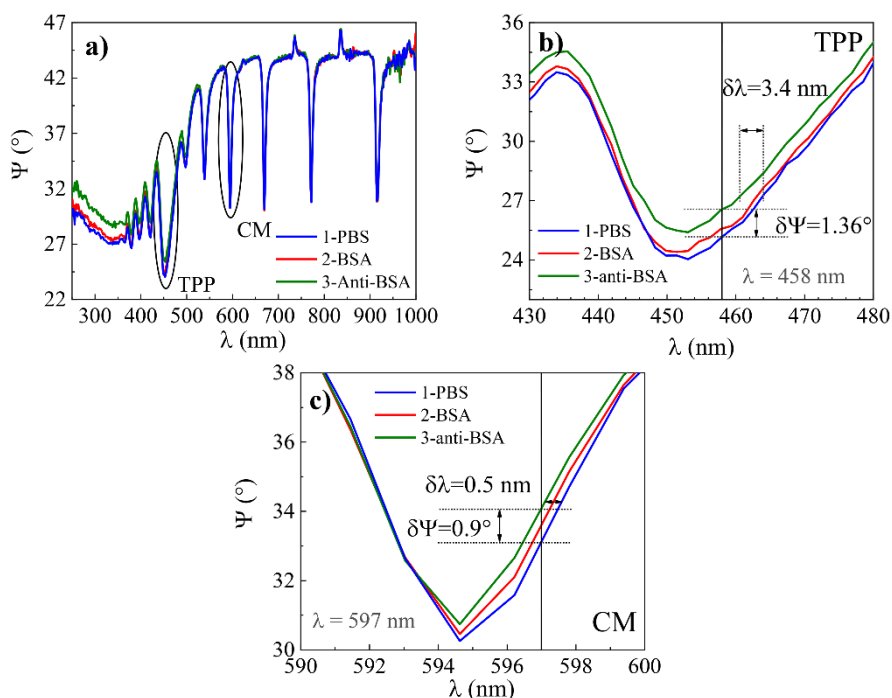


**Figure 4.4.5.** The full (a) spectra of ellipsometric parameter  $\Psi$  vs  $\lambda$  for: 1- PBS, 2- BSA, 3- anti-BSA and zoomed view of TPP (b) and CM (c).

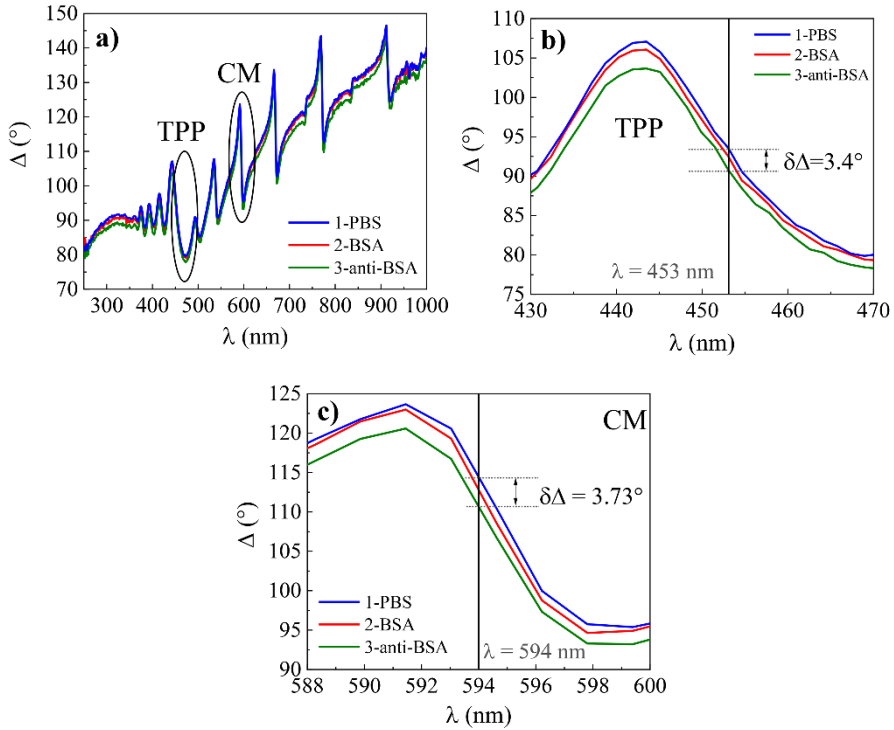


**Figure 4.4.6.** The full (a) spectra of ellipsometric parameter  $\Psi$  vs  $\lambda$  for: 1- PBS, 2- BSA, 3- anti-BSA and zoomed view of TPP (b) and CM (c).

mode (Fig. 4.4.5 c) for modified sensors chip mQCM-D are presented. The ellipsometric parameter  $\Delta$  spectra (Fig. 4.4.6 a) and zoomed in view of TPP (Fig. 4.4.6 b) and CM (Fig. 4.4.6 c). The optical response of ellipsometric parameter  $\delta\Psi$  detected for TPP mode between curves 1 and 3 was  $1.36^\circ$  (Fig. 4.4.5 b), meanwhile for CM mode the difference was  $\delta\Psi = 0.9^\circ$  (Fig. 4.4.5 c). Also, simultaneously registered ellipsometric parameter  $\Delta$  have shown the differences  $\delta\Delta$  between curves 1 and 3 for TPP of  $3.4^\circ$  (Fig. 4.4.6 b) and for cavity mode it was  $3.73^\circ$  (Fig. 4.4.6 c), respectively.

The spectroscopic ellipsometry data for modified mQCM-D sensor chip were analyzed by a multilayer model [141,171,192]. In this study, the multilayer model represented the following structure: Quartz substrate/Au (200 nm)/1D PC (TiO<sub>2</sub>/SiO<sub>2</sub> (110/60nm)/Au (40nm)/MUA-11/BSA+anti-BSA/buffer solution. Firstly, the structure with pure gold layer/buffer interface without proteins, were analyzed to evaluate the reference optical properties of the multilayer structure, such as the thickness and optical constants of each layer. At the starting point of the fitting the optical constants of the materials were used, namely BK7 [193], SiO<sub>2</sub> [194], Au [195] and TiO<sub>2</sub>

[196] were taken from the literature. The reasonably good fitting results (MSE=11.3) were obtained, then only the thicknesses of the multilayer structure were free fitting parameters while the optical constants stay fixed. Furthermore, the ellipsometric spectra of attached BSA and anti-BSA proteins on the gold surface were analyzed, additionally introducing the layer describing the attached surface mass of the studied proteins. The refractive index of the protein layer was approximated as a homogeneous layer and described using the Bruggeman effective medium approximation (EMA). The EMA considers the BSA+anti-BSA protein layer to be an isotropic physical mixture of two elements, protein and buffer solution, and homogenous on the scale of wavelength. The effective refractive index of the mixture was calculated from the volume fractions of its components, assuming that these retain their intrinsic optical properties and the thickness of the layer was obtained  $d=18$  nm.

While the thickness and effective refractive index of BSA proteins were determined from regression analysis, de Feijter's formula [177]  $\Gamma = \frac{d(n-n_{buffer})}{dn/dC} \times 100$  allow to evaluate the surface mass ( $\text{ng}/\text{cm}^2$ ), where  $dn/dC=0.18 \frac{\text{cm}^3}{\text{g}}$  [178] is the refractive index increment for the layer material, depending on the protein concentration in the buffered solution,  $d$  is the thickness (nm) and  $n$  is the refractive index of the protein layer obtained from regression analysis and  $n_{buffer}$  is the refractive index of the buffered solution. The attached surface mass for spectroscopic ellipsometry  $\Gamma_{SE} \approx 600 \text{ ng}/\text{cm}^2$  was calculated for the resonant wavelength of Tamm plasmon polariton and cavity mode excitation, meanwhile the obtained surface mass from the QCM-D was  $\Gamma_{QCM-D} \approx 1750 \text{ ng}/\text{cm}^2$ . Such a differences in attached surface mass is explained by contribution of buffer solution to the mass evaluation in QCM-D method, meanwhile from the SE evaluated the "dry mass" of the protein [183]. Such information obtained simultaneously from the coupled methods opens possibilities to study proteins conformational changes depending on the pH, surface charge and many other factors [197,198].

It should be noted that in the case of biomolecules interaction experiment the sensitivity of the ellipsometric parameters of Tamm plasmon polariton was higher for  $\Psi$  and, generally, had the same sensitivity for  $\Delta$  compared with cavity modes. The ellipsometric parameter of TPP was  $\Psi=1.36/0.9 \approx 1.5$  more sensitive to the attached surface mass than cavity mode, meanwhile, the phase difference  $\Delta=3.4/3.7 \approx 0.92$  was still slightly better for the cavity mode. However, as can be seen from Table 4 the measurements for ambient with different refractive indexes showed much higher sensitivity for the cavity

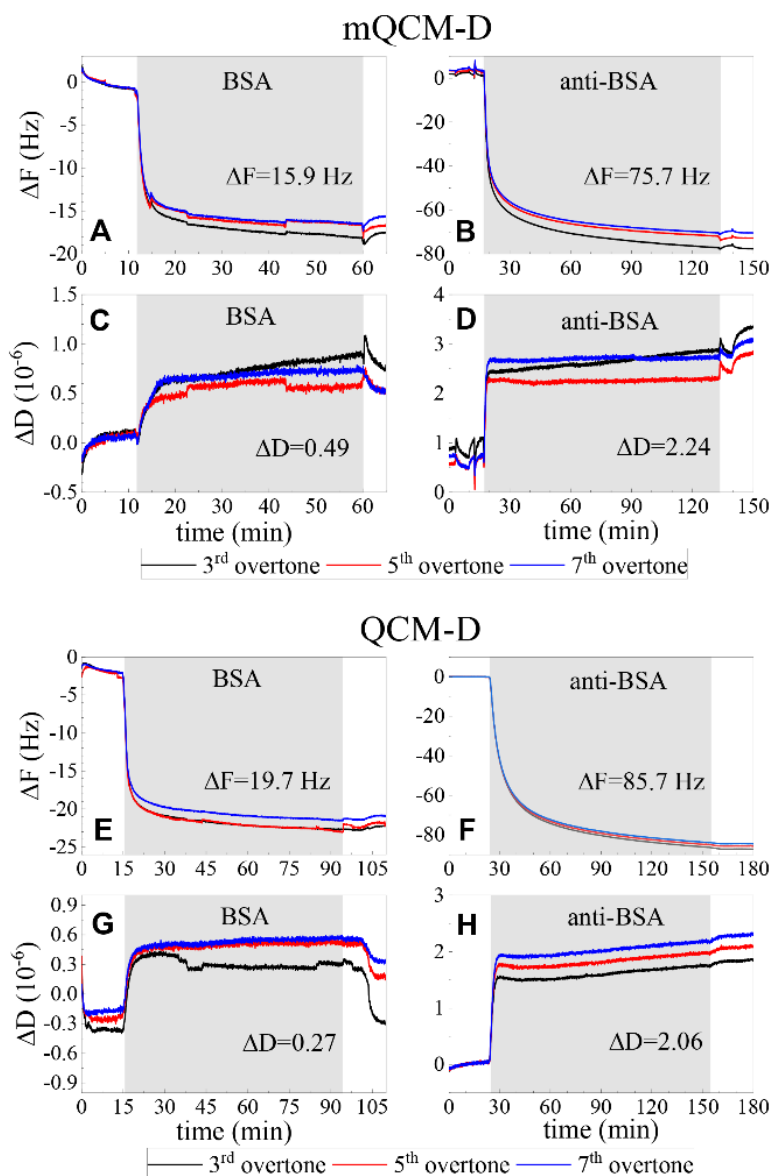


**Figure 4.4.7.** The BSA immobilization and anti-BSA affinity kinetics of modified mQCM-D (A-D) and QCM-D (E-H) sensorchips for resonance frequency shift  $\Delta F$  (A, B, E, F) and energy dissipation  $\Delta D$  (C, D, G, H) changes.

mode than for Tamm plasmon polariton. This can be explained by the different origin of Tamm plasmon polaritons and cavity modes. Tamm plasmon polariton in fact is a surface optical state which appears at the interface



between the metal film and photonic crystal, meanwhile the cavity modes are generated through the full length of the photonic crystal between the two gold mirrors. Thus, when some changes of refractive index occur on the surface of a thin gold layer (formation of protein monolayer, for instance), this process has more influence for the surface sensitive resonance – Tamm plasmon polariton, than for cavity mode. On the contrary, when the refractive index of the ambient was changed, the angle of light incidence to the gold film surface refracted through the length of the bulk ambient and transmitted to the photonic crystal at a deviate angle, which has a significant influence to the resonant wavelength of the cavity modes. This assumption supports the stronger dependence of the cavity modes on the angle of incidence which can be seen in the dispersion relation map of  $\Psi$  ellipsometric parameter (Fig. 4.4.1).

In order to clarify the contribution of deposited planar plasmonic-photonic structure on the resonant frequency of quartz crystal microbalance the standard and modified QCM-D sensor discs' frequencies were measured. The quartz crystal resonant frequency (F1) in deionized water for the standard QCM-D sensor disc was 4.952 MHz. The PC/Au modified mQCM-D sensor chip F1 frequency was equal to 4.922 MHz. The shift of QCM-D frequency in kinetics measurements showed consistency between standard QCM-D and mQCM sensors, thus the difference of 0.03 MHz in F1 does not affect the sensitivity of QCM-D method. In Fig. 4.4.7 presented covalent BSA immobilization on self-assembling monolayer 11-MUA and affinity interaction of anti-BSA with formed BSA monolayer on both samples: mQCM-D (Fig. 4.4.7 A-D) and QCM-D (Fig. 4.4.7 E-H), A-D and E-H demonstrates the  $\Delta D$  and  $\Delta F$  of the binding kinetics between proteins, respectively. As it can be seen from Fig. 4.4.7 the resonance frequency shift  $\Delta F$  and energy dissipation  $\Delta D$  were similar for both samples – mQCM-D and QCM-D. Such a performance of both modified and standard QCM sensor chips have shown similar performance.

### Summary

The planar plasmonic photonic structures made from periodic dielectric layers and thin metal film were designed for improved performance of ellipsometric parameters  $\Psi(\lambda)$  and  $\Delta(\lambda)$  in the combinatorial spectroscopic ellipsometry and quartz crystal microbalance method. The low-cost 1D plasmonic photonic structures supporting Tamm plasmon polaritons and cavity modes were employed for the optical signal enhancement by modifying the commercially available QCM-D sensor chip.

This study has shown that for refractive index sensing of ambient the planar plasmonic photonic nanostructures exhibits higher sensitivity than conventional quartz microbalance sensor chip. Namely, the cavity modes and Tamm plasmon polariton was about 49 and 24 times more sensitive than the standard QCM-D sensor chip, respectively. For the ambient refractive index sensing the cavity modes have shown the twice better sensitivity for ellipsometric parameters  $\Psi(\lambda)$  and  $\Delta(\lambda)$  the Tamm plasmon polariton mode. However, the TPP still showed about 24 and 12 times higher sensitivity for ellipsometric parameters  $\Psi$  and  $\Delta$ , respectively, than the standard QCM-D sensor chip. Meanwhile, for the optical biosensing signal readout, the sensitivity of Tamm plasmon polaritons and cavity modes were comparable and higher than with standard QCM-D sensor chip. This fact can be explained by the different origin of Tamm plasmon polaritons and cavity mode phenomena's, the first of which is a surface optical state, meanwhile the second one, generated through the full length of the cavity. This difference in optical features gives additional advances and can determine whether the surface or bulk process is dominant. The dispersion relation feature of Tamm plasmon polaritons namely, the direct excitation without additional coupler, gives the possibility to enhance the optical signal on the sensing surface despite the fact that Tamm plasmons are excited at the inner interface of the gold layer. The generation of Tamm plasmon polaritons at the inner interface is not optimal for the sensing applications, however, in this optical configuration TPP gives about 24 times improved sensitivity in  $\Psi$  ellipsometric parameter. To the best of our knowledge this is the first study and application of the Tamm plasmon polaritons and cavity mode in the combinatorial SE-QCM-D method for the enhanced readout of ellipsometric parameters.

## 4.5 Gold microbump arrays for generation of hybrid lattice plasmon polaritons

### 4.5.1 Introduction

Plasmonics has become a topic of the widely studied field of light-matter interaction and has led to numerous fundamental investigations and applications to novel optical devices based on surface plasmon polaritons (SPPs) [199]. As the SPP waves cannot be excited by light in air, the efficient coupling between free-space light and SPPs on a flat metal surface remains challenging, especially if a prism coupler is technically challenging in development of practical applications. The grating coupler approach is attractive for device integration since the grating can be fabricated directly on the metal film supporting the SPPs [200]. The current technological progress enables the creation of complex plasmonic systems supporting multiple plasmon modes, which can be analyzed as the interaction of elementary plasmons supported by nanostructures. The most popular models of complex plasmonic systems are metallic nanodimers [201], metallic nanoshells [202] and metallic nanoparticles near metal films [203]. Such structures exhibit the plasmon hybridization effect where different plasmonic excitations can interact with each other. The theoretical studies based on the coupled dipole approximation (CDA) model have shown that ultra-narrow plasmonic resonances appear in the periodic arrays of metal nanoparticles where the period is comparable with the incident light wavelength. The ordered array of metal nanoparticles acts as a diffractive grating for incident light which diffraction effect depends on the size, shape, and period of the array. If one of the scattered waves propagates in the plane of the array it can couple with localized plasmon resonance of these nanoparticles. When nanoparticles are arranged by an appropriate period, the scattered light field is in phase with local plasmon resonance to the nearby nanoparticle, thus enhancing the plasmonic excitation in the neighbor particle. Since, at resonance all nanoparticles in array oscillate in phase and the diffractively scattered photons from nanoparticles can excite the LSPs in adjacent nanoparticles instead of decaying in free space, as a result the lattice resonances suppress radiative losses [204]. This leads to a significant narrowing of the plasmonic resonance, due to compensation of the damping of localized plasmon resonance of the individual particles by the scattered field of light [48]. This phenomenon overcomes a fundamental problem of the plasmonic resonances having usually a rather wide spectral width compared with the resonances on the dielectric nanostructures. However, the localized surface plasmons are weakly

tunable due to their limited dispersion [99], while, surface plasmonic modes can be tunable in a wide spectral range. By combining thin gold film with a periodic array of gold microbumps, one can create a hybrid lattice plasmon polariton mode (HLPP) that opens the possibility to merge the spectral tuning of SPP and reduced propagation losses of the LSP mode, due to Bragg reflections [47,105]. These properties provide potentially richer implementations in light manipulation and could be applied for nanolasing structures and plasmonic bio-sensors, where dispersion features allow to excite the hybrid plasmonic modes directly through the liquid ambient as well as narrowing of the resonance due to electric field localization on the gold microbumps that increases the sensitivity of such type of optical sensors.

Despite the technological progress in the fabrication of complex plasmonic systems, the creation of structures with the extremely small dimensions of the periodic surface irregularities remains still complicated, time-consuming, and expensive. The most popular fabrication method of such structures is lithography-based techniques, which are limited in the production of large areas of the arrays. The size of the periodic arrays supported plasmonic lattice surface resonance is significant as the detection of the optical response requires the illumination of a sufficient number of periodic elements with spatially coherent light over a large surface area.

Here, the fabrication of large-scale gold microbumps arrays in a gold film using a cost-effective direct laser writing technique is presented. The fabricated arrays support hybrid lattice plasmon polariton (HLPP) modes with reduced losses and tunable dispersion properties in the VIS-NIR range, in the same range as structures fabricated by lithography-based techniques [205]. The reduced losses manifested themselves as a narrow resonance width of the HLPP compared with the spectral width of traditional surface plasmon resonance. This work shows significant technological progress in the formation of large-scale metallic gratings via laser-based technique as the previous works based on this technique demonstrated the surface plasmon resonances (SPR) of gratings in a spectral range at 2–6  $\mu\text{m}$  [206]. The demonstrated DLW production method paves new opportunities for hybrid lattice plasmon polariton (HLPP)-based applications in biotechnology, photonics, plasmonics, etc.

The results presented in the following Chapter were originally published in:

E. Stankevičius, K. Vilkevičius, M. Gedvilas, E. Bužavaitė-Vertelienė, A. Selskis and Z. Balevičius. “Direct Laser Writing for the Formation of Large-Scale Gold Microbumps Arrays Generating Hybrid Lattice Plasmon

#### 4.5.2 Hybrid lattice plasmon polaritons dispersion relations

Surface plasmons polaritons propagating on a planar metal surface are described by the dispersion relation, which is the solution of Maxwell's equations by applying the infinite conditions to the metal/dielectric interface. The dispersion relation of surface plasmons polaritons at a dielectric-metal interface is described by Eq. 2.13.

The dispersion relation of surface plasmons on a planar metal surface is plotted schematically in Fig. 4.5.1 (red lines). The relation between the wavevector of light in free space ( $k_i$ ) and angular frequency  $\omega$  is linear (dashed grey line in Fig. 4.5.1). As presented in Fig. 4.5.1, the wavevector of light in free space  $k_i$  is always smaller than the wavevector of the surface plasmons  $k_{SPP}$ . Therefore, SPP cannot be excited by direct illumination of the metal surface with light (due to the non-radiative nature of SPP). Excitation of SPP occurs only when the photon and SPP wavevectors match. The photon and SPP wavevectors can be matched using photon tunneling in the total internal

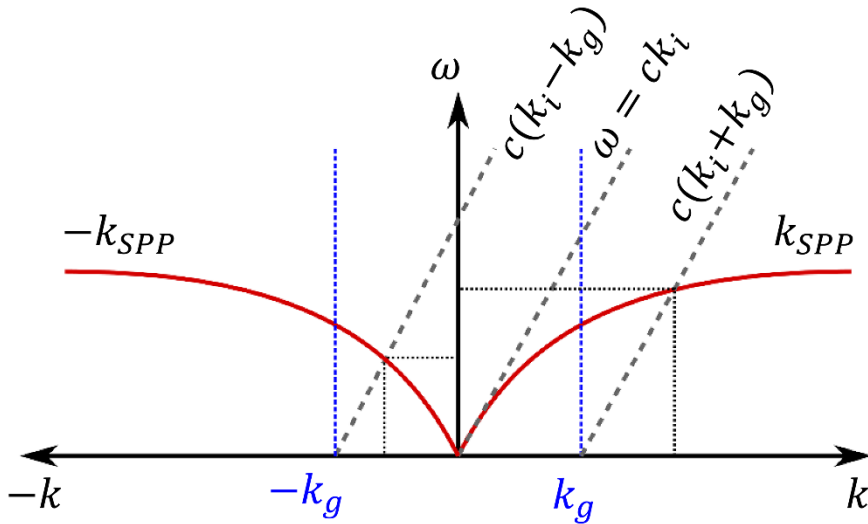


**Figure 4.5.1.** Dispersion relations of light and surface plasmons polariton. The  $x$ -component of the incident light ( $k_i$ ) is shown by the dashed grey line. The diffraction of the incident light by the grating results in the lines  $c(k_i + k_g)$  and  $c(k_i - k_g)$ . The intersection of the diffracted light lines with the plasmon dispersion lines  $k_{SPP}$  and  $-k_{SPP}$  indicate the frequencies of the excited plasmons polaritons.

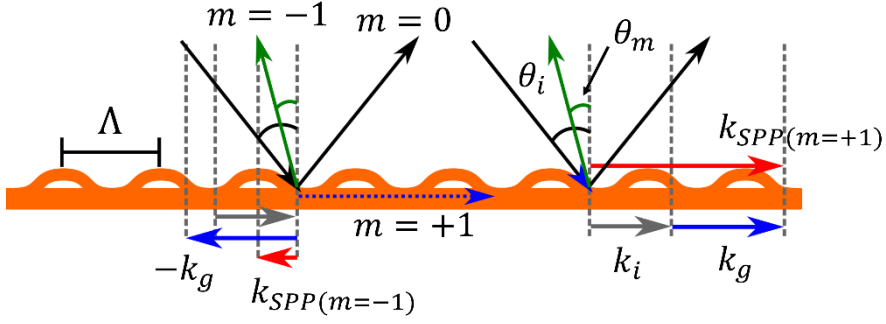


**Figure 4.5.2.** The relationship between the tangential component of the incident light wavevector  $k_i$  (black), grating vector  $k_g$  (blue), and the wavevector of surface plasmons polaritons  $k_{SPP}$  (red).  $k_{SPP(m=-1)}$  and  $k_{SPP(m=+1)}$  are wavevectors of the surface plasmons polaritons coupled with -1 and +1 diffraction orders, respectively.  $\theta_i$  is the angle of incident light;  $\theta_m$  is the angle of diffracted light;  $m$  is the diffraction order;  $\Lambda$  is the period of the gold bumps array.

reflection geometry (Kretschmann and Otto configurations) or diffraction effects [92]. One attractive method to excite surface plasmons is to use a diffraction grating on the metal surface [207,208]. A grating has a fixed wavevector, due to the periodicity, and as a result it changes the momentum of the incident wave along the surface by adding an integer of the grating vector to the incident wave surface component. The wavevector of the grating vector is given by  $k_g = 2\pi/\Lambda$ , where  $\Lambda$  is the period of the grating.

When light with wavevector  $k_i$  is incident on the grating at an angle  $\theta_i$  with the surface normal, the incident light is diffracted into multiple beams according to the following diffraction relation [207]:

$$k_i(\sin \theta_m - \sin \theta_i) = mk_g, \quad (4.10)$$

where  $\theta_m$  is diffraction angle and  $m$  is the diffraction order.

The diffracted beams have a wavevector component tangential to the surface given by  $k_i \sin(\theta_m)$ . The excitation of SPPs on a grating is achieved when the wavevector of the surface plasmons and the tangential component of the wavevector of the diffracted beam match the momentum conservation condition:

$$\pm k_{SPP} = k_i \sin \theta_m = k_i \sin \theta_i + mk_g. \quad (4.11)$$

In Eq. 4.11  $k_i \sin(\theta_i)$  is the wavevector component tangential to the surface of the incident beam. The sign  $\pm$  before  $k_{SPP}$  shows that surface plasmon polaritons can propagate either in the positive or negative  $x$ -direction (Fig. 4.5.2). The grating coupling of surface plasmons is schematically explained in Fig. 4.5.1. The surface plasmon excitation condition is satisfied when the incident light dispersion curve (the red lines in Fig. 4.5.1) crosses the lines  $c(k_i + k_g)$  and  $c(k_i - k_g)$  (the dashed grey lines in Fig. 4.5.1). The intersection of the diffracted light lines with the plasmon dispersion lines  $k_{SPP}$  and  $-k_{SPP}$  indicate the frequencies of the excited plasmons. The graph shows that the surface plasmons excitation can occur when the angle of incidence is between  $0^\circ$  and  $90^\circ$  at two different frequencies: one ( $\omega(-1)$ ) corresponding to the  $-k_{SPP}$  intersection with  $c(k_i - k_g)$  and another ( $\omega(+1)$ ) where  $k_{SPP}$  crosses  $c(k_i + k_g)$ . If the incident light impinges normal to the surface, then the plasmons are excited at a single frequency. The positive and negative vectorial

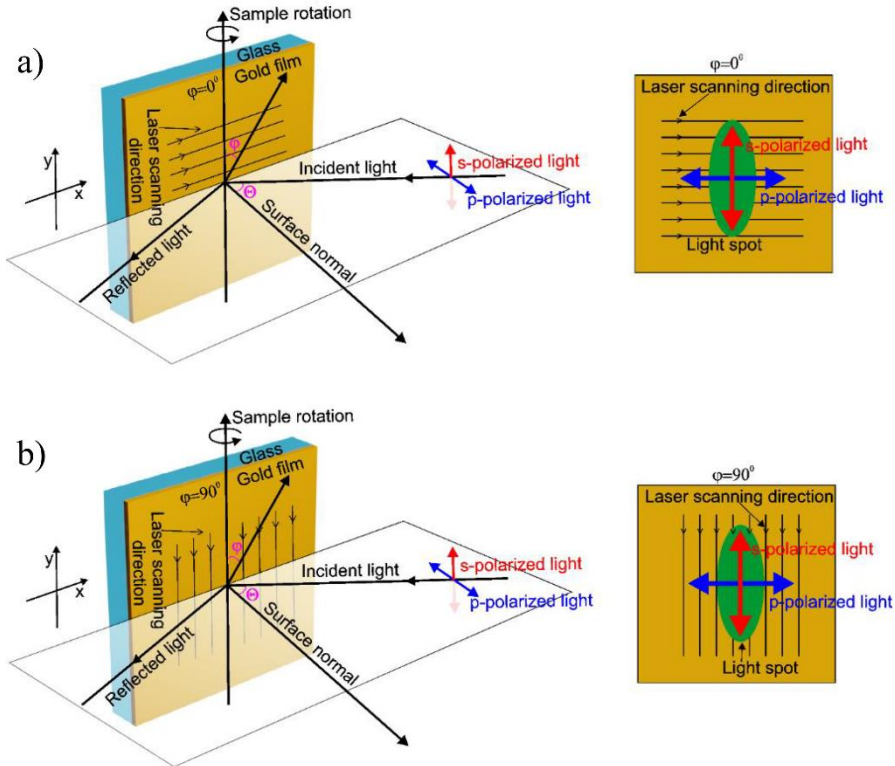


**Figure 4.5.3.** 3D (left) and 2D (right) views of the sample orientation in the reflectance measurement, when  $\varphi=0^\circ$  (a), and  $\varphi=90^\circ$  (b).  $\theta$  is the angle of light incidence and  $\varphi$  is the azimuthal angle.

solutions correspond to the rightwards and leftwards propagating surface plasmons having different frequencies (Fig. 4.5.2).

### 4.5.3 Investigation of plasmonic properties

The reflectance spectra of the fabricated gold bump array were measured using a spectrophotometer (Photon RT, Essentoptics). The measurements were performed for *s*- and *p*-polarized light within the wavelength range from 0.4 to 1.5  $\mu\text{m}$  and different angles of incidence  $\theta = 8^\circ, 15^\circ, 30^\circ, 45^\circ,$  and  $60^\circ$ , when light beam spot size was  $2 \times 5$  mm. The azimuthal angle  $\varphi$  of the sample was selected as  $0^\circ$ , when the plane of light incidence is parallel to the laser scanning direction used in microbumps formation process (Fig. 4.5.3 a), and  $90^\circ$ , when the plane of light incidence is perpendicular to the laser scanning

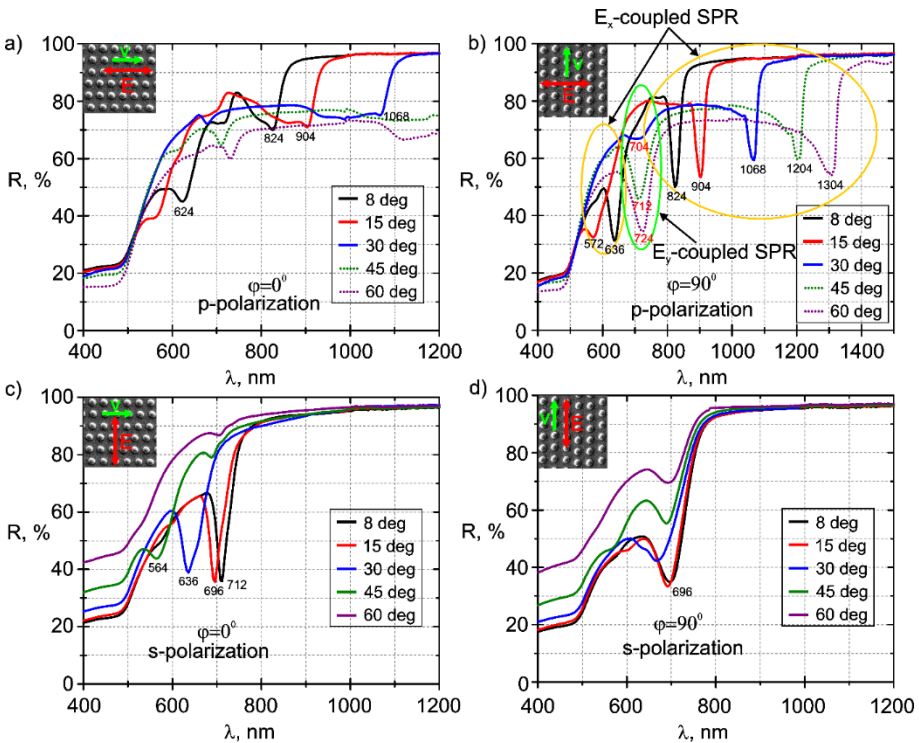


**Figure 4.5.4.** Reflectance spectra of microbumps array with period 700 nm in 50 nm thick gold film for a,b) *p*-polarized and c,d) *s*-polarized light when  $\varphi=0^\circ$  (a, c) and  $\varphi=90^\circ$  (b, d). Insets on the graphs show the laser scanning direction during the microbumps formation (green arrows) and the oscillation direction of the electric field (red arrows). Spectra were measured for the different angles of light incidence:  $8^\circ$  (black curves);  $15^\circ$  (red curves);  $30^\circ$  (blue curves),  $45^\circ$  (green curves), and  $60^\circ$  (purple curves).



direction (Fig. 4.5.3). The sample was rotated along (when the azimuthal angle  $\varphi=0^\circ$ ) and perpendicular ( $\varphi=90^\circ$ ) to the laser scanning direction during the measurement of the reflectance spectra.

The measured reflectance spectra for *s*- and *p*-polarized light when the azimuthal angle  $\varphi=0^\circ$  and  $\varphi=90^\circ$ , gold film thickness 50 nm and bumps period 700 nm are given in Fig. 4.5.4. The results show that the coupling of the microbumps array depends on the laser scanning direction during their fabrication. When *p*-polarized light is parallel to the laser scanning direction, the hybrid lattice plasmon resonances (HLPR) are wide (Fig. 4.5.4 a). This can be influenced by the defects and dislocation of arrays. When *p*-polarized light is perpendicular to the laser scanning direction (Fig. 4.5.4 b), the HLPR becomes  $\sim 30$  nm width at half of the maximum (FWHM). The narrowing of the resonance width is fated by the plasmonic surface lattice resonances phenomenon (diffractively coupled surface plasmon resonances with Bragg reflections parallel to the interface), which leads not only to a remarkable narrowing of the resonance width as well as to related phenomenon such as a dramatic enhancement of the electric field near the nanostructures [103]. In this case, the HLPR was observed at two different wavelengths for the  $8^\circ$  and  $15^\circ$  angles of incidence. The spectral separation between two plasmonic dips increased with an increasing incident angle, as shown in Fig. 4.5.4 b (yellow circles). The second peak of HLPR at the higher angles of incidence ( $30^\circ$ ,  $45^\circ$ , and  $60^\circ$ ) disappears due to the absorption of gold in the spectral region below 500 nm. Additionally, the same sample was tested using the variable angle

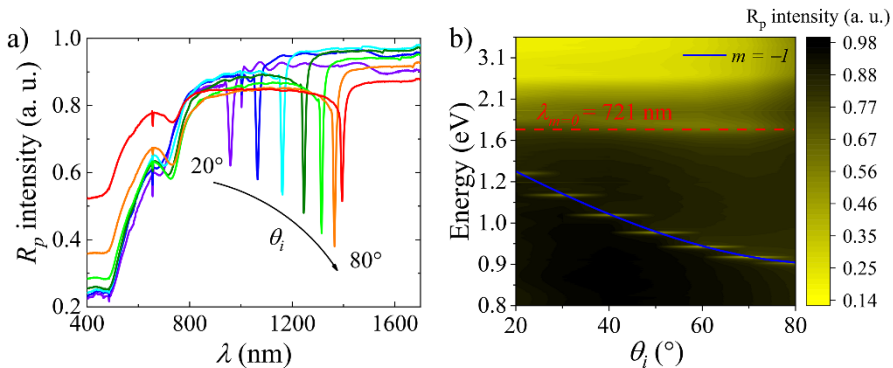


**Figure 4.5.5.** Reflectance spectra measured using polarization-sensitive variable angle spectroscopic ellipsometry method (VASE) in  $20^\circ$ - $80^\circ$  range of angle of incidence (AOI) of microbumps array with period 700 nm in 50 nm thick gold film for *p*-polarized light when  $\varphi=90^\circ$ ; b) The map of the measured dispersion relation of the HLPs corresponds to the *p*-polarization.

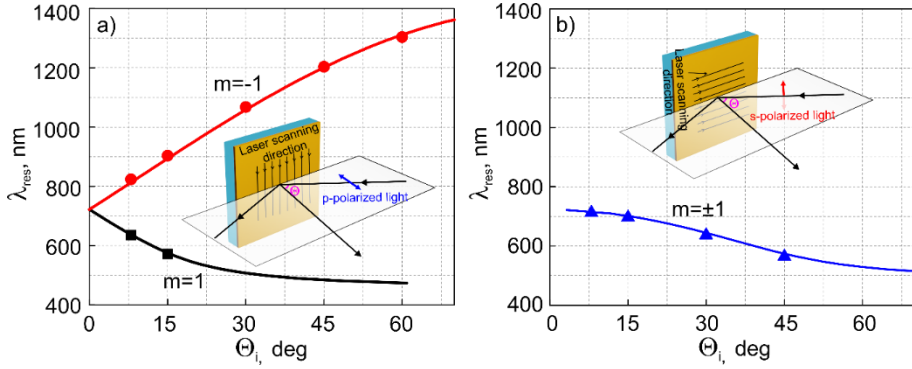


**Figure 4.5.6.** The theoretically calculated (solid lines) and the experimentally measured data points (squares, circles, and triangles) of HLPP resonant wavelength dependence on the angle of incidence, when the incident light is  $p$ -polarized and  $\varphi=90^\circ$  (a), and when the light is  $s$ -polarized and  $\varphi=0^\circ$  (b).

spectroscopic ellipsometry method (VASE) (J. A. Woollam RC2 ellipsometer) in the spectral range of 210-1700 nm, when the angle of incidence (AOI) was selected in the range of  $20^\circ$ - $80^\circ$ . The results are depicted in Fig. 4.5.5. In this case, the measurements were performed using a light spot size  $250 \times 500 \mu\text{m}$ . It is about 10 times smaller compared to the beam spot size ( $2 \times 5 \text{ mm}$ ) used in the spectrophotometer measurements shown in Fig. 4.5.4. The plasmonic dips in the VASE method are narrower compared to the spectrophotometer method and can be lower than 10 nm width at half of the maximum (Fig. 4.5.5 a). The narrowing of the plasmonic dip is related to the used light spot size and suitable numerical aperture in the measurements [48], the larger illuminated area includes more defects of the array which might result in a larger FWHM. In Fig. 4.5.5 b, it is given the map of the measured dispersion relation of the HLPs, which is determined by the interaction of in-plane Bragg reflections with propagated surface plasmon resonance. Compared with the local plasmons (LSPs), the hybrid lattice resonance has dispersive nature because of the surface plasmon polaritons component.

As the narrow HLPR of the fabricated microbumps array has been demonstrated only in one direction, the theoretical estimations were performed based on the 1D grating theory. The resonant wavelength of surface plasmons when 1D gold grating is in the air and the plane of light incidence is perpendicular to the 1D grating lines ( $p$ -polarization) is expressed [207]:

$$\lambda_{res} = -\frac{\Lambda}{m} \left( \sin \theta_i \mp \sqrt{\frac{\epsilon_{Au}}{1 + \epsilon_{Au}}} \right), \quad (4.12)$$

where  $\Lambda$  is the period of the grating;  $m$  is diffraction order;  $\theta_i$  is the incident angle of light;  $\varepsilon_{Au}$  is the dielectric constant of gold. This case matches the sample rotated orthogonally to the grating lines,  $\varphi=90^\circ$ , Fig. 4.5.3 b.

Dispersion relation using Eq. 4.12 was performed. The real and imaginary parts of refractive indexes of gold at different wavelengths were taken from reference [209]. The theoretically resonant wavelengths  $\lambda_{res}$  depending on the incident angle  $\theta_i$  for  $p$ -polarization are represented by red and black solid lines in Fig. 4.5.6 a. The experimentally measured hybrid lattice plasmon resonances represented by data points in Fig. 4.5.6 a perfectly fit these curves (red circles for  $m=-1$  and black squares for  $m=1$ ).

Besides the HLPR at two different wavelengths, the third resonance was observed for large incident angles at wavelength approximately equal to the period of the grating (green circle in Fig. 4.5.4 b). These peaks appear when the plane of the light incidence is inaccurately perpendicular to the laser scanning direction during the measurements of the spectra. In this case, the electric field vector can be divided into two orthogonal components ( $\mathbf{E}_x$  and  $\mathbf{E}_y$ ), therefore the HLPR is coupled with  $\mathbf{E}_x$  and  $\mathbf{E}_y$  components.  $\mathbf{E}_x$  is perpendicular to the laser scanning direction and  $\mathbf{E}_y$  coincides with the laser scanning direction (Fig. 4.5.7 a). The influence of  $\mathbf{E}_y$  components grows by increasing the incident angle (Fig. 4.5.4 b). The peaks coupled with  $\mathbf{E}_y$  are wider (compared to the HLPR coupled with  $\mathbf{E}_x$ ) and occur only when the incident angle is equal to or larger than  $30^\circ$ . When the sample alignment is perfect with the grating lines, only one component of the electric field ( $\mathbf{E}_x$  or  $\mathbf{E}_y$ ) couples the HLPR. Hence,  $\mathbf{E}_x$  matches  $p$ -polarized light (Fig. 4.5.7 b) and  $\mathbf{E}_y$  -  $s$ -polarized light (Fig.4.5.7 c).

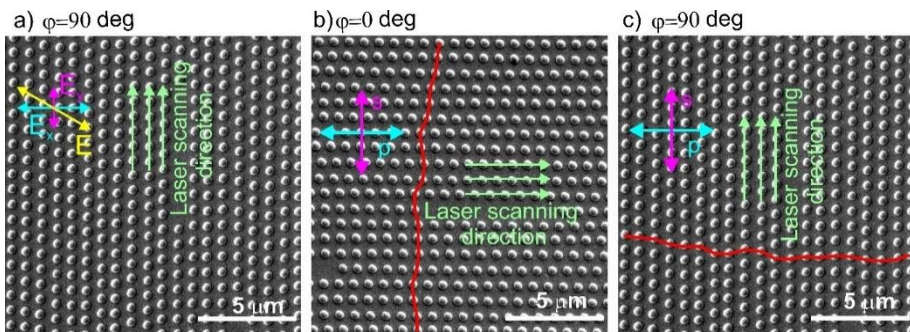


**Figure 4.5.7.** a) Electric field vector (yellow arrow) when the alignment of the vector does not fit the array in laser scanning direction; b) Electric field vector  $p$ -polarization component that fits the laser scanning direction; c) Electric field vector  $s$ -polarization component that fits the laser scanning direction.

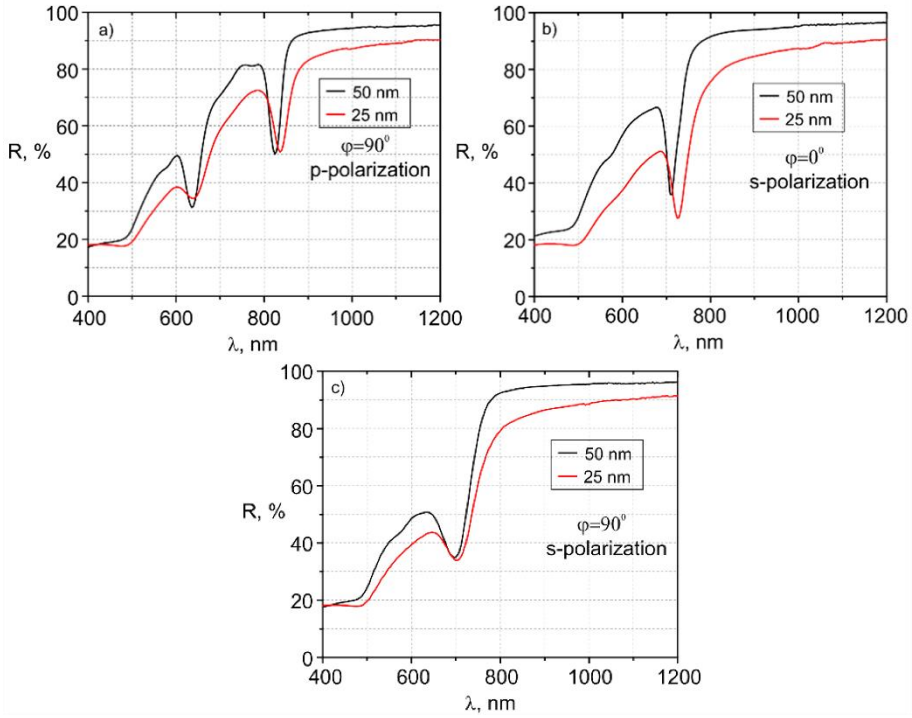


**Figure 4.5.8.** Reflectance spectra of microbumps array with 700 nm period in 50 nm (black curves) and 25 nm (red curves) Au film for *p*-polarized light when  $\varphi=90^\circ$  (a), *s*-polarized light when  $\varphi=0^\circ$  (b) and  $\varphi=90^\circ$  (c) at  $8^\circ$  AOI.

The resonant wavelength of hybrid lattice plasmons resonance when the 1D gold grating is in the air and the plane of light incidence is parallel to the 1D grating lines is expressed (*s*-polarization, the sample is rotated along the grating lines,  $\varphi=0^\circ$ , Fig. 4.5.3 a) [207]:

$$\lambda_{res} = \pm \frac{\Lambda}{m} \sqrt{\frac{\epsilon_{Au}}{1 + \epsilon_{Au}} - \sin^2 \theta_i}, \quad (4.13)$$

Theoretical estimation using Eq. 4.13 is shown in Fig. 4.5.6 b. When the incident light is *s*-polarized and the sample is rotated along the grating lines (the laser scanning direction), only a single resonance peak is observed. The resonance peak shifts toward shorter wavelengths by increasing the incident angle  $\theta_i$  (Fig. 4.5.4 c). The measured resonance peaks (triangles in Fig. 4.5.6 b) are in good agreement with the theoretical calculations.

When *s*-polarized light is parallel to the laser scanning direction ( $\varphi=90^\circ$ ), the hybrid lattice plasmons resonances (HLPR) occur at the wavelength equal

to the grating period for all angles of light incidence (Fig. 4.5.4 d). Since the sample is rotated around the axis perpendicular to the laser scanning direction (Fig. 4.5.3 a), the HLPR is independent of the incidence angle and the electric field vector oscillates along the grating lines consisting of gold microbumps having a period of 700 nm. In this case, the incident light satisfies the same conditions as the incident light impinges normally to the surface ( $\theta_i=0$ ) where the HLPR occurs at a wavelength equal to the grating constant [210]. The period of the microbumps array determines the place of the HLPR in the reflectance spectra. The deviation of HLPR by changing the light incident angle in Fig. 4.5.4 d appears due to the imperfect alignment of the sample with the grating lines.

The influence of gold film thickness on the HLPR was investigated by the fabrication of gold microbumps grating in different gold films having 50 nm and 25 nm thickness. The measured reflectance spectra for different samples are shown in Fig. 4.5.8. Analysis indicates that the film thickness slightly affects the HLPR of the fabricated structure, and the thinner film has lower

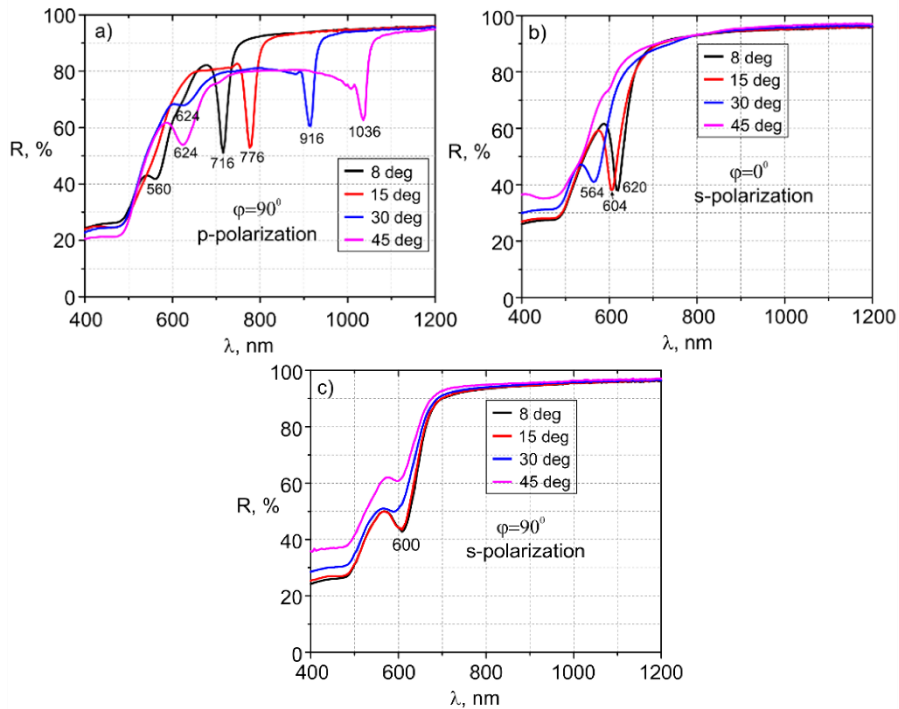


**Figure 4.5.9.** Reflectance spectra of microbumps array with 600 nm period in 50 nm gold film for a) *p*-polarized and b, c) *s*-polarized light for  $\varphi=90^\circ$  (a, c) and  $\varphi=0^\circ$  (b) with different AOI: 8° (black curves); 15° (red curves); 30° (blue curves) and 45° (pink curves).

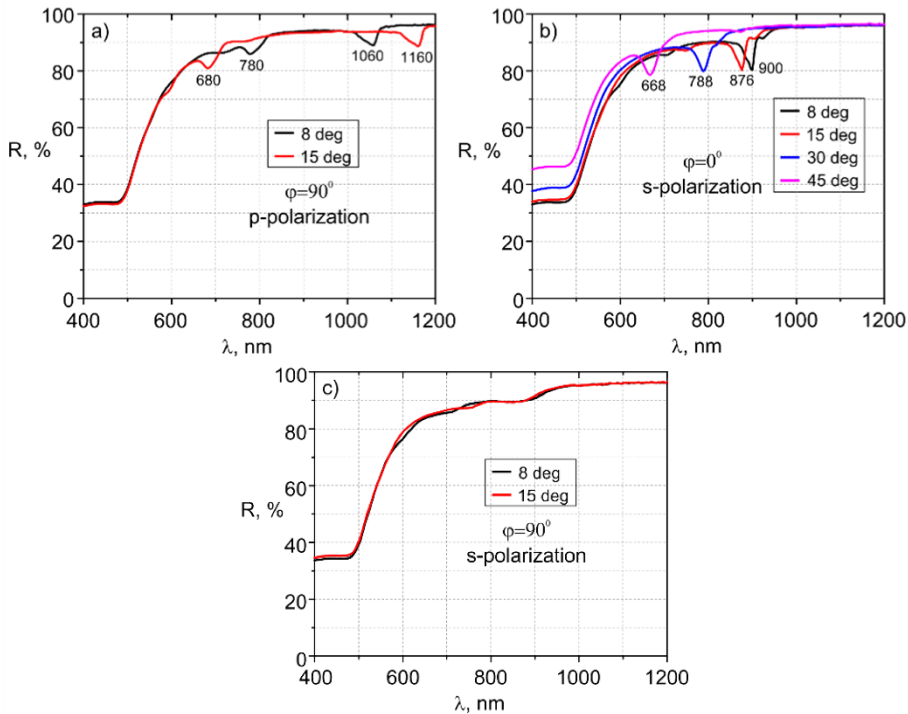


**Figure 4.5.10.** Reflectance spectra of microbumps array with 900 nm period in 50 nm gold film for a) *p*-polarized and b,c) *s*-polarized light when  $\varphi=90^\circ$  (a, c) and  $\varphi=0^\circ$  (b). Spectra were measured for the different angles of light incidence:  $8^\circ$  (black curves);  $15^\circ$  (red curves);  $30^\circ$  (blue curve) and  $45^\circ$  (pink curve).

reflectance (red curve) compared to the thicker film (black curve). The HLPR for 50 nm gold film (black curve in Fig. 4.5.8) is deeper, narrower, and slightly shifted to the shorter wavelengths comparing to the HLPR for 25 nm gold film (red curve in Fig. 4.5.8). These effects can be determined by the size of the fabricated bumps and the space between them.

The period of the microbumps grating determines the place of the HLPR in the reflectance spectra. This is perfectly seen in the reflectance spectra of the gratings with a different period (Fig. 4.5.4 (700 nm), Fig. 4.5.9 (600 nm), and Fig. 4.5.10 (900 nm)). All gratings were fabricated in a 50 nm gold film using a single laser pulse with 1.5 nJ energy. The measured values of the HLPR for the different period gratings are in good agreement with the theoretical estimation.

The analysis of the reflectance spectra of the microbumps gratings with a different period (Fig. 4.5.9 and Fig. 4.5.10) shows that the HLPR for 600 nm is deeper and narrower compared with the HLPR of 900 nm period grating.

By increasing the period, the FWHM (full width at half maximum) of HLPR increases, and the amplitude decreases. For a 900 nm period grating, the HLPR signal for *s*-polarized light (when  $\varphi=90^\circ$ ) becomes very weak and almost disappears (Fig. 4.5.10 c).

The reflectance spectra of gratings with a different period show that the space between microbumps is crucial for the HLPR signal. The smaller the grating period, the deeper and narrower the HLPR signal appears. Narrower FWHM and larger reflectance amplitude are desired because a deeper and narrower resonance dip allows efficient detection of the resonant shift [211].

### Summary

The fabrication of large-scale ( $5\times 5\text{ mm}^2$ ) gold microbumps gratings-coupled hybrid lattice plasmon polaritons surface plasmon resonances (SPRs) in the VIS-NIR range by using a direct laser writing technique was demonstrated. The polarized reflectance and spectroscopic ellipsometry measurements have shown that arrays gratings consisted of gold bumps support hybrid lattice plasmon polaritons modes which are a result of propagated surface plasmon resonance and in-plane Bragg reflections of the grating. The HLPP modes exhibit a modified dispersion relation from the conventionally propagated surface plasmon resonance. The coupling of in-plane Bragg reflections with the propagated surface plasmon resonance leads to ultra-narrow width of the hybrid plasmonic resonances which are comparable with surface-resonances in purely dielectric structures with low losses. The dependence of HLPR wavelengths on the incident angle was in good agreement with theoretical consideration. The presented grating fabrication method shows significant technological progress in the formation of large-scale metallic arrays by using a laser-based technique and opens new possibilities for plasmonic-based applications integrated photonic devices, optical sensors, and nanolasers.

## 5 MAIN RESULTS AND CONCLUSIONS

- The unambiguous experimental evidence of the strong coupling regime in the hybrid TPP-SPP mode was demonstrated for the first time by cutting the part of incident energy spectra with optical filters. Present experimental studies have shown that if the investigated system is in strong coupling this is always enough to excite only one component of the hybrid excitation, for other to be generated.
- The investigation of hybrid plasmonic modes under strong coupling showed that compared to conventional reflection intensity methods, the polarization states-based measurement techniques provide a more detailed information about the mechanisms of strong coupling, as only the polarization states where the strong coupling occur should be singled out.
- The analysis of the in-plane wave vector, which the plasmonics together with TIRE method gives, allows one to obtain more sensitive optical responses from ultrathin graphene-based hybrid nanostructures. Widening of the TPP and the SPP resonances in the hybrid TPP-SPP mode, with the single layer graphene on top of silver, indicates a weakened coupling strength (~6%) between the two modes and the decrease of the quality factor, where such reduction can be explained by the conductivity changes of the silver-graphene/PMMA system.
- The sensitivity of the SPP component of the hybrid TPP-SPP mode had 6.4 times higher sensitivity for BSA proteins adsorbed to the gold surface, than the conventionally used SPR, because the energy losses, experienced in metal, are reduce for the SPP component and as a result the width of the resonance narrows.
- The optical response of ellipsometric parameters  $\Psi(\lambda)$  and  $\Delta(\lambda)$  of the modified QCM-D sensor chip, supporting Tamm plasmon polaritons and cavity modes, exhibited a higher sensitivity to refractive index changes compared with the conventional QCM-D sensor chip. The cavity mode (321 nm/RIU) and TPP (352 nm/RIU) was 49 and 24 times more sensitive, compared to the commercial QCM-D chip.
- The Tamm plasmon polaritons showed 1.5 times higher sensitivity for the biosensing application compared to the cavity mode. It can be explained by the different origins of these excitations, where TPP is the surface electromagnetic wave and the cavity mode is a bulk mode. These differences in optical features of the TPP and CM excitations give



additional advance, allowing to simultaneously determine whether bulk or surface process is dominant.

- The gold microbumps surface lattice arrays fabricated by cost-effective large area ( $5 \times 5 \text{ mm}^2$ ) direct laser writing method allows to generate narrow hybrid lattice plasmon resonances, compared to the single SPP mode. The coupling of the in-plane Bragg reflections with the propagated surface plasmon leads to ultra-narrow resonance (up to 10 nm width) that are comparable by quality to the ones produced by lithography methods.

## 6 SANTRAUKA

### ĮVADAS

Pastaruosius keletą metų plačiai paplito fotonų sąveikos su nanostruktūromis tyrimai, kurie yra potencialūs naujų prototipų, tinkamų nanofotoniniams prietaisams, vystyme. Tokie tyrimai fotonikoje padeda suprasti nanometrų dydžio struktūrose susidarančius optinius sužadinimus bei kaip tokiose nanostruktūrose optinis atsakas priklauso nuo jų dydžio, formos ar periodiškumo. Viena iš nanofotonikos mokslo sričių, kuriai skiriama daug dėmesio, yra plazmonų poliaritonų tyrimai metalinėse struktūrose. Plazmonai yra kolektyvinės laisvųjų krūvininkų metale osciliacijos. Šviesos sąveika su plazmonų rezonansu metalų nanosandarose pradėti tyrinėti dėl elektrinio lauko lokalizavimo į tūrius, mažesnius už difrakcijos ribą, savybės [1].

Kuomet du plazmoniniai sužadinimai sąveikauja tarpusavyje, gali atsirasti nauji fizikiniai reiškiniai. Panašūs, plačiai tyrinėti sąveikos procesai yra plazmonų ir eksitonų sąveika [2,3]. Įvairiuose emiteriuose, tokiuose kaip eksitonai puslaidininkiuose, organiniuose dažuose ar fotochrominėse molekulėse [4-7], gali vykti energijos mainai tarp paviršinio plazmoninio sužadinimo bei eksitono, jeigu šie yra stipriosios sąveikos režime. Dėl šios savybės, sužadinimai, esantys stipriojoje sąveikoje, yra daug žadantys taikant juos nanofotoninėse sistemose naujos kartos plazmoniniams lazeriams (SPASER) [8,9], didelio jautrumo optiniams biojutikliams [10], cheminių reakcijų valdymui [11,12], kambario temperatūros Bose ir Einstein'o kondensatui [8] bei kvantiniuose informacijos apdorojimo įtaisuose [13]. Tačiau, stiprioji sąveika gali būti aptinkama ir visiškai plazmoninėse nanofotoninėse sandarose, kuriose du skirtingos ar vienodos prigimties plazmoniniai sužadinimai stipriai sąveikauja vienas su kitu [14]. Pagrindinė stipriosios sąveikos režimo savybė yra energijos mainų tarp dviejų plazmoninių sužadinimų (ar plazmono ir eksitono) sparta, kur mainai įvyksta per sistemos koherentiškumo laiką [15]. Tokia energijos mainų sparta viršija slopinimo metale spartą, o dėl šios priežasties susidaro nauja hibridinė plazmoninė moda. Tačiau, pagrindinis skirtumas tarp plazmono-eksitono ir plazmono-plazmono sąveikų yra toks, kad plazmono-eksitono atveju sistema suformuoja naują hibridinį poliaritoną, tuo tarpu plazmonas-plazmonas savaime yra poliaritonas, kuris formuoja naują poliaritoninę būseną, kurioje abu pavienių plazmonų poliaritonai savaime yra sudėtyje. Pagrindinė stipriosios sąveikos režimo savybė yra ženkli poliaritono energijos lygmenų kontrolė bei koherentinė, delokalizuota naujos poliaritono modos prigimtis

[16,17]. Publikacijų, skirtų stipriosios sąveikos režimui tarp dviejų plazmoninių sužadinių bei jų taikymams, skaičius yra gana mažas [18-20].

Šioje disertacijoje pristatomi tyrimai, skirti hibridinių šviesos-medžiagos sąveikos poliaritonų modų gilesniam supratimui, kuriais siekiama pademonstruoti jų svarbą pradedant fundamentinėmis savybėmis ir baigiant jų pritaikymu nanofotoninėse struktūrose, minėtose anksčiau. Šiuose tyrimuose pristatomas paprastas metodas, taikant optinius filtrus, kuriuo pirmą kartą eksperimentiškai pademonstruota stiprioji sąveika hibridinėse Tamm'o ir paviršinių plazmonų poliaritonų (trump. TPP-SPP) modose (4.1 skyrius). Taip pat, buvo parodyta, kad dėl stipriosios sąveikos tarp hibridinio plazmoninio sužadimo TPP ir SPP komponentų sistema jaučia grafeno monosluoksnį, nusodintą ant metalo paviršiaus (4.2 skyrius). Hibridinės plazmoninės modos sąveikos stiprumo keitimas tarp grafeno monosluoksnio ir PMMA sluoksnio, esančių ant nanofotoninės-plazmoninės struktūros, leidžia charakterizuoti grafeno optines savybes.

Kitose šios disertacijos dalyse pristatomas hibridinių poliaritoninių sužadinių taikymas biojutikliams. Buvo tiriama optimizuoto jautrumo hibridinio TPP-SPP sužadimo sistema, kuri buvo lyginama su pavienio SPR moda, ant jutiklių aukso paviršiaus formuojant BSA baltymo sluoksnį (4.3 skyrius). Hibridinių TPP-SPP bei pavienių SPR sužadinių dispersiniai sąryšiai buvo naudojami hibridinės TPP-SPP modos sustiprintam elipsometrinių parametru jautrumui paaiškinti. Taip pat, buvo pademonstruota nebrangiai pagaminama 1D plazmoninė fotoninė struktūra užauginta ant komercinio kvarco kristalo mikrobalanso (QCM-D) jutiklio. Tokioje struktūroje generuojami Tamm'o plazmonai ir rezonansinės (angl. *cavity mode*) modos, kurių dėka sustiprinamas optinis signalas kombinuotame spektrinės elipsometrijos ir kvarco kristalo mikrobalanso metode (4.4 skyrius).

Pabaigoje, skyriuje 5.5, pademonstruotas tiesioginio lazerinio rašymo būdu pagamintas didelio ploto mikrogumbų gardelių masyvas, kuriame generuojami hibridiniai gardelių plazmonai poliaritonai (trump. HLPP) regimojo ir artimojo infraraudonųjų spindulių spektro ruožuose. Šiose struktūrose žadinami siauri rezonansai su mažais energijos nuostoliais rodo potencialų tiesioginio lazerinio rašymo metodo, kaip pigaus, greito ir didelį plotą apimančio, poveikį kuriant norimų optinių savybių integruotus fotoninius prietaisus. Toks HLPP rezonansų pritaikymas, kartu su stipriosios sąveikos režimu juose, lemia sumažėjusius nuostolius, o, dėl šios priežasties, ir padidėjusį paviršinės bangos sklidimo nuotolį bei pagerėjusį tokių plazmoninių sužadinių koherentiškumą, ir žada pažangias optines savybes.

## TIKSLAI

Šioje disertacijoje pristatomų tyrimų tikslas buvo ištirti optinį atsaką įvairiuose hibridiniuose plazmoniniuose sužadiniuose, tokiuose kaip SPP, TPP ir HLPP. Pagrindinis šių tyrimų objektas buvo hibridinių TPP-SPP modų žadinimas, taikant visiškojo vidaus atspindžio elipsometriją (trump. TIRE) bei šių modų taikymas biologinių molekulių detekcijai. Ypač išskiriant tokius tyrimus, kaip:

- Optinių filtrų metodo pritaikymas, panaudojant filtrus daliai žadinančios šviesos spektro nufiltruoti, taip, kad matuojamas spektras būtų padalintas į dvi dalis, kur kiekviename ruože krintančia šviesa būtų žadinama tik viena hibridinės TPP-SPP modos komponentė. Toks metodas leidžia eksperimentiškai tirti stipriosios sąveikos savybes.
- Stipriosios sąveikos pokyčių tarp TPP ir SPP komponentių hibridinėje TPP-SPP modoje dėl grafeno monosluoksnio, esančio tarp PMMA ir sidabro sluoksnių, kuriuo būtų galima valdyti daugiasluoksnės sistemos laidumą bei TPP ir SPP sužadinių optinės dispersijos kreives, tyrimas.
- Hibridinių TPP-SPP modų taikymas padidinto jautrumo biojutikliams ir jų palyginimas su plačiai taikomu pavieniu SPR jutikliu. Dėl stipriosios sąveikos pakitusi optinė dispersija, galėtų būti taikoma hibridinių TPP-SPP modų optimizavimui bei elipsometrinių parametrų TIRE konfigūracijoje jautrumo kontrolei.
- Pritaikyti 1D fotonines plazmonines nanostruktūras, suformuotas ant komercinio QCM-D jutiklio, kuriose gali būti generuojami Tamm'o plazmonai poliaritonai bei rezonansinės modos, optinio signalo sustiprinimui kombinuotame spektrinės elipsometrijos bei kvarco kristalo mikrobalsno metode.
- Pritaikyti aukso mikrogumbų gardelių masyvą, pagamintą tiesioginio lazerinio rašymo būdu, hibridinių gardelių plazmoninių rezonansų, kurie pasižymi itin siaurais pločiais, palyginamais su litografijos metodais pagamintų gardelių rezonansų kokybe, generavimui.

### Uždaviniai tikslams pasiekti:

- Išvystyti paprastą eksperimentinį metodą, kuriame taikant optinius filtrus, dalis krintančios šviesos spektro nufiltruojama taip, kad būtų žadinama tik viena hibridinio TPP-SPP sužadimo komponentė.
- Naudojant fotoninio kristalo/aukso struktūrą, sužadinti visą hibridinės TPP-SPP modos bei dalį jos (tik TPP ar SPP) spektrų visiškojo vidaus atspindžio elipsometrijos konfigūracijoje.

- Ištirti stipriosios sąveikos įtaką hibridinio TPP-SPP sužadavimo optinei dispersijai, atskiriant TPP ir SPP šakas hibridinio sužadavimo dispersijų kreivėse.
- Palyginti grafeno monosluoksnio įtaką pavienių Tamm'o plazmonų poliaritonų kintamo kampo spektrinės elipsometrijos optiniam atsakui su hibridinių TPP-SPP modų, esančių stipriosios sąveikos režime, TIRE optiniu atsaku.
- Išvystyti 1D fotoninio kristalo/sidabro/grafeno/PMMA daugiasluoksnės struktūros optinį modelį, aprašantį hibridinių TPP-SPP modų stipriąją sąveiką ir žadinimą.
- Pritaikyti hibridinius TPP-SPP kaip jutiklio zondą, juos panaudojant GCSF receptoriaus imobilizavimo bei BSA baltymų sluoksnio formavimosi ant aukso paviršiaus tyrimams. Taip pat palyginti šių modų elipsometrinių parametrų jautrumą su paviene SPR moda.
- Atlikti 1D plazmoninės nanofotoninės struktūros, palaikančios TPP ir rezonansines modas, kurios gali būti generuojamos ant modifikuoto QCM-D jutiklio, skaitmeninius modeliavimus.
- Palyginti suformuoto baltymų sluoksnio ant modifikuoto QCM-D jutiklio, kuriame generuojamos TPP ir rezonansinės modos, elipsometrinių parametrų  $\Psi(\lambda)$  ir  $\Delta(\lambda)$  jautrumus su tradiciniu QCM-D jutikliu kombinuotame SE ir kvarco kristalo mikrobalsno metode.
- Pamatuoti aukso mikrogumbų hibridinių gardelių plazmonų elipsometrinių parametrų optinį atsaką ir charakterizuoti optines dispersijos bei rezonansų savybes.
- Paaiškinti HLPP rezonansų, pagamintų tiesioginio lazerinio rašymo būdu, fizikinį principą.

## **MOKSLINIS NAUJUMAS**

Šioje disertacijoje atlikti eksperimentiniai tyrimai yra šiuo metu sparčiai besivystančioje plazmonikos ir nanofotonikos, nagrinėjančioje rezonansinę fotonų sąveiką su nanostruktūromis, srityje.

Pagrindinis šio darbo naujumas yra pirmą kartą pademonstruotas eksperimentinis stipriosios sąveikos tarp TPP ir SPP sužadimų hibridinėje TPP-SPP modoje režimas, derinant krintančios šviesos spektrą optinių filtrų pagalba. Eksperimentiškai buvo įrodyta, jeigu viena hibridinės modos komponentė yra sužadinama ties jos rezonansiniu dažniu, kita taip pat egzistuos ir galės būti valdoma per stipriosios sąveikos tarp TPP ir SPP

režimą. Energijos mainai tarp TPP ir SPP komponentių demonstruoja hibridinių TPP-SPP modų taikymo integruotos fotonikos įtaisuose potencialą.

Plazmoninių struktūrų, pagrįstų stipriąja sąveika, tyrimų fone, grafeno monosluoksniu įtaka sidabro laidumui parodė, kad stiprioji sąveika ir elektronų, dalyvaujančių hibridinių plazmoninių sužadinių sąveikoje, koncentracija galėtų būti apibūdinta kaip kokybės rodiklis, leidžiantis valdyti tiriamų nanostruktūrų optinę dispersiją.

Darbe buvo parodyta, kad hibridinių TPP-SPP bei pavienių TPP sužadinių taikymas biomolekulių jutikliams leidžia sustiprinti sistemos optinį atsaką. Hibridiniai TPP-SPP sužadiniai ir stipriosios sąveikos režimas buvo pirmą kartą panaudoti biologinių molekulių detekcijai. Buvo nustatyta, kad hibridinių plazmoninių modų jautrumas gali būti kontroliuojamas naudojant stipriosios sąveikos tarp TPP ir SPP komponentių efektą. Toks pritaikymas sumažina energijos nuostolius metale, kuriuos patiria SPP komponentė, todėl plazmoninis rezonansas susiaurėja. Buvo pastebėta, kad ant jutiklio paviršiaus formuojant BSA baltymų sluoksnį optimizuota hibridinės TPP-SPP modos sistema pasižymėjo didesniu jautrumu nei įprastai naudojamo SPR jutiklio. Tamm'o plazmonų poliaritonų optinės dispersijos savybė, kuomet laisvoje erdvėje krintančios šviesos bangos vektorius yra visuomet didesnis už TPP bangos vektorių ir TPP galima žadinti tiesiogiai nenaudojant prizmės, suteikia galimybę padidinti jutiminio paviršiaus spektrinės elipsometrijos optinio signalo jautrumą, nenaudojant visiškojo vidaus atspindžio konfigūracijos. Kiek yra žinoma, tai pirmas kartas, kuomet Tamm'o plazmonai poliaritonai ir rezonansinės modos buvo tirti ir taikyti kombinuotame spektrinės elipsometrijos bei kvarco kristalo mikrobalanso metode, sustiprinto elipsometrinių parametrų signalo nuskaitymui.

Tiesioginis lazerinis rašymas buvo pritaikytas metalo mikrogumbų gardelių masyvo, kuriame galima žadinti hibridinius gardelių plazmonų poliaritonus, gamybai. Šie hibridiniai plazmoniniai sužadiniai susidaro dėl sklindančio paviršinio plazmono rezonanso ir nuo mikrogumbų plokštumoje susidaranciu Bragg'o atspindžių sąveikos. HLPP modos, lyginant su SPP, pasižymi pakitusiu dispersiniu sąryšiu. Bragg'o atspindžių sąveika su sklindančiu paviršiniu plazmonu poliaritonu lemia itin siaurą HLPP rezonanso plotį, kuris dydžiu palyginamas su paviršinėmis bangomis, pasižyminčiomis mažais nuostoliais – generuojamomis dielektrinėse struktūrose, ar litografijos būdu pagamintų struktūrų plazmoniniais sužadimais. Pademonstruotas gardelių masyvo gamybos metodas rodo svarbų technologinį progresą didelio ploto metalinių gardelių formavimo, taikant tiesioginį lazerinį rašymą, vystyme ir atveria naujus taikymus plazmoniniais sužadimais grįstiems integruotos fotonikos įtaisams, optiniams jutikliams bei nanolazeriams.

## **PRAKTINIS PRITAIKYMAS**

Optinių filtrų metodo spektriniuose matavimuose pritaikymas plazmoninių rezonansų sąveikos analizei, leidžia eksperimentiškai nustatyti stipriąją sąveiką tarp dviejų ar daugiau plazmoninių sužadinių. Apibendrinant, ši metodika yra tinkama įvairioms nanofotoninėms struktūroms, gebančioms generuoti paviršines rezonansines būsenas stipriojoje sąveikoje.

Hibridinių plazmoninių modų panaudojimas stipriosios sąveikos režime leidžia sumažinti plazmoninių rezonansų sklidimo nuostolius ir pagerina jų kokybės faktorių, todėl padidėja plazmoninių biojutiklių optinio signalo atsako jautrumas.

Tamm'o plazmonų poliaritonų optinės dispersijos savybė, kuomet šias būsenas galima sužadinti laisvoje erdvėje krintančia šviesa, nes jos bangos vektorius yra visuomet didesnis už Tamm'o bangos vektorius, suteikia galimybę sustiprinti elipsometrinių parametrų optinio atsako jautrumą kombinuotame spektrinės elipsometrijos ir kvarco kristalo mikrobalanso metode, todėl nereikia naudoti visiško vidaus atspindžio konfigūracijos.

Taikant tiesioginio lazerinio rašymo metodą, buvo pademonstruota, kad galima pagaminti didelio ploto metalo submikroninio periodo gardelių masyvus, pasižyminčius itin aukštos kokybės plazmoniniais rezonansais, kurie palyginami su rezonansais, gaunamais tradiciniais litografijos metodais pagamintose struktūrose, todėl taikant tiesioginio lazerinio rašymo metodą gali būti sumažinti gamybos kaštai ir sutrumpintas tokių nanostruktūrų gamybos laikas.

## **GINAMIEJI TEIGINIAI**

- Jei nanofotoninės-plazmoninės struktūros sužadiniai yra stipriosios sąveikos režime, pakanka žadinti tik vieną plazmoninio sužadimo komponentę, kad būtų generuojama visa hibridinė plazmoninė moda, nes abi hibridinės plazmoninės būsenos dispersinės šakos yra neatsiejamai susietos tarpusavyje.
- Stiprioji sąveika tarp TPP ir SPP sumažina sklidimo nuostolius metale (auksas, sidabras) ir susiaurina plazmoninio rezonanso plotį, dėl ko optinio signalo jautrumas lūžio rodiklio pokyčiams jutiklio paviršiuje padidėja.
- TPP ir rezonansinės modos, generuojamos 1D plazmoninėje nanofotoninėje struktūroje, pagamintoje ant standartinio QCM jutiklio,

sustiprina elipsometrinių  $\Psi(\lambda)$  ir  $\Delta(\lambda)$  parametrų optinio signalo atsaką kombinuotame SE-QCM metode.

- Aukso mikrogumbų gardelių masyvuose, pagamintuose tiesioginio lazerinio rašymo būdu, galima žadinti siaurus hibridinių gardelių plazmonų rezonansus, pasižyminčius mažesniais nuostoliais bei modifikuotomis dispersinėmis savybėmis.

## **Autoriaus įnašas**

Šio darbo autorius atliko visus elipsometrijos matavimus, pateiktus mokslinėse publikacijose, pristatomose šioje disertacijoje bei dalyvavo grafeno, naudoto stipriosios sąveikos hibridinėje TPP-SPP modyje, Ramano spektroskopijos matavimuose. Taip pat, atliko realaus laiko baltymų kinetikų matavimus baltymų imobilizacijos bei baltymų sluoksnio formavimo procesą. Autorius parengė 1-3 numeriais sąraše pažymėtas publikacijas, taip pat prisidėjo prie 4, 5 publikacijų rengimo bei recenzavimo proceso.

## LITERATŪROS APŽVALGA

Šiame skyriuje pateikiama literatūros apžvalga su disertacijoje pristatomais darbo tikslais ir uždaviniais susijusiomis temomis. Literatūros apžvalgos skyrius suskirstytas į tris poskyrius, kuriuose aptariami stipriosios sąveikos reiškiniai, fotoninių kristalų savybės bei plazmoniniai reiškiniai.

Poskyryje 2.1 supažindinama su stipriosios sąveikos reiškiniais įvairiose sistemose: plazmonas-eksitonas, rezonansinė moda-eksitonas, atomo, įterpto rezonatoriuje, sąveika bei plazmonas-plazmonas. Aprašoma dviejų osciliatorių sąveika ir sąveikos stiprumo kiekybinis įvertinimas. Analizuojamas stipriosios sąveikos reiškinys, susidarantis tarp dviejų (ar daugiau) sąveikaujančių osciliatorių, kurių sąveika yra tokia stipri, kad šių osciliatorių energijų lygmenys pakinta, lyginant juos su pradiniais pavienių osciliatorių lygmenimis. Tuomet, osciliatorių sistema, esanti stipriojoje sąveikoje, tampa hibridine, o energijos mainai tarp osciliatorių vyksta greičiau, nei laikas per kurį hibridinė sistema patiria nuostolius. Tokie reiškiniai yra itin patrauklūs, norint šiuos sužadinius panaudoti plazmoninių lazerių (trump. SPASER) taikymuose, integruotuose fotoniniuose įtaisuose ar cheminių reakcijų valdyme.

Poskyryje 2.2 yra pateikiamos 1D periodinių struktūrų, vadinamų fotoniniais kristalais (trump. PC), savybės. Tokiose struktūrose lūžio rodiklis kinta viena kryptimi, o kitomis dvejomis yra homogeninis. Trumpai pristatomas fotoninės draustinės juostos, kurioje tam tikros energijos fotonai



nepraleidžiami per struktūrą, susidarymo mechanizmas. Tokios fotoninės struktūros yra aktualios siekiant žadinti Tamm'o plazmonus poliaritonus (trump. TPP), kurie aprašomi 2.3.1 skirsnyje.

Paskutiniame literatūros apžvalgos poskyryje (2.3 poskyris) aprašomi paviršiniai plazmoniniai sužaditimai: Tamm'o plazmonai poliaritonai, paviršiniai plazmonai poliaritonai (trump. SPP), hibridinės Tamm'o-paviršinių plazmonų poliaritonų būsenos (trump. TPP-SPP) bei hibridiniai gardelių plazmonų poliaritonai (trump. HLPP). Skirsnyje 2.3.1 apibūdinami TPP būsenų žadinimo principai, šių būsenų optinės savybės bei jų dispersiniai sąryšiai. Tamm'o plazmonai yra paviršinės bangos susidaranti metalo ir 1D PC sandūroje. Tamm'o plazmonai gali būti žadinami tiesiogiai krintančia šviesa ir jų generavimui nėra reikalingos prizmės. Taip yra dėl to, kad laisvoje erdvėje sklindančios šviesos bangos vektorius yra visuomet didesnis nei TPP. Tuo tarpu, paviršinių plazmonų poliaritonų (2.3.2 skirsnis) bangos vektorius visuomet yra didesnis nei laisvoje erdvėje sklindančios bangos, todėl tokioms bangoms žadinti naudojamos prizmės bangos vektoriui padidinti. O panaudojus TPP struktūrą su SPP žadinimo konfigūracija, galima generuoti hibridinius TPP-SPP sužadimus (aprašomi 2.3.3 skirsnyje), kuriuose, esant tam tikroms sąlygoms, gali būti stipriosios sąveikos režimas. Taip pat, stiprioji sąveika gali būti hibridinių gardelių plazmonų poliaritonų sužadimuose, kurie susidaro periodinėse gardelių struktūrose, aprašomose 2.3.4 skirsnyje.

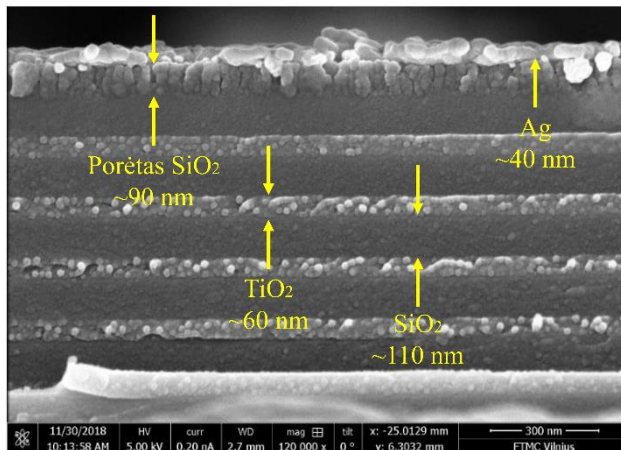
## METODAI

Šiame skyriuje aprašomi disertacijos tyrimuose taikyti metodai ir jų principai.

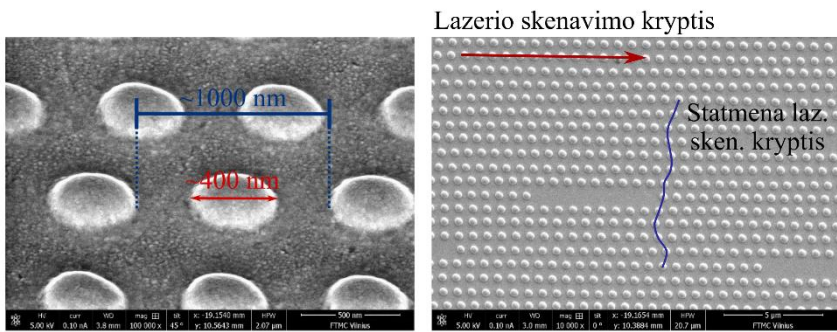
Poskyryje 3.1 pristatomi taikyti optiniai poliarizuotos šviesos matavimo metodai: spektrinė elipsometrija (trump. SE) bei visiškojo vidaus atspindžio elipsometrija (trump. TIRE), kuriais matuojamas  $p$  ir  $s$  poliarizacijų būsenų intensyvumų santykis (elipsometrinis parametras  $\Psi$ ) bei fazių skirtumas (elipsometrinis parametras  $\Delta$ ). Darbe naudoti du kintamo kampo spektrinės elipsometrijos įtaisai – gamintojo J. A. Woollam „M-2000X“ ir „RC2“ modeliai, kurių matuojamas spektro ruožas atitinkamai yra 245-1000 nm ir 210-1700 nm, o matuojamų kampų ruožas 45°-90° ir 20°-90°.

Šioje disertacijoje aprašomų tirtų fotoninių-plazmoninių struktūrų gamybos metodai pateikiami 3.2 poskyryje. Daugiasluoksnės fotoninės struktūros su plonais metalų sluoksniais buvo gaminamos jonų pluošto dulkinimo ir magnetroninio dulkinimo metodais (3.2.1 skirsnis). Fotoniniai kristalai buvo gaminami iš  $\text{TiO}_2$  (60 nm)/  $\text{SiO}_2$  (110 nm) 6 bei 10 dvisluoksnių, atitinkamai dengiamų ant BK7 ir kvarco monokristalo/aukso padėklų. Taip pat buvo pagamintas 6  $\text{TiO}_2$  (120 nm)/ $\text{SiO}_2$  (200 nm) dvisluoksnių fotoninis kristalas. PC struktūros buvo padengiamos 40 nm Au ar Ag sluoksniu. Periodinių gardelių masyvo, taikomo hibridiniams gardelių plazmonų rezonansams generuoti, gamybai buvo naudojamas tiesioginio lazerinio rašymo metodas, kuris plačiau aprašomas 3.2.2 skirsnyje.

Nanofotoninių struktūrų charakterizavimo metodai, taikyti šiame darbe, ir rezultatai pateikti 3.3 poskyryje. Grafeno, naudoto stipriosios sąveikos tyrimams, sluoksnis charakterizuotas taikant Ramano spektroskopijos metodą (3.3.1 skirsnis), iš kurio nustatomas 2D ir G linijų intensyvumo santykis. Iš šio santykio buvo patvirtinta, kad ant sidabro paviršiaus yra nusodintas grafeno monosluoksnis ( $I_{(2D)}/I_{(G)}=2.4$ ). Taip pat, suformuotos struktūros charakterizuotos skenuojančiu elektronų mikroskopu (SEM), kur 1D fotoninio kristalo su plonu Ag sluoksniu skerspjuvio mikroskopinė nuotrauka pateikta 1 pav. Iš SEM mikroskopinių nuotraukų įvertintos ruošinių struktūros bei sluoksnių storiai. Remiantis mikrogumbų gardelių masyvų SEM matavimais (2 pav.) nustatytas 700 nm mikrogumbų gardelių periodas, 400 nm gumbo plotis ir ~90 nm gumbo aukštis.



**1 pav.** Fotoninio kristalo su 40 nm sidabro sluoksniu skerspjuvio SEM mikroskopinė nuotrauka.



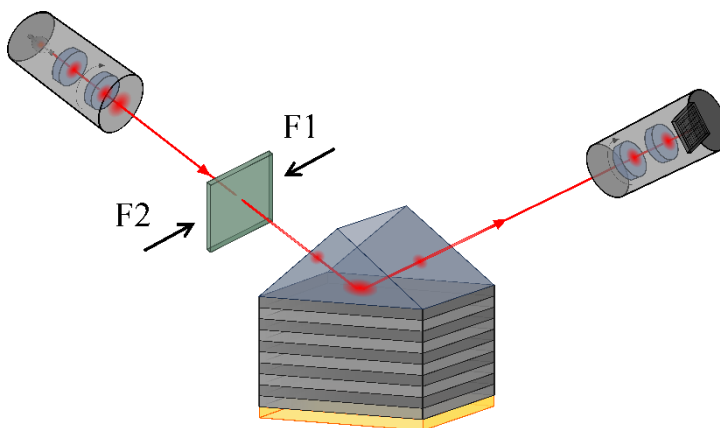
**2 pav.** Mikrogumbų SEM mikroskopinės nuotraukos. Gumbo plotis 400 nm, o spindulio plotis atitinka 1000 nm (kairė). Gardelė tvarkingai išsidėsčiusi lazerio skenavimo kryptimi (dešinė).

Baltymų sluoksnių formavimo principai pristatomi 3.4 poskyryje. Čia aprašomi GCSF receptoriaus bei BSA baltymų sluoksnių adsorbcijos, prie savatvarkiu monosluoksniu (SAM) modifikuoto Au paviršiaus, metodai bei aprašomi aukso paviršiaus paruošimo, baltymų aktyvavimo bei adsorbcijos procesai.

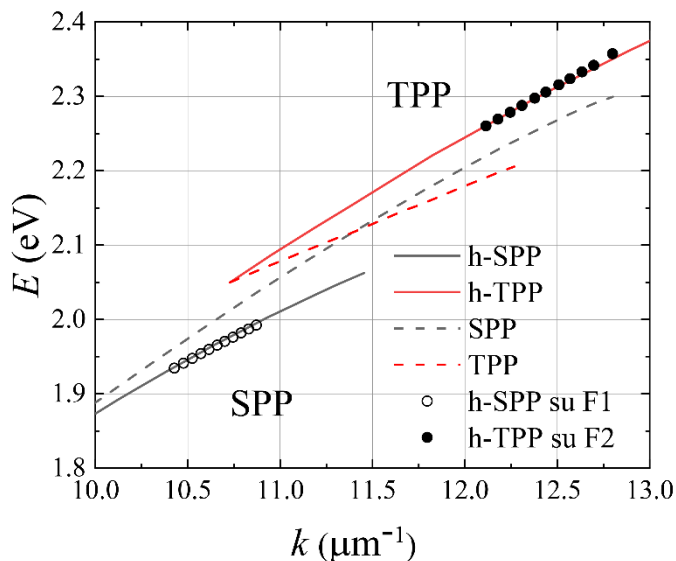
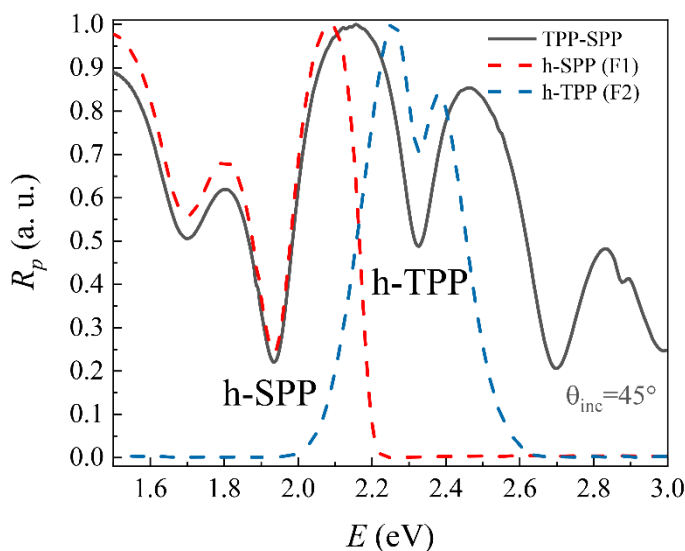
## REZULTATAI

Ketvirtajame skyriuje yra pateikiami šio darbo rezultatai. Skyrius yra suskirstytas į 5 poskyrius, kuriuose analizuojami: stiprioji sąveika hibridinėse Tamm'o plazmonų-paviršinių plazmonų poliaritonuose, hibridinių TPP-SPP modų taikymas biojutikliuose, biojutiklių optinio signalo stiprinimas, panaudojant TPP ir rezonansines modas bei hibridinių gardelių plazmonų rezonanso reiškinys aukso mikrogumbų gardelių masyvuose.

Tyrimuose, aprašomuose 4.1 poskyryje, buvo eksperimentiškai parodyta hibridinio TPP-SPP plazmoninio sužadavimo stiprioji sąveika tarp TPP ir SPP komponentių, panaudojant optinius filtrus, kuriais nufiltruojama viena hibridinio sužadavimo komponentė (arba TPP, arba SPP). Filtrai visiškojo vidaus atspindžio elipsometrijos schemoje (3 pav.) buvo įterpiami tarp šviesos šaltinio ir bandinio, o filtrų pralaidumo spektrai parenkami taip, kad pilnai išfiltruotų vieną komponentę, tačiau kita komponentė būtų praleidžiama. Tamm'o plazmono poliaritono komponentei nufiltruoti buvo pasirinktas Schott OG 590 (F1), o SPP komponentės pašalinimui – Schott VG 14 (F2) filtrai. Pradžioje pamatuoti spektrai be filtrų, o vėliau atlikti matavimai nufiltruojant vieno sužadavimo dispersijos šaką, o kitą žadinant. Nustatyta, kad su F1 ir F2 filtrais nufiltruoti TPP ir SPP komponentių spektrai, esančių atitinkamai 533 nm ir 641 nm, atkartoja pilną hibridinio TPP-SPP sužadavimo spektrą (4 pav. viršuje). Jeigu energijos mainai tarp dviejų osciliatorių įvyksta greičiau, nei kad sistema patiria energijos nuostolius metale, tuomet tokia sistema yra stipriojoje sąveikoje. Tokiomis sąlygomis sužadinių energijos vertės pasislenka, lyginant su pradinėmis jų vertėmis, o sužadimas tampa



**3 pav.** Visiškojo vidaus atspindžio elipsometrijos schema, hibridinių TPP-SPP modų stipriosios sąveikos tyrimams, taikant filtrų metodą.

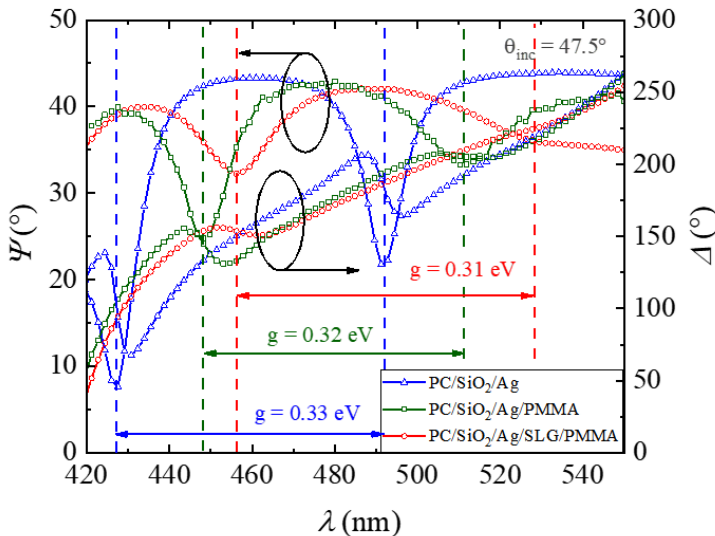


**4 pav.** Hibridinio TPP-SPP sužadavimo be ir su F1, F2 filtrais atspindžio spektrai (viršuje) ir dispersinis sąryšis (ištisinės linijos ir apskritimai) bei pavienių TPP ir SPP būsenų dispersija (brūkšninės linijos) (apačioje).

hibridiniu ir jo rezonansų tarpusavio sąveika yra neatskiriama susieta. Todėl, su F1 ir F2 filtrais matuoti dispersiniai sąryšiai atitinka pilną hibridinės TPP-SPP modos dispersiją, taip kaip pavaizduota 4 pav. apačioje. Suskaičiuojant pavienių sužadavimų dispersinius sąryšius (brūkšninės linijos 4 pav. apačioje), matyti, kad ties kreivių susikirtimo vieta Rabi energijų tarpas tarp TPP ir SPP komponentų hibridiniame TPP-SPP sužadavime yra lygus 105 meV.

Stiprioji sąveika tarp dviejų rezonansų bus tuomet, kai sąveikos stiprumo dydis  $g$  bus didesnis už  $\frac{1}{4}(\gamma_1 + \gamma_2)$ , kur  $\gamma_1$  ir  $\gamma_2$  yra rezonansų pločiai pusės maksimumo aukštyje (trump. FWHM). Šioje hibridinėje sistemoje didžiausia sąveikos stiprumo vertė ( $g = 0.22$  eV) buvo ties pavienių TPP ir SPP rezonansų susikirtimo tašku. Taip pat, svarbu paminėti, kad analizuojant stipriąją sąveiką, hibridiniuose TPP-SPP sužadiniuose, analizę reikėtų atlikti TM poliarizacijoje, nes TE poliarizacija nedalyvauja sąveikoje su paviršinio plazmono poliaritono komponente. Taigi, matuojant bendrą atspindžio intensyvumą TE komponentė iškraipo hibridinės modos atspindžio spektrą, todėl rezonansų pločiai ir energijos gali būti įvertinami nekorektiškai.

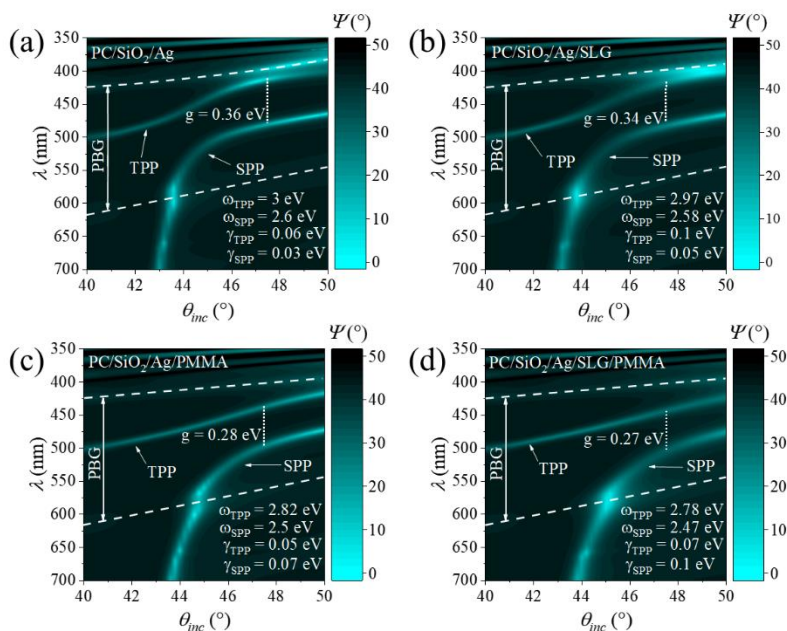
Toliau, 4.2 poskyryje analizuojama grafeno monosluoksnio įtaka hibridinės TPP-SPP modos sąveikos stiprumui. Darbe tirta fotoninio kristalo su sidabro sluoksniu struktūra, ant kurios (sidabro paviršiuje) nusodintas grafenas/PMMA. Struktūrų charakterizavimui ir optinio atsako matavimui taikyti VASE, TIRE, Ramano spektroskopijos ir SEM matavimų metodai. Tokia fotoninė-plazmoninė struktūra su grafeno monosluoksniu stipriojoje sąveikoje yra patraukli dėl jose žadinamų hibridinių TPP-SPP modų potencialaus pritaikymo optiniuose jutikliuose bei integruotuose optiniuose grandynuose. Todėl, buvo pasirinkta išanalizuoti kokią įtaką stipriajai sąveikai daro grafenas (SLG) ir PMMA sluoksniai. Pradžioje įvertinta SLG ir PMMA įtaka pavienio TPP modai, kur PC/Ag struktūros sidabro paviršių padengus PMMA ir SLG/PMMA sluoksniais buvo nustatytas atitinkamai



**5 pav.** Eksperimentiniai elipsometrinių  $\Psi$  ir  $\Delta$  parametų spektrai PC/Ag, PC/Ag/PMMA ir PC/Ag/Gr/PMMA struktūroms.

1 nm ir 3 nm Tamm'o plazmono poliaritono modos poslinkis. Taip pat, tinkinant TPP optinio atsako spektrus, nustatytas 90 nm SiO<sub>2</sub> sluoksnio porėtumas (~30% oro) ir PMMA sluoksnio (~10 nm) bei 0,8 nm SLG (~1-2 grafeno sl.) storiai. Hibridinių TPP-SPP modų TIRE matavimai buvo atlikti naudojant fokusavimo optiką, kur ant prizmės pagrindo krintančio spindulio diametras yra ~250-300 μm. TIRE matavimai atlikti ties 47,5° šviesos kritimo kampu (5 pav.) ir palyginti tarp PC/Ag, PC/Ag/PMMA ir PC/Ag/SLG/PMMA struktūrų, o iš šių matavimų buvo nustatyti sąveikos stipriai. Nuo pradinės PC/Ag struktūros, kurios  $g = 0,33$  eV, užnešus 10 nm PMMA sluoksnį, sąveikos stipris sumažėja iki 0,32 eV, o ant Ag paviršiaus užnešus SLG/PMMA, jis sumažėja iki 0,31 eV. Svarbu paminėti, kad hibridinio TPP-SPP sužadavimo SPP komponentė yra jautresnė lūžio rodiklio pokyčiams prie metalo paviršiaus, tuo tarpu TPP komponentės optinio atsako pokytis vyksta dėl sąveikos stiprumo pokyčių tarp abiejų hibridinio TPP-SPP sužadavimo komponentių. Taip pat, grafeno ir PMMA sluoksnių įtaka sąveikos stiprumui buvo analizuota iš modeliuotų dispersinių sąryšių (6 pav.), iš kurių nustatyta sąveikos stiprumo mažėjimo tendencija ant Ag paviršiaus užnešus grafeną.

Ant Ag paviršiaus užneštas SLG/PMMA lemia TPP ir SPP komponentių rezonansų išplitimą, kuris įvyksta dėl sumažėjusio sąveikos stiprumo, t. y.

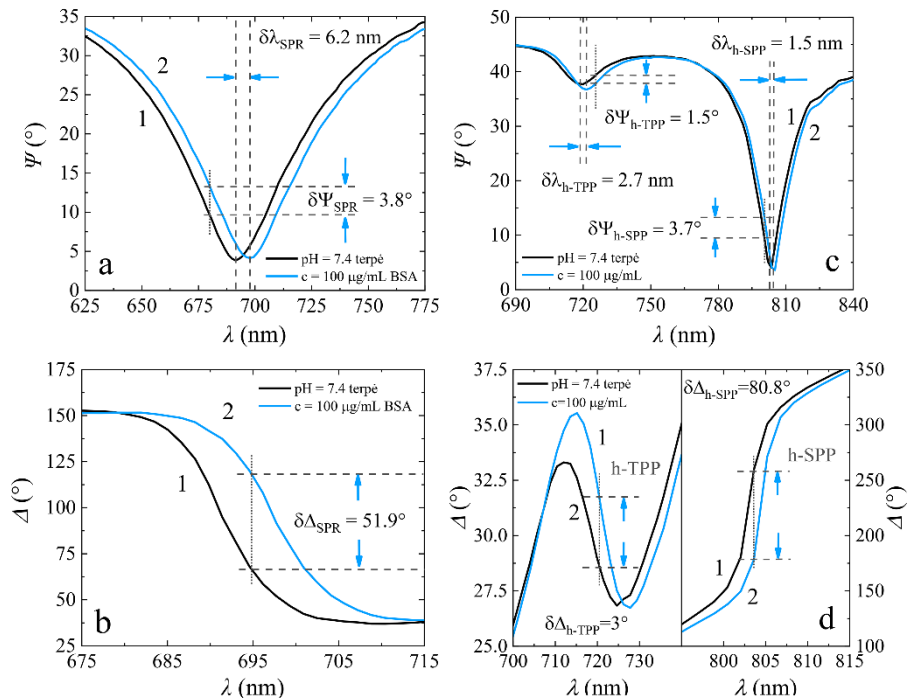


**6 pav.** Modeliuoti hibridinių TPP-SPP modų dispersiniai sąryšiai PC/Ag (a), PC/Ag/SLG (b), PC/Ag/PMMA (c) ir PC/Ag/SLG/PMMA (d) struktūrose.

sužadiniams padidėjusių nuostolių. Toks išplitimas gali būti paaiškintas laidumo ant sidabro paviršiaus pokyčiu.

Hibridinių Tamm'o-paviršinių plazmonų poliaritonų, esančių stipriojoje sąveikoje, taikymas biojutikliams pristatomas 4.3 poskyryje. Biologinių molekulių detekcijai skystuose plačiai naudojamas paviršiaus plazmonų rezonanso (trump. SPR) metodas. Tačiau, šių rezonansų jautrumo padidinimo galimybės yra ribotos, nes rezonanso plotis yra didelis dėl sugerties ir sklaidos nuostolių metale. Plazmonais grįstų biojutiklių jautrumas gali būti padidintas sumažinus energijos nuostolius metale, o tai galima padaryti panaudojus stipriąją sąveiką hibridinėse TPP-SPP modose.

Šiuose tyrimuose hibridiniai TPP-SPP sužadiniai pritaikyti prie metalo paviršiaus adsorbuotų biologinių molekulių detekcijai, o gauti rezultatai palyginti su tradiciniu SPR sužadiniu. Pradžioje atlikti GCSF receptoriaus imobilizavimo prie jutiklio paviršiaus TIRE matavimai tiek su SPR, tiek su TPP-SPP modas generuojančiais jutikliais. Šviesos kritimo kampas SPR ir TPP-SPP sužadiniams atitinkamai buvo  $70^\circ$  ir  $62,5^\circ$ . Hibridinių TPP-SPP modų jautrumo parametrus įvertinti sistema buvo optimizuojama, parenkant

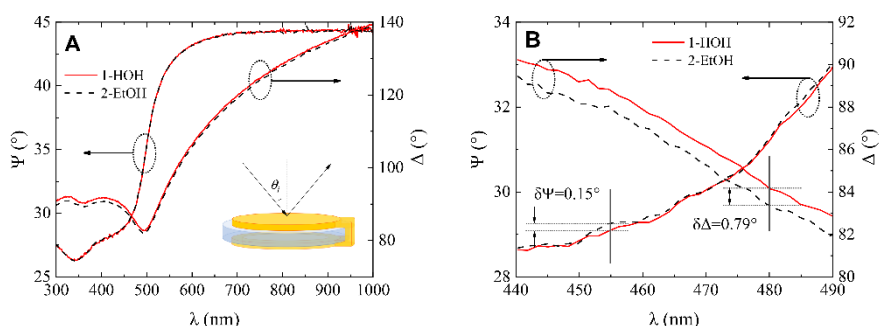


**7 pav.** Elipsometrinių parametų a)  $\Psi(\lambda)$  ir b)  $\Delta(\lambda)$  pavieniam SPR bei c)  $\Psi(\lambda)$  ir d)  $\Delta(\lambda)$  hibridinei TPP-SPP modai spektrai prieš (1) ir po (2) BSA imobilizavimo.

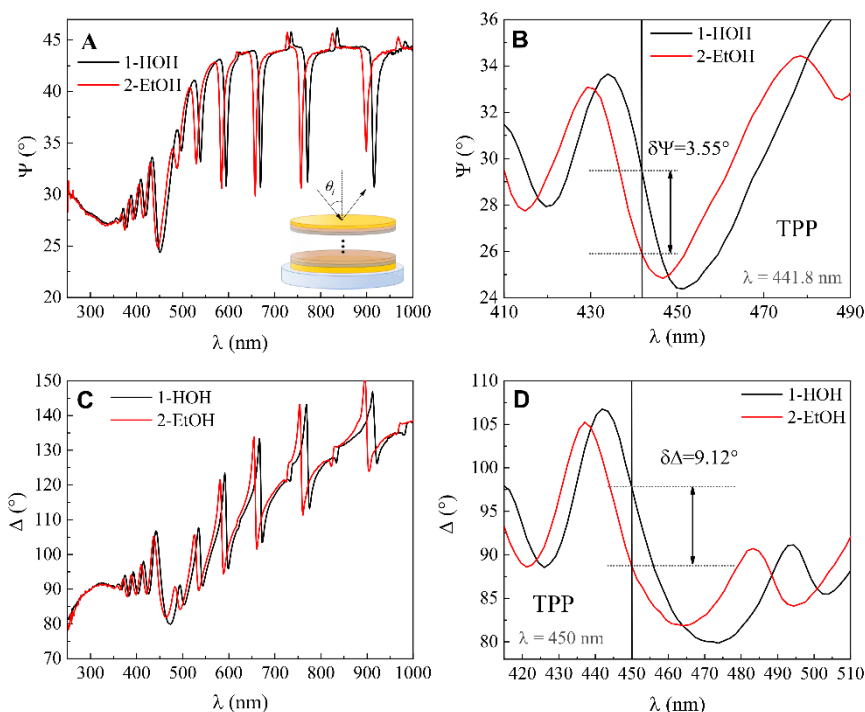


šviesos kritimo kampą tokį, kad SPP komponentės rezonanso minimumas būtų kuo gilesnis, t. y. krintančios šviesos bangos vektorius kiek įmanoma labiau sutaptų su laisvų elektronų osciliacijos energija. Atliekant BSA baltymų adsorbcijos prie paviršiaus TIRE matavimus, kritimo kampas SPR ir TPP-SPP modams atitinkamai buvo  $70^\circ$  ir  $64,6^\circ$ . Pagamintos PC/Au struktūros aukso paviršius buvo paruoštas, kad ant jo paviršiaus galėtų vykti BSA molekulių adsorbcija. Įleidus  $100 \mu\text{g/mL}$  BSA baltymų, esančių  $\text{pH}=7,4$  terpėje, tirpalą buvo matuojamas elipsometrinių parametru signalo pokytis (7 pav.), kuris taip pat buvo lyginamas su SPR signalu. Nustatyta, kad hibridinio TPP-SPP sužadavimo SPP komponentės jautrumas buvo didesnis nei pavienio SPR. Dėl sąveikos stiprio kitimo, buvo padidintas elipsometrinio parametro  $\Delta(\lambda)$  jautrumas, kur  $\delta\Delta/\delta\lambda$  SPP komponentei hibridiniame sužadiniame buvo 6,4 karto didesnis ( $\delta\Delta/\delta\lambda=53,9^\circ/\text{nm}$ ) nei pavienio SPR ( $\delta\Delta/\delta\lambda=8,4^\circ/\text{nm}$ ) atveju. Taip pat, svarbu paminėti, kad biologinių molekulių jutikliai, pagrįsti stipriosios sąveikos režimu tarp hibridinio TPP-SPP sužadavimo komponentių, pasižymi ne tik didesniu jautrumu, esančiu dėl sumažėjusių nuostolių SPP komponentei, bet taip pat turi ir antrąjį zondą – TPP komponentę. Dar vienas zondas gali teikti papildomos informacijos apie molekulių adsorbciją prie jutiklio paviršiaus.

Plazmoninės paviršinės bangos (SPR, TPP-SPP) pasižymi optinio signalo sustiprinimu, todėl tokie sužadiniai yra daug jautresni, tačiau ne visuomet matavimų konfigūracijoje galima įterpti prizmę. Vienas tokių pavyzdžių yra kombinuotas spektrinės elipsometrijos ir kvarco kristalo mikrobalsano metodas (SE-QCM), kurio schema neleidžia naudoti prizmės. Tokioje kombinuotoje metodikoje jutiklio SE signalo atsakas lūžio rodiklio prie jutiklio paviršiaus pokyčiams yra mažas, lyginant šį su paviršinėmis bangomis



**8 pav.** Standartinio QCM jutiklio elipsometrinių parametru  $\Psi$  ir  $\Delta$  (A) spektrai bei priartintas A vaizdas (B) vandenyje (raudona) ir etanolyje (juoda brūkšninė linija).



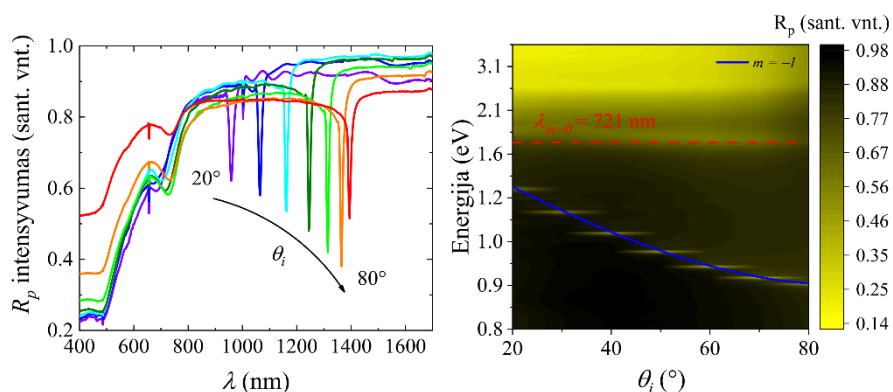
**9 pav.** Modifikuoto QCM jutiklio elipsometrinių parametų  $\Psi$  (A,B) ir  $\Delta$  (C,D) spektrai su priartintu vaizdu (B,C) Tamm'o plazmonui, įleidus vandeni (juoda linija) ir etanolį (raudona linija).

grįstų jutiklių optinio signalo pokyčiais, todėl ieškomi būdai, kaip šį signalą sustiprinti.

Šios disertacijos 4.4 poskyryje yra pristatomas SE signalo sustiprinimas kombinuotame SE-QCM metode, panaudojant modifikuotą QCM jutiklio struktūrą, kurioje generuojami Tamm'o paviršiniai plazmonai polaritonai bei rezonansinės modos. Šiame darbe ant QCM jutiklio, sudaryto iš kvarco kristalo su 200 nm Au sluoksniu, buvo užaugintas fotoninis kristalas su 40 nm Au sluoksniu. Pradžioje – suskaičiuoti struktūrą, palaikančių TPP ir rezonansines modas, dispersiniai sąryšiai bei palyginti su eksperimentiškai matuotais. Įvertinus rezultatus, atlikti spektrinės elipsometrijos (ties 65° šviesos kritimo kampų)  $\Psi$  ir  $\Delta$  parametų pokyčių, keičiant aplinkos lūžio rodiklį, matavimai su standartiniu QCM jutikliu (8 pav.) bei modifikuotu QCM jutikliu (9 pav.). Aplinkos lūžio rodiklis buvo varijuojamas keičiant terpę, kurioje patalpintas jutiklis – iš dejonizuoto vandens ( $n=1.333$ ) į etanolį ( $n=1.361$ ). Šie matavimai parodė, kad modifikuoto QCM jutiklio optinis signalas yra 23 ir 49 kartus atitinkamai TPP ir rezonansinei modai jautresnis

už standartinio QCM jutiklio optinį atsaką. Rezonansinė moda pasižymėjo 2 kartus didesniu elipsometrinių parametų  $\Psi$  ir  $\Delta$  jautrumu nei TPP. Ištyrus jutiklio optinį atsaką į aplinkos lūžio rodiklio pokyčius, buvo atlikti tyrimai su BSA baltymų molekulių adsorbicija prie jutiklio paviršiaus. Buvo nustatyta, kad TPP sužadavimo elipsometrinio parametro  $\Psi$  jautrumas buvo 1,5 karto didesnis nei rezonansinės modos atveju. Tokie skirtingi jautrumai aplinkos lūžio rodiklio ir ant paviršiaus nusėdusios masės pokyčiams gali būti paaiškinti skirtinga šių sužadimų prigimtimi, kur TPP yra paviršinė banga, jautresnė paviršiaus lūžio rodiklio pokyčiams, o rezonansinė moda – tūrinė, jaučianti aplinkos lūžio rodiklio pokyčius.

Paskutiniame 4.5 poskyryje analizuojamos hibridinės gardelių plazmonų modos, kurių žadinimui nėra reikalinga prizmė, todėl šios gardelės tinka tokiems taikymams kaip: integruota optika, integruotiems jutikliams bei plazmoniniams nanolazeriams. Poskyryje aprašomi gardelių masyvai, sudaryti iš mikrogumbų, kurie buvo pagaminti naudojant tiesioginio lazerinio rašymo metodą. Šios struktūros pasižymėjo periodiniu (periodas ~700 nm) mikrogumbų išsidėstymu lazerio skenavimo kryptimi. Tokiose gardelėse, regimojoje ir artimojo infraraudonojo spektrų srityse gali būti žadinamos HLPP modos, pasižyminčios siaurais rezonansais, dėl sumažėjusių energijos nuostolių metale. Šių rezonansų kokybė yra palyginama su litografijos metodais pagamintose struktūrose generuojamais gardelių plazmonų rezonansais. Darbe matuotas HLPP atspindžio spektras  $p$  ir  $s$  poliarizuotai šviesai bei atlikti HLPP rezonansų spektrinės elipsometrijos matavimai esant skirtingiems šviesos kritimo kampams, taip pat pamatuoti šių rezonansų dispersiniai sąryšiai. Spektrinės elipsometrijos matavimai atlikti naudojant fokusavimo optiką, kur spindulys yra suspaudžiamas į  $250 \times 500 \mu\text{m}$  dėmę. Iš



**10 pav.** HLPP modų spektrinės elipsometrijos  $p$  poliarizacijos atspindžio spektrai (kairėje) ir dispersiniai sąryšiai (dešinėje).

šių matavimų (10 pav.) matyti, kad rezonansų pločiai pusės maksimumo aukštyje siekia apie 10 nm. Tuo tarpu, jeigu spindulys fokusuojamas į didesnę dėmę, rezonansų plotis tampa didesnis. Taip yra dėl didesnio skaičiaus mikrogumbų, kuriuos apima platesnis spindulys, todėl apšviečiami ir struktūros defektai. Rezonansai taip pat buvo suskaičiuoti remiantis 4.12 formule. Kaip matyti iš 10 pav., dešinėje esančios skaičiuotos dispersijos kreivė (pažymėta mėlyna linija) sutampa su eksperimentiškai matuotais rezultatais. Taip pat, buvo tirta rezonansų priklausomybė nuo gardelės periodo. Esant didesniems periodams rezonansai išplinta, dėl sumažėjusios sąveikos tarp rezonansų. Todėl, norint gauti siaurus HLPP rezonansus, svarbu tinkamai parinkti periodą bei turėti periodinę struktūrą. Toks tiesioginio lazerinio rašymo pritaikymas leidžia pagaminti gardeles, kuriose generuojami siauri, mažų energijos nuostolių HLPP rezonansai, susidarantys dėl plokštumoje atsirandančių Bragg'o atspindžių sąveikos su paviršiniu plazmonu.

## PAGRINDINIAI REZULTATAI IR IŠVADOS

- Pirmą kartą eksperimentiškai įrodytas stipriosios sąveikos režimas hibridinėje TPP-SPP modoje, optiniais filtrais nufiltruojant dalį krintančios šviesos spektro. Šiais tyrimais parodyta, kad sužadanimams esant stiprioje sąveikoje visuomet pakanka žadinti tik vieną hibridinės modos komponentę, kad būtų generuojama ir kita.
- Hibridinių plazmoninių modų, esančių stiprioje sąveikoje, tyrimai parodė, kad poliarizacijos būsenų matavimais grįsti metodai, lyginant su tradiciniais atspindžio intensyvumo matavimo metodais, teikia daugiau informacijos apie stipriosios sąveikos mechanizmus, nes galima išskirti tik tas poliarizacijos būsenas, kuriose vyksta stipri sąveika.
- TIRE metodas, leidžia gauti jautresnį optinį atsaką nuo itin plonų hibridinių grafeno nanostruktūrų, dėl išilginės bangos vektoriaus komponentės atsirandančios generuojant plazmoninius sužadanimus. Hibridinės TPP-SPP modos TPP ir SPP komponentių išplitimas dėl grafeno monosluoksnio ant sidabro paviršiaus rodo sąveikos stiprio susilpnėjimą (~6%) bei rezonansų kokybės faktoriaus sumažėjimą, kur toks sumažėjimas gali būti paaiškintas per sistemos laidumo pokyčius, dėl grafenas/PMMA struktūros užneštos ant Ag paviršiaus.
- Hibridinių TPP-SPP sužadanimų jautrumas BSA baltymų, nusėdusių ant aukso paviršiaus, sluoksniui buvo 6,4 karto didesnis nei SPR jutiklio, nes panaudojus stipriąją sąveiką energijos nuostoliai metale SPP komponentei sumažėja ir rezonansas susiaurėja.
- Modifikuoto QCM-D jutiklio, kuriame generuojami Tamm'o plazmonai poliaritonai ir rezonansinės modos, optinis elipsometrinių parametrų  $\Psi(\lambda)$  ir  $\Delta(\lambda)$  atsakas pasižymėjo padidėjusiu jautrumu aplinkos lūžio rodiklio pokyčiams, lyginant šį su įprastu QCM-D jutikliu. Rezonansinė moda ir TPP sužadanimas buvo atitinkamai 49 ir 24 kartus jautresnis, nei standartinio QCM-D jutiklio atveju.
- Tamm'o plazmonai poliaritonai pasižymėjo 1,5 karto jautresniu optiniu atsaku BSA baltymų detekcijos tyrimuose, lyginant su rezonansine moda. Toks jautrumų skirtumas gali būti paaiškintas dėl skirtingų TPP ir rezonansinių modų prigimčių, nes TPP yra paviršinė elektromagnetinė banga, o rezonansinė moda – tūrinis sužadanimas. Vienu metu naudojant TPP ir rezonansinę modą šie optinių savybių skirtumai leidžia nustatyti ar dominuoja tūrinis, ar paviršinis procesas.
- Didelio ploto ( $5 \times 5 \text{ mm}^2$ ) aukso mikrogumbų paviršinių gardelių masyvuose, pagamintuose tiesioginio lazerinio rašymo būdu, gali būti

žadinami siauri, lyginant su pavieniu SPP, hibridinių gardelių plazmonų rezonansai. Paviršinio sklindančio plazmono sąveika su gardelės plokštumoje susidaranciais Bragg'o atspindžiais lemia itin siaurus rezonansus (iki 10 nm pločio), kurių kokybė palyginama su litografijos metodais pagamintose struktūrose gaunamais rezonansais.

## 7 PUBLIKACIJŲ SĄRAŠAS

### Mokslinių publikacijų disertacijos tema sąrašas

- P1. E. Bužavaitė-Vertelienė, V. Vertelis and Z. Balevičius. "The experimental evidence of a strong coupling regime in the hybrid Tamm plasmon-surface plasmon polariton mode", *Nanophotonics* **10**, 1565-1571, (2021). (IF=7.923)
- P2. E. Buzavaite-Verteliene, A. Valavicius, L. Grineviciute, T. Tolenis, R. Lukose, G. Niaura, Z. Balevicius, „Influence of the graphene layer on the strong coupling in the hybrid Tamm-plasmon polariton mode“, *Optics Express* **28**, 10308-10319, (2020). (IF=3.833)
- P3. E. Buzavaite-Verteliene, I. Plikusiene, T. Tolenis, A. Valavicius, J. Anulyte, A. Ramanavicius, and Z. Balevicius, „Hybrid Tamm-surface plasmon polariton mode for highly sensitive detection of protein interactions“, *Optics Express* **28**, 29033-29043, (2020). (IF=3.833)
- P4. I. Plikusiene, E. Bužavaitė-Vertelienė, V. Mačiulis, A. Valavičius, A. Ramanavičienė, Z. Balevičius, „Application of Tamm plasmon and cavity modes for biosensing in the combined spectroscopic ellipsometry and quartz crystal microbalance method“, *Biosensors* **11**, 501, (2022). (IF=5.743)
- P5. E. Stankevičius, K. Vilkevičius, M. Gedvilas, E. Bužavaitė-Vertelienė, A. Selskis, Z. Balevičius, “Direct Laser Writing for the Formation of Large-Scale Gold Microbumps Arrays Generating Hybrid Lattice Plasmon Polaritons in Vis–NIR Range”. *Advanced Optical Materials* **9**, 2100027, (2021). (IF=10.050)

### Kitos doktorantūros metu išspausdintos mokslinės publikacijos

- P6. E. Bužavaitė-Vertelienė, V. Maciulis, J. Anulytė, T. Tolenis, A. Baškys, I. Plikusiene, Z. Balevičius, “Total Internal Reflection Ellipsometry Approach for Bloch Surface Waves Biosensing Applications”, *Biosensors* **12**(8), 584, (2022).
- P7. I. Plikusiene, V. Maciulis, A. Ramanaviciene, Z. Balevicius, E. Buzavaite-Verteliene, E. Ciplys, R. Slibinskas, M. Simanavicius, A. Zvirbliene, A. Ramanavicius, “Evaluation of kinetics and thermodynamics of interaction between immobilized SARS-CoV-2 nucleoprotein and specific antibodies by total internal reflection ellipsometry”, *Journal of Colloid and Interface Science* **594**, 195-203, (2021).

- P8. G. Mickiene, I. Dalgėdienė, G. Zvirblis, Z. Dapkunas, I. Plikusiene, E. Buzavaite-Verteliene, Z. Balevicius, A. Rukšėnaitė, M. Pleckaityte, „Human granulocyte-colony stimulating factor (G-CSF)/stem cell factor (SCF) fusion proteins: design, characterization and activity“, *PeerJ* **8**, e9788, (2020). (IF=3.060)

### Konferencijos

- K1. E. Buzavaite-Verteliene, T. Tolenis, A. Valavicius, M. Narkauskaite, Z. Balevicius, Excitation of Bloch surface waves in periodic structures using spectroscopic ellipsometry, *62<sup>nd</sup> International conference for students of physics and natural sciences “Open Readings”*, Vilnius, Lietuva (2019). (stendinis)
- K2. E. Bužavaitė-Vertelienė, S. Tumėnas, T. Tolenis, A. Valavičius, R. Lukošė, Z. Balevičius, “Study of hybrid Tamm-plasmon polaritons mode by total internal reflection ellipsometry”, *8<sup>th</sup> International conference on spectroscopic ellipsometry (ICSE8)*, Barselona, Ispanija (2019). (stendinis)
- K3. I. Plikusienė, E. Bužavaitė-Vertelienė, J. Talbot, T. Tolenis, A. Valavičius, A. Ramanavičius, A. Mickienė, Z. Balevičius, “Total internal reflection ellipsometry of hybrid Tamm – plasmon polaritons mode for biosensing application”, *8<sup>th</sup> International conference on spectroscopic ellipsometry (ICSE8)*, Barselona, Ispanija (2019). (stendinis)
- K4. V. Grasyte, E. Buzavaite-Verteliene, Z. Balevicius, “Dispersion relation analysis of Bloch surface waves and surface plasmon polaritons using total internal reflection ellipsometry”, *63rd International conference for students of physics and natural sciences “Open Readings”*, Vilnius, Lietuva (2020) (atšaukta dėl COVID-19). (stendinis)
- K5. V. Gradauskas, J. Anulytė, E. Bužavaitė-Vertelienė, I. Plikusienė, Z. Balevičius, “(In-situ) study of immobilized receptor binding kinetics by using planar photonic-plasmonic nanostructures for biosensing” *64<sup>th</sup> International conference for students of physics and natural sciences “Open readings”*, Vilnius, Lietuva (2021). (stendinis)
- K6. I. Plikusiene, E. Buzavaite-Verteliene, A. Lisaviciute, G. Mickiene, V. Maciulis, J. Talbot, Z. Balevicius, G. Zvirblis, S. Balevicius, A. Ramanavicius, “Label –free ellipsometric immunosensors based on interaction of genetically engineered ligands with different chimeric receptors”, *31<sup>st</sup> World Congress on Biosensors “Biosensors 2021”*, Nuotoliniu (2021). (stendinis)



- K7. E. Bužavaitė-Vertelienė, V. Vertelis, Z. Balevičius, „Evidence of a strong coupling regime in a photonic-plasmonic structure supporting hybrid Tamm-surface plasmon polaritons“, *23<sup>rd</sup> International Conference-School „Advanced Materials and Technologies 2021“*, Palanga, Lietuva (2021). (stendinis)
- K8. J. Anulytė, E. Bužavaitė-Vertelienė, I. Plikusienė, Z. Balevičius, „Hybrid Tamm-surface plasmon polaritons mode based on planar plasmonic photonic nanostructures for highly sensitive real time biosensing of GCSF and BSA proteins“, *23<sup>rd</sup> International Conference-School „Advanced Materials and Technologies 2021“*, Palanga, Lietuva (2021). (stendinis)
- K9. E. Bužavaitė-Vertelienė, I. Plikusienė, V. Mačiulis, A. Valavičius, A. Ramanavičienė, Z. Balevičius, „Tamm plasmons and cavity modes for biosensing application in a combined spectroscopic ellipsometry and quartz crystal microbalance method“, *65<sup>th</sup> International conference for students of physics and natural sciences “Open readings”*, Vilnius, Lietuva (2022). (žodinis)

## 8 REFERENCES

1. W. L. Barnes, "Surface plasmon–polariton length scales: a route to sub-wavelength optics," *J. Opt. A: Pure Appl. Opt.* **8**(4), S87–S93 (2006).
2. T. K. Hakala, J. J. Toppari, A. Kuzyk, M. Pettersson, H. Tikkanen, H. Kunttu, and P. Törmä, "Vacuum Rabi Splitting and Strong-Coupling Dynamics for Surface-Plasmon Polaritons and Rhodamine 6G Molecules," *Phys. Rev. Lett.* **103**(5), 053602 (2009).
3. J. Fregoni, F. J. Garcia-Vidal, and J. Feist, "Theoretical Challenges in Polaritonic Chemistry," *ACS Photonics* **9**(4), 1096–1107 (2022).
4. P. Andrew, "Energy Transfer Across a Metal Film Mediated by Surface Plasmon Polaritons," *Science* **306**(5698), 1002–1005 (2004).
5. J. Bellessa, C. Bonnand, J. C. Plenet, and J. Mugnier, "Strong Coupling between Surface Plasmons and Excitons in an Organic Semiconductor," *Phys. Rev. Lett.* **93**(3), 036404 (2004).
6. C. Symonds, C. Bonnand, J. C. Plenet, A. Bréhier, R. Parashkov, J. S. Lauret, E. Deleporte, and J. Bellessa, "Particularities of surface plasmon–exciton strong coupling with large Rabi splitting," *New J. Phys.* **10**(6), 065017 (2008).
7. J. T. Hugall, A. Singh, and N. F. van Hulst, "Plasmonic Cavity Coupling," *ACS Photonics* **5**(1), 43–53 (2018).
8. T. K. Hakala, A. J. Moilanen, A. I. Väkeväinen, R. Guo, J.-P. Martikainen, K. S. Daskalakis, H. T. Rekola, A. Julku, and P. Törmä, "Bose–Einstein condensation in a plasmonic lattice," *Nature Phys* **14**(7), 739–744 (2018).
9. P. Berini and I. De Leon, "Surface plasmon–polariton amplifiers and lasers," *Nature Photon* **6**(1), 16–24 (2012).
10. A. Lishchuk, C. Vasilev, M. P. Johnson, C. N. Hunter, P. Törmä, and G. J. Leggett, "Turning the challenge of quantum biology on its head: biological control of quantum optical systems," *Faraday Discuss.* **216**, 57–71 (2019).
11. J. A. Hutchison, T. Schwartz, C. Genet, E. Devaux, and T. W. Ebbesen, "Modifying Chemical Landscapes by Coupling to Vacuum Fields," *Angew. Chem. Int. Ed.* **51**(7), 1592–1596 (2012).
12. C. P. Dietrich, A. Steude, M. Schubert, J. Ohmer, U. Fischer, S. Höfling, and M. C. Gather, "Strong Coupling in Fully Tunable Microcavities Filled with Biologically Produced Fluorescent Proteins," *Advanced Optical Materials* **5**(1), 1600659 (2017).
13. D. G. Baranov, M. Wersäll, J. Cuadra, T. J. Antosiewicz, and T. Shegai, "Novel Nanostructures and Materials for Strong Light–Matter Interactions," *ACS Photonics* **5**(1), 24–42 (2018).
14. P. Törmä and W. L. Barnes, "Strong coupling between surface plasmon polaritons and emitters: a review," *Rep. Prog. Phys.* **78**(1), 013901 (2015).
15. Z. Jacob and V. M. Shalaev, "Plasmonics Goes Quantum," *Science* **334**(6055), 463–464 (2011).

16. A. J. Moilanen, T. K. Hakala, and P. Törmä, "Active Control of Surface Plasmon–Emitter Strong Coupling," *ACS Photonics* **5**(1), 54–64 (2018).
17. K. S. Menghrajani and W. L. Barnes, "Strong Coupling beyond the Light-Line," *ACS Photonics* **7**(9), 2448–2459 (2020).
18. B. I. Afinogenov, V. O. Bessonov, A. A. Nikulin, and A. A. Fedyanin, "Observation of hybrid state of Tamm and surface plasmon-polaritons in one-dimensional photonic crystals," *Appl. Phys. Lett.* **103**(6), 061112 (2013).
19. H. Liu, X. Sun, F. Yao, Y. Pei, F. Huang, H. Yuan, and Y. Jiang, "Optical magnetic field enhancement through coupling magnetic plasmons to Tamm plasmons," *Opt. Express* **20**(17), 19160 (2012).
20. A. Paulauskas, S. Tumenas, A. Selskis, T. Tolenis, A. Valavicius, and Z. Balevicius, "Hybrid Tamm-surface plasmon polaritons mode for detection of mercury adsorption on 1D photonic crystal/gold nanostructures by total internal reflection ellipsometry," *Opt. Express* **26**(23), 30400 (2018).
21. C.-Y. Wang, Y. Sang, X. Yang, S. S. Raja, C.-W. Cheng, H. Li, Y. Ding, S. Sun, H. Ahn, C.-K. Shih, S. Gwo, and J. Shi, "Engineering Giant Rabi Splitting via Strong Coupling between Localized and Propagating Plasmon Modes on Metal Surface Lattices: Observation of  $\sqrt{N}$  Scaling Rule," *Nano Lett.* **21**(1), 605–611 (2021).
22. J. Kasprzak, M. Richard, S. Kundermann, A. Baas, P. Jeambrun, J. M. J. Keeling, F. M. Marchetti, M. H. Szymańska, R. André, J. L. Staehli, V. Savona, P. B. Littlewood, B. Deveaud, and L. S. Dang, "Bose–Einstein condensation of exciton polaritons," *Nature* **443**(7110), 409–414 (2006).
23. G. Rempe, H. Walther, and N. Klein, "Observation of quantum collapse and revival in a one-atom maser," *Phys. Rev. Lett.* **58**(4), 353–356 (1987).
24. M. Brune, J. M. Raimond, P. Goy, L. Davidovich, and S. Haroche, "Realization of a two-photon maser oscillator," *Phys. Rev. Lett.* **59**(17), 1899–1902 (1987).
25. R. J. Thompson, G. Rempe, and H. J. Kimble, "Observation of normal-mode splitting for an atom in an optical cavity," *Phys. Rev. Lett.* **68**(8), 1132–1135 (1992).
26. M. Pelton, M. Sheldon, and J. Khurgin, "Plasmon-exciton coupling," *Nanophotonics* **8**(4), 513–516 (2019).
27. S. I. Azzam, A. V. Kildishev, R.-M. Ma, C.-Z. Ning, R. Oulton, V. M. Shalaev, M. I. Stockman, J.-L. Xu, and X. Zhang, "Ten years of spasers and plasmonic nanolasers," *Light Sci Appl* **9**(1), 90 (2020).
28. L. Shi, T. K. Hakala, H. T. Rekola, J.-P. Martikainen, R. J. Moerland, and P. Törmä, "Spatial Coherence Properties of Organic Molecules Coupled to Plasmonic Surface Lattice Resonances in the Weak and Strong Coupling Regimes," *Phys. Rev. Lett.* **112**(15), 153002 (2014).
29. S. Pirotta, M. Patrini, M. Liscidini, M. Galli, G. Dacarro, G. Canazza, G. Guizzetti, D. Comoretto, and D. Bajoni, "Strong coupling between

- excitons in organic semiconductors and Bloch surface waves," *Appl. Phys. Lett.* **104**(5), 051111 (2014).
30. I.-C. Hoi, C. M. Wilson, G. Johansson, T. Palomaki, B. Peropadre, and P. Delsing, "Demonstration of a Single-Photon Router in the Microwave Regime," *Phys. Rev. Lett.* **107**(7), 073601 (2011).
  31. B. Munkhbat, M. Wersäll, D. G. Baranov, T. J. Antosiewicz, and T. Shegai, "Suppression of photo-oxidation of organic chromophores by strong coupling to plasmonic nanoantennas," *Sci. Adv.* **4**(7), eaas9552 (2018).
  32. Y. Zhu, D. J. Gauthier, S. E. Morin, Q. Wu, H. J. Carmichael, and T. W. Mossberg, "Vacuum Rabi splitting as a feature of linear-dispersion theory: Analysis and experimental observations," *Phys. Rev. Lett.* **64**(21), 2499–2502 (1990).
  33. G. Khitrova, H. M. Gibbs, M. Kira, S. W. Koch, and A. Scherer, "Vacuum Rabi splitting in semiconductors," *Nature Phys* **2**(2), 81–90 (2006).
  34. J. P. Reithmaier, G. Şek, A. Löffler, C. Hofmann, S. Kuhn, S. Reitzenstein, L. V. Keldysh, V. D. Kulakovskii, T. L. Reinecke, and A. Forchel, "Strong coupling in a single quantum dot–semiconductor microcavity system," *Nature* **432**(7014), 197–200 (2004).
  35. T. Yoshie, A. Scherer, J. Hendrickson, G. Khitrova, H. M. Gibbs, G. Rupper, C. Ell, O. B. Shchekin, and D. G. Deppe, "Vacuum Rabi splitting with a single quantum dot in a photonic crystal nanocavity," *Nature* **432**(7014), 200–203 (2004).
  36. E. Peter, P. Senellart, D. Martrou, A. Lemaître, J. Hours, J. M. Gérard, and J. Bloch, "Exciton-Photon Strong-Coupling Regime for a Single Quantum Dot Embedded in a Microcavity," *Phys. Rev. Lett.* **95**(6), 067401 (2005).
  37. X. Fan, P. Palinginis, S. Lacey, H. Wang, and M. C. Lonergan, "Coupling semiconductor nanocrystals to a fused-silica microsphere: a quantum-dot microcavity with extremely high Q factors," *Opt. Lett.* **25**(21), 1600 (2000).
  38. M. Pelton, S. D. Storm, and H. Leng, "Strong coupling of emitters to single plasmonic nanoparticles: exciton-induced transparency and Rabi splitting," *Nanoscale* **11**(31), 14540–14552 (2019).
  39. D. G. Lidzey, D. D. C. Bradley, M. S. Skolnick, T. Virgili, S. Walker, and D. M. Whittaker, "Strong exciton–photon coupling in an organic semiconductor microcavity," *Nature* **395**(6697), 53–55 (1998).
  40. D. G. Lidzey, D. D. C. Bradley, A. Armitage, S. Walker, and M. S. Skolnick, "Photon-Mediated Hybridization of Frenkel Excitons in Organic Semiconductor Microcavities," *Science* **288**(5471), 1620–1623 (2000).
  41. P. A. Hobson, W. L. Barnes, D. G. Lidzey, G. A. Gehring, D. M. Whittaker, M. S. Skolnick, and S. Walker, "Strong exciton–photon coupling in a low-Q all-metal mirror microcavity," *Appl. Phys. Lett.* **81**(19), 3519–3521 (2002).

42. R. Houdré, J. L. Gibernon, P. Pellandini, R. P. Stanley, U. Oesterle, C. Weisbuch, J. O’Gorman, B. Roycroft, and M. Ilegems, "Saturation of the strong-coupling regime in a semiconductor microcavity: Free-carrier bleaching of cavity polaritons," *Phys. Rev. B* **52**(11), 7810–7813 (1995).
43. C. Sönnichsen, T. Franzl, T. Wilk, G. von Plessen, J. Feldmann, O. Wilson, and P. Mulvaney, "Drastic Reduction of Plasmon Damping in Gold Nanorods," *Phys. Rev. Lett.* **88**(7), 077402 (2002).
44. D. Sarid, "Long-Range Surface-Plasma Waves on Very Thin Metal Films," *Phys. Rev. Lett.* **47**(26), 1927–1930 (1981).
45. J. de Torres, P. Ferrand, G. Colas des Francs, and J. Wenger, "Coupling Emitters and Silver Nanowires to Achieve Long-Range Plasmon-Mediated Fluorescence Energy Transfer," *ACS Nano* **10**(4), 3968–3976 (2016).
46. K. Chevrier, J.-M. Benoit, C. Symonds, J. Papparone, J. Laverdant, and J. Bellessa, "Organic Exciton in Strong Coupling with Long-Range Surface Plasmons and Waveguided Modes," *ACS Photonics* **5**(1), 80–84 (2018).
47. D. Wang, J. Guan, J. Hu, M. R. Bourgeois, and T. W. Odom, "Manipulating Light–Matter Interactions in Plasmonic Nanoparticle Lattices," *Acc. Chem. Res.* **52**(11), 2997–3007 (2019).
48. V. G. Kravets, A. V. Kabashin, W. L. Barnes, and A. N. Grigorenko, "Plasmonic Surface Lattice Resonances: A Review of Properties and Applications," *Chem. Rev.* **118**(12), 5912–5951 (2018).
49. Z. Balevičius, "Strong Coupling between Tamm and Surface Plasmons for Advanced Optical Bio-Sensing," *Coatings* **10**(12), 1187 (2020).
50. N. Nefedkin, E. Andrianov, and A. Vinogradov, "The Role of Strong Coupling in the Process of Photobleaching Suppression," *J. Phys. Chem. C* **124**(33), 18234–18242 (2020).
51. B.-S. Song, T. Asano, Y. Akahane, Y. Tanaka, and S. Noda, "Transmission and reflection characteristics of in-plane hetero-photonic crystals," *Appl. Phys. Lett.* **85**(20), 4591–4593 (2004).
52. A. Chutinan and S. Noda, "Waveguides and waveguide bends in two-dimensional photonic crystal slabs," *Phys. Rev. B* **62**(7), 4488–4492 (2000).
53. M. Qiu and S. He, "High-directivity patch antenna with both photonic bandgap substrate and photonic bandgap cover," *Microw. Opt. Technol. Lett.* **30**(1), 41–44 (2001).
54. H. Shen, Z. Wang, Y. Wu, and B. Yang, "One-dimensional photonic crystals: fabrication, responsiveness and emerging applications in 3D construction," *RSC Adv.* **6**(6), 4505–4520 (2016).
55. Lord Rayleigh, "XXV. *Notes on electricity and magnetism*. —III. *On the behaviour of iron and steel under the operation of feeble magnetic forces*," *The London, Edinburgh, and Dublin Philosophical Magazine and Journal of Science* **23**(142), 225–245 (1887).
56. J. D. Joannopoulos, ed., *Photonic Crystals: Molding the Flow of Light*, 2nd ed (Princeton University Press, 2008).

57. J. W. Kłos, M. Krawczyk, Yu. S. Dadoenkova, N. N. Dadoenkova, and I. L. Lyubchanskii, "Photonic-magnonic crystals: Multifunctional periodic structures for magnonic and photonic applications," *Journal of Applied Physics* **115**(17), 174311 (2014).
58. P. S. Maji and R. Das, "Hybrid-Tamm-Plasmon-Polariton Based Self-Reference Temperature Sensor," *J. Lightwave Technol.* **35**(14), 2833–2839 (2017).
59. J. Homola, S. S. Yee, and G. Gauglitz, "Surface plasmon resonance sensors: review," *Sensors and Actuators B: Chemical* **54**(1–2), 3–15 (1999).
60. J. Homola, "Present and future of surface plasmon resonance biosensors," *Analytical and Bioanalytical Chemistry* **377**(3), 528–539 (2003).
61. M. Liscidini and J. E. Sipe, "Analysis of Bloch-surface-wave assisted diffraction-based biosensors," *J. Opt. Soc. Am. B* **26**(2), 279 (2009).
62. A. Messner, P. A. Jud, J. Winiger, M. Eppenberger, D. Chelladurai, W. Heni, B. Baeuerle, U. Koch, P. Ma, C. Haffner, H. Xu, D. L. Elder, L. R. Dalton, J. Smajic, and J. Leuthold, "Broadband Metallic Fiber-to-Chip Couplers and a Low-Complexity Integrated Plasmonic Platform," *Nano Lett.* **21**(11), 4539–4545 (2021).
63. R.-M. Ma, R. F. Oulton, V. J. Sorger, G. Bartal, and X. Zhang, "Room-temperature sub-diffraction-limited plasmon laser by total internal reflection," *Nature Mater* **10**(2), 110–113 (2011).
64. X. Wang, X. Jiang, Q. You, J. Guo, X. Dai, and Y. Xiang, "Tunable and multichannel terahertz perfect absorber due to Tamm surface plasmons with graphene," *Photon. Res.* **5**(6), 536 (2017).
65. T. Kovalevich, P. Boyer, M. Suarez, R. Salut, M.-S. Kim, H. P. Herzig, M.-P. Bernal, and T. Grosjean, "Polarization controlled directional propagation of Bloch surface wave," *Opt. Express* **25**(5), 5710 (2017).
66. N. Kedei, D. J. Lundberg, A. Toth, P. Welburn, S. H. Garfield, and P. M. Blumberg, "Characterization of the Interaction of Ingenol 3-Angelate with Protein Kinase C," *Cancer Res* **64**(9), 3243–3255 (2004).
67. M. M. Baksh, M. Jaros, and J. T. Groves, "Detection of molecular interactions at membrane surfaces through colloid phase transitions," *Nature* **427**(6970), 139–141 (2004).
68. A. L. Lereu, M. Zerrad, A. Passian, and C. Amra, "Surface plasmons and Bloch surface waves: Towards optimized ultra-sensitive optical sensors," *Appl. Phys. Lett.* **111**(1), 011107 (2017).
69. A. P. Vinogradov, A. V. Dorofeenko, S. G. Erokhin, M. Inoue, A. A. Lisyansky, A. M. Merzlikin, and A. B. Granovsky, "Surface state peculiarities in one-dimensional photonic crystal interfaces," *Phys. Rev. B* **74**(4), 045128 (2006).
70. A. V. Kavokin, I. A. Shelykh, and G. Malpuech, "Lossless interface modes at the boundary between two periodic dielectric structures," *Phys. Rev. B* **72**(23), 233102 (2005).

71. T. Goto, A. V. Dorofeenko, A. M. Merzlikin, A. V. Baryshev, A. P. Vinogradov, M. Inoue, A. A. Lisyansky, and A. B. Granovsky, "Optical Tamm States in One-Dimensional Magnetophotonic Structures," *Phys. Rev. Lett.* **101**(11), 113902 (2008).
72. I. Tamm, "Über eine mögliche Art der Elektronenbindung an Kristalloberflächen," *Z. Physik* **76**(11–12), 849–850 (1932).
73. M. E. Sasin, R. P. Seisyan, M. A. Kalitchevski, S. Brand, R. A. Abram, J. M. Chamberlain, A. Yu. Egorov, A. P. Vasil'ev, V. S. Mikhlin, and A. V. Kavokin, "Tamm plasmon polaritons: Slow and spatially compact light," *Appl. Phys. Lett.* **92**(25), 251112 (2008).
74. M. Kalitchevski, I. Iorsh, S. Brand, R. A. Abram, J. M. Chamberlain, A. V. Kavokin, and I. A. Shelykh, "Tamm plasmon-polaritons: Possible electromagnetic states at the interface of a metal and a dielectric Bragg mirror," *Phys. Rev. B* **76**(16), 165415 (2007).
75. B. Auguie, M. C. Fuertes, P. C. Angelomé, N. L. Abdala, G. J. A. A. Soler Illia, and A. Fainstein, "Tamm Plasmon Resonance in Mesoporous Multilayers: Toward a Sensing Application," *ACS Photonics* **1**(9), 775–780 (2014).
76. S. Kumar, P. S. Maji, and R. Das, "Tamm-plasmon resonance based temperature sensor in a Ta<sub>2</sub>O<sub>5</sub>/SiO<sub>2</sub> based distributed Bragg reflector," *Sensors and Actuators A: Physical* **260**, 10–15 (2017).
77. W. L. Zhang, F. Wang, Y. J. Rao, and Y. Jiang, "Novel sensing concept based on optical Tamm plasmon," *Opt. Express* **22**(12), 14524 (2014).
78. O. Buchnev, A. Belosludtsev, V. Reshetnyak, D. R. Evans, and V. A. Fedotov, "Observing and controlling a Tamm plasmon at the interface with a metasurface," *Nanophotonics* **9**(4), 897–903 (2020).
79. M. Kalitchevski, S. Brand, R. A. Abram, I. Iorsh, A. V. Kavokin, and I. A. Shelykh, "Hybrid states of Tamm plasmons and exciton polaritons," *Appl. Phys. Lett.* **95**(25), 251108 (2009).
80. A. Kavokin and G. Malpuech, *Cavity Polaritons* (Elsevier, 2003).
81. A. Kavokin, I. Shelykh, and G. Malpuech, "Optical Tamm states for the fabrication of polariton lasers," *Appl. Phys. Lett.* **87**(26), 261105 (2005).
82. T. Hu, Y. Wang, L. Wu, L. Zhang, Y. Shan, J. Lu, J. Wang, S. Luo, Z. Zhang, L. Liao, S. Wu, X. Shen, and Z. Chen, "Strong coupling between Tamm plasmon polariton and two dimensional semiconductor excitons," *Appl. Phys. Lett.* **110**(5), 051101 (2017).
83. O. Gazzano, S. M. de Vasconcellos, K. Gauthron, C. Symonds, J. Bloch, P. Voisin, J. Bellessa, A. Lemaître, and P. Senellart, "Evidence for Confined Tamm Plasmon Modes under Metallic Microdisks and Application to the Control of Spontaneous Optical Emission," *Phys. Rev. Lett.* **107**(24), 247402 (2011).
84. C. Symonds, G. Lheureux, J. P. Hugonin, J. J. Greffet, J. Laverdant, G. Brucoli, A. Lemaître, P. Senellart, and J. Bellessa, "Confined Tamm Plasmon Lasers," *Nano Lett.* **13**(7), 3179–3184 (2013).

85. G. Lheureux, S. Azzini, C. Symonds, P. Senellart, A. Lemaître, C. Sauvan, J.-P. Hugonin, J.-J. Greffet, and J. Bellessa, "Polarization-Controlled Confined Tamm Plasmon Lasers," *ACS Photonics* **2**(7), 842–848 (2015).
86. W. L. Barnes, A. Dereux, and T. W. Ebbesen, "Surface plasmon subwavelength optics," *Nature* **424**(6950), 824–830 (2003).
87. K. Kneipp, H. Kneipp, I. Itzkan, R. R. Dasari, and M. S. Feld, "Surface-enhanced Raman scattering and biophysics," *J. Phys.: Condens. Matter* **14**(18), R597–R624 (2002).
88. A. Paulauskas, A. Selskis, V. Bukauskas, V. Vaicikauskas, A. Ramanavicius, and Z. Balevicius, "Real time study of amalgam formation and mercury adsorption on thin gold film by total internal reflection ellipsometry," *Applied Surface Science* **427**, 298–303 (2018).
89. A. V. Krasavin, A. V. Zayats, and N. I. Zheludev, "Active control of surface plasmon–polariton waves," *J. Opt. A: Pure Appl. Opt.* **7**(2), S85–S89 (2005).
90. J. Seidel, S. Grafström, and L. Eng, "Stimulated Emission of Surface Plasmons at the Interface between a Silver Film and an Optically Pumped Dye Solution," *Phys. Rev. Lett.* **94**(17), 177401 (2005).
91. A. P. Hibbins and J. R. Sambles, "Squeezing millimeter waves into microns," *Phys. Rev. Lett.* **92**(14), 143904 (2004).
92. A. V. Zayats and I. I. Smolyaninov, "Near-field photonics: surface plasmon polaritons and localized surface plasmons," *J. Opt. A: Pure Appl. Opt.* **5**(4), S16–S50 (2003).
93. P. Berini, R. Charbonneau, N. Lahoud, and G. Mattiussi, "Characterization of long-range surface-plasmon-polariton waveguides," *Journal of Applied Physics* **98**(4), 043109 (2005).
94. P. Berini, "Plasmon-polariton waves guided by thin lossy metal films of finite width: Bound modes of symmetric structures," *Phys. Rev. B* **61**(15), 10484–10503 (2000).
95. U. Koch, C. Uhl, H. Hettrich, Y. Fedoryshyn, D. Moor, M. Baumann, C. Hoessbacher, W. Heni, B. Baeuerle, B. I. Bitachon, A. Josten, M. Ayata, H. Xu, D. L. Elder, L. R. Dalton, E. Mentovich, P. Bakopoulos, S. Lischke, A. Krüger, L. Zimmermann, D. Tsiokos, N. Pleros, M. Möller, and J. Leuthold, "Plasmonics—high-speed photonics for co-integration with electronics," *Jpn. J. Appl. Phys.* **60**(SB), SB0806 (2021).
96. V. G. Bordo and H.-G. Rubahn, *Optics and Spectroscopy at Surfaces and Interfaces* (Wiley-VCH, 2005).
97. A. Otto, "Excitation of nonradiative surface plasma waves in silver by the method of frustrated total reflection," *Z. Physik* **216**(4), 398–410 (1968).
98. E. Kretschmann and H. Raether, "Notizen: Radiative Decay of Non Radiative Surface Plasmons Excited by Light," *Zeitschrift für Naturforschung A* **23**(12), 2135–2136 (1968).
99. M. Sarkar, M. Besbes, J. Moreau, J.-F. Bryche, A. Olivéro, G. Barbillon, A.-L. Coutrot, B. Bartenlian, and M. Canva, "Hybrid Plasmonic Mode by



- Resonant Coupling of Localized Plasmons to Propagating Plasmons in a Kretschmann Configuration," *ACS Photonics* **2**(2), 237–245 (2015).
100. S. Azzini, G. Lheureux, C. Symonds, J.-M. Benoit, P. Senellart, A. Lemaitre, J.-J. Greffet, C. Blanchard, C. Sauvan, and J. Bellessa, "Generation and Spatial Control of Hybrid Tamm Plasmon/Surface Plasmon Modes," *ACS Photonics* **3**(10), 1776–1781 (2016).
  101. R. Das, T. Srivastava, and R. Jha, "Tamm-plasmon and surface-plasmon hybrid-mode based refractometry in photonic bandgap structures," *Opt. Lett.* **39**(4), 896 (2014).
  102. R. Das, T. Srivastava, and R. Jha, "On the performance of Tamm-plasmon and surface-plasmon hybrid-mode refractive-index sensor in metallo-dielectric heterostructure configuration," *Sensors and Actuators B: Chemical* **206**, 443–448 (2015).
  103. V. G. Kravets, F. Schedin, and A. N. Grigorenko, "Extremely Narrow Plasmon Resonances Based on Diffraction Coupling of Localized Plasmons in Arrays of Metallic Nanoparticles," *Phys. Rev. Lett.* **101**(8), 087403 (2008).
  104. B. Augu e and W. L. Barnes, "Collective Resonances in Gold Nanoparticle Arrays," *Phys. Rev. Lett.* **101**(14), 143902 (2008).
  105. D. Wang, A. Yang, A. J. Hryn, G. C. Schatz, and T. W. Odom, "Superlattice Plasmons in Hierarchical Au Nanoparticle Arrays," *ACS Photonics* **2**(12), 1789–1794 (2015).
  106. I. Romero, J. Aizpurua, G. W. Bryant, and F. J. Garc a De Abajo, "Plasmons in nearly touching metallic nanoparticles: singular response in the limit of touching dimers," *Opt. Express* **14**(21), 9988 (2006).
  107. A. I. V akev inen, R. J. Moerland, H. T. Rekola, A.-P. Eskelinen, J.-P. Martikainen, D.-H. Kim, and P. T orm a, "Plasmonic Surface Lattice Resonances at the Strong Coupling Regime," *Nano Lett.* **14**(4), 1721–1727 (2014).
  108. M. Ramezani, A. Halpin, A. I. Fern andez-Dom nguez, J. Feist, S. R.-K. Rodriguez, F. J. Garcia-Vidal, and J. G omez Rivas, "Plasmon-exciton-polariton lasing," *Optica* **4**(1), 31 (2017).
  109. A. Fernandez-Bravo, D. Wang, E. S. Barnard, A. Teitelboim, C. Tajon, J. Guan, G. C. Schatz, B. E. Cohen, E. M. Chan, P. J. Schuck, and T. W. Odom, "Ultralow-threshold, continuous-wave upconverting lasing from subwavelength plasmons," *Nat. Mater.* **18**(11), 1172–1176 (2019).
  110. M. Dridi and G. C. Schatz, "Model for describing plasmon-enhanced lasers that combines rate equations with finite-difference time-domain," *J. Opt. Soc. Am. B* **30**(11), 2791 (2013).
  111. R. W. Wood, "XLII. *On a remarkable case of uneven distribution of light in a diffraction grating spectrum,*" *The London, Edinburgh, and Dublin Philosophical Magazine and Journal of Science* **4**(21), 396–402 (1902).
  112. Lord Rayleigh, "On the Dynamical Theory of Gratings.," *Proceedings of the Royal Society of London.* **79**(532), 399–416 (1907).

113. H. Gao, J. M. McMahon, M. H. Lee, J. Henzie, S. K. Gray, G. C. Schatz, and T. W. Odom, "Rayleigh anomaly-surface plasmon polariton resonances in palladium and gold subwavelength hole arrays," *Opt. Express* **17**(4), 2334 (2009).
114. J. M. McMahon, J. Henzie, T. W. Odom, G. C. Schatz, and S. K. Gray, "Tailoring the sensing capabilities of nanohole arrays in gold films with Rayleigh anomaly-surface plasmon polaritons," *Opt. Express* **15**(26), 18119 (2007).
115. N. Gisbert Quilis, M. van Dongen, P. Venugopalan, D. Kotlarek, C. Petri, A. Moreno Cencerrado, S. Stanescu, J. L. Toca Herrera, U. Jonas, M. Möller, A. Mourran, and J. Dostalek, "Actively Tunable Collective Localized Surface Plasmons by Responsive Hydrogel Membrane," *Adv. Optical Mater.* **7**(15), 1900342 (2019).
116. F. Korte, J. Koch, and B. N. Chichkov, "Formation of microbumps and nanojets on gold targets by femtosecond laser pulses," *Appl. Phys. A* **79**(4–6), 879–881 (2004).
117. J. P. Moening, S. S. Thanawala, and D. G. Georgiev, "Formation of high-aspect-ratio protrusions on gold films by localized pulsed laser irradiation," *Appl. Phys. A* **95**(3), 635–638 (2009).
118. V. G. Kravets, F. Schedin, R. Jalil, L. Britnell, R. V. Gorbachev, D. Ansell, B. Thackray, K. S. Novoselov, A. K. Geim, A. V. Kabashin, and A. N. Grigorenko, "Singular phase nano-optics in plasmonic metamaterials for label-free single-molecule detection," *Nature Mater* **12**(4), 304–309 (2013).
119. Ž. Prielaidas, S. Juodkazis, and E. Stankevičius, "Thermal control of SZ2080 photopolymerization in four-beam interference lithography," *Phys. Chem. Chem. Phys.* **22**(9), 5038–5045 (2020).
120. X. Gao, J. Hale, S. Heckens, and J. A. Woollam, "Studies of metallic multilayer structures, optical properties, and oxidation using *in situ* spectroscopic ellipsometry," *Journal of Vacuum Science & Technology A: Vacuum, Surfaces, and Films* **16**(2), 429–435 (1998).
121. J. Xie, D. Zhang, X.-Q. Yan, M. Ren, X. Zhao, F. Liu, R. Sun, X. Li, Z. Li, S. Chen, Z.-B. Liu, and J.-G. Tian, "Optical properties of chemical vapor deposition-grown PtSe<sub>2</sub> characterized by spectroscopic ellipsometry," *2D Mater.* **6**(3), 035011 (2019).
122. E. Langereis, S. B. S. Heil, H. C. M. Knoops, W. Keuning, M. C. M. van de Sanden, and W. M. M. Kessels, "*In situ* spectroscopic ellipsometry as a versatile tool for studying atomic layer deposition," *J. Phys. D: Appl. Phys.* **42**(7), 073001 (2009).
123. R. M. Azzam and N. M. Bashara, *Ellipsometry and Polarized Light*, paperback ed., 5. impr, North-Holland Personal Library (North-Holland, 2003).
124. H. Arwin, M. Poksinski, and K. Johansen, "Total internal reflection ellipsometry: principles and applications," *Appl. Opt.* **43**(15), 3028 (2004).

125. T. Tolenis, L. Grinevičiūtė, R. Buzelis, L. Smalakys, E. Pupka, S. Melnikas, A. Selskis, R. Drazdys, and A. Melninkaitis, "Sculptured anti-reflection coatings for high power lasers," *Opt. Mater. Express* **7**(4), 1249 (2017).
126. R. Lukose, N. Zurauskiene, S. Balevicius, V. Stankevici, S. Keršulis, V. Plausinaitiene, and R. Navickas, "Hybrid graphene-manganite thin film structure for magnetoresistive sensor application," *Nanotechnology* **30**(35), 355503 (2019).
127. D. S. Ivanov, A. I. Kuznetsov, V. P. Lipp, B. Rethfeld, B. N. Chichkov, M. E. Garcia, and W. Schulz, "Short laser pulse nanostructuring of metals: direct comparison of molecular dynamics modeling and experiment," *Appl. Phys. A* **111**(3), 675–687 (2013).
128. C. Unger, J. Koch, L. Overmeyer, and B. N. Chichkov, "Time-resolved studies of femtosecond-laser induced melt dynamics," *Opt. Express* **20**(22), 24864 (2012).
129. L. M. Malard, M. A. Pimenta, G. Dresselhaus, and M. S. Dresselhaus, "Raman spectroscopy in graphene," *Physics Reports* **473**(5–6), 51–87 (2009).
130. R. Trusovas, G. Račiukaitis, G. Niaura, J. Barkauskas, G. Valušis, and R. Pauliukaite, "Recent Advances in Laser Utilization in the Chemical Modification of Graphene Oxide and Its Applications," *Advanced Optical Materials* **4**(1), 37–65 (2016).
131. Z. Qi, X. Zhu, H. Jin, T. Zhang, X. Kong, R. S. Ruoff, Z. Qiao, and H. Ji, "Rapid Identification of the Layer Number of Large-Area Graphene on Copper," *Chem. Mater.* **30**(6), 2067–2073 (2018).
132. A. C. Ferrari, "Raman spectroscopy of graphene and graphite: Disorder, electron–phonon coupling, doping and nonadiabatic effects," *Solid State Communications* **143**(1–2), 47–57 (2007).
133. A. C. Ferrari, J. C. Meyer, V. Scardaci, C. Casiraghi, M. Lazzeri, F. Mauri, S. Piscanec, D. Jiang, K. S. Novoselov, S. Roth, and A. K. Geim, "Raman Spectrum of Graphene and Graphene Layers," *Phys. Rev. Lett.* **97**(18), 187401 (2006).
134. A. Gupta, G. Chen, P. Joshi, S. Tadigadapa, and Eklund, "Raman Scattering from High-Frequency Phonons in Supported *n* -Graphene Layer Films," *Nano Lett.* **6**(12), 2667–2673 (2006).
135. J.-S. Hwang, Y.-H. Lin, J.-Y. Hwang, R. Chang, S. Chattopadhyay, C.-J. Chen, P. Chen, H.-P. Chiang, T.-R. Tsai, L.-C. Chen, and K.-H. Chen, "Imaging layer number and stacking order through formulating Raman fingerprints obtained from hexagonal single crystals of few layer graphene," *Nanotechnology* **24**(1), 015702 (2013).
136. Y. P. Meshcheryakov and N. M. Bulgakova, "Thermoelastic modeling of microbump and nanojet formation on nanosize gold films under femtosecond laser irradiation," *Appl. Phys. A* **82**(2), 363–368 (2006).

137. I. Plikusiene, Z. Balevicius, A. Ramanaviciene, J. Talbot, G. Mickiene, S. Balevicius, A. Stirke, A. Tereshchenko, L. Tamosaitis, G. Zvirblis, and A. Ramanavicius, "Evaluation of affinity sensor response kinetics towards dimeric ligands linked with spacers of different rigidity: Immobilized recombinant granulocyte colony-stimulating factor based synthetic receptor binding with genetically engineered dimeric analyte derivatives," *Biosensors and Bioelectronics* 112112 (2020).
138. P. Vasa, W. Wang, R. Pomraenke, M. Lammers, M. Maiuri, C. Manzoni, G. Cerullo, and C. Lienau, "Real-time observation of ultrafast Rabi oscillations between excitons and plasmons in metal nanostructures with J-aggregates," *Nature Photon* 7(2), 128–132 (2013).
139. R. Ulbricht, E. Hendry, J. Shan, T. F. Heinz, and M. Bonn, "Carrier dynamics in semiconductors studied with time-resolved terahertz spectroscopy," *Rev. Mod. Phys.* 83(2), 543–586 (2011).
140. H. Leng, B. Szychowski, M.-C. Daniel, and M. Pelton, "Strong coupling and induced transparency at room temperature with single quantum dots and gap plasmons," *Nat Commun* 9(1), 4012 (2018).
141. Z. Balevicius, I. Baleviciute, S. Tumenas, L. Tamosaitis, A. Stirke, A. Makaraviciute, A. Ramanaviciene, and A. Ramanavicius, "In situ study of ligand–receptor interaction by total internal reflection ellipsometry," *Thin Solid Films* 571, 744–748 (2014).
142. C. Symonds, A. Lemaître, E. Homeyer, J. C. Plenet, and J. Bellessa, "Emission of Tamm plasmon/exciton polaritons," *Appl. Phys. Lett.* 95(15), 151114 (2009).
143. N. Lundt, S. Klemmt, E. Cherotchenko, S. Betzold, O. Iff, A. V. Nalitov, M. Klaas, C. P. Dietrich, A. V. Kavokin, S. Höfling, and C. Schneider, "Room-temperature Tamm-plasmon exciton-polaritons with a WSe<sub>2</sub> monolayer," *Nat Commun* 7(1), 13328 (2016).
144. Z. Liu, J. Li, Z. Liu, W. Li, J. Li, C. Gu, and Z.-Y. Li, "Fano resonance Rabi splitting of surface plasmons," *Sci Rep* 7(1), 8010 (2017).
145. A. N. Grigorenko, M. Polini, and K. S. Novoselov, "Graphene plasmonics," *Nature Photon* 6(11), 749–758 (2012).
146. S. Xiao, T. Wang, T. Liu, X. Yan, Z. Li, and C. Xu, "Active modulation of electromagnetically induced transparency analogue in terahertz hybrid metal-graphene metamaterials," *Carbon* 126, 271–278 (2018).
147. Y. Cai, J. Zhu, Q. H. Liu, T. Lin, J. Zhou, L. Ye, and Z. Cai, "Enhanced spatial near-infrared modulation of graphene-loaded perfect absorbers using plasmonic nanoslits," *Opt. Express* 23(25), 32318 (2015).
148. Y. Cai, J. Zhu, and Q. H. Liu, "Tunable enhanced optical absorption of graphene using plasmonic perfect absorbers," *Appl. Phys. Lett.* 106(4), 043105 (2015).
149. F. H. L. Koppens, D. E. Chang, and F. J. García de Abajo, "Graphene Plasmonics: A Platform for Strong Light–Matter Interactions," *Nano Lett.* 11(8), 3370–3377 (2011).

150. A. K. Geim and K. S. Novoselov, "The rise of graphene," in *Nanoscience and Technology* (Co-Published with Macmillan Publishers Ltd, UK, 2009), pp. 11–19.
151. M. Baitimirova, R. Viter, J. Andzane, A. van der Lee, D. Voiry, I. Iatsunskyi, E. Coy, L. Mikoliunaite, S. Tumenas, K. Załęski, Z. Balevicius, I. Baleviciute, A. Ramanaviciene, A. Ramanavicius, S. Jurga, D. Erts, and M. Bechelany, "Tuning of Structural and Optical Properties of Graphene/ZnO Nanolaminates," *J. Phys. Chem. C* **120**(41), 23716–23725 (2016).
152. F. Schedin, E. Lidorikis, A. Lombardo, V. G. Kravets, A. K. Geim, A. N. Grigorenko, K. S. Novoselov, and A. C. Ferrari, "Surface-Enhanced Raman Spectroscopy of Graphene," *ACS Nano* **4**(10), 5617–5626 (2010).
153. Y. Cai, Z. Wang, S. Yan, L. Ye, and J. Zhu, "Ultraviolet absorption band engineering of graphene by integrated plasmonic structures," *Opt. Mater. Express* **8**(11), 3295 (2018).
154. V. G. Kravets, R. Jalil, Y.-J. Kim, D. Ansell, D. E. Aznakayeva, B. Thackray, L. Britnell, B. D. Belle, F. Withers, I. P. Radko, Z. Han, S. I. Bozhevolnyi, K. S. Novoselov, A. K. Geim, and A. N. Grigorenko, "Graphene-protected copper and silver plasmonics," *Sci Rep* **4**(1), 5517 (2015).
155. V. G. Kravets, F. Schedin, R. Jalil, L. Britnell, K. S. Novoselov, and A. N. Grigorenko, "Surface Hydrogenation and Optics of a Graphene Sheet Transferred onto a Plasmonic Nanoarray," *J. Phys. Chem. C* **116**(6), 3882–3887 (2012).
156. J. Hu, E. Yao, W. Xie, W. Liu, D. Li, Y. Lu, and Q. Zhan, "Strong longitudinal coupling of Tamm plasmon polaritons in graphene/DBR/Ag hybrid structure," *Opt. Express* **27**(13), 18642 (2019).
157. Y. M. Qing, H. F. Ma, and T. J. Cui, "Flexible control of light trapping and localization in a hybrid Tamm plasmonic system," *Opt. Lett.* **44**(13), 3302 (2019).
158. A. Ciesielski, L. Skowronski, M. Trzcinski, and T. Szoplik, "Controlling the optical parameters of self-assembled silver films with wetting layers and annealing," *Applied Surface Science* **421**, 349–356 (2017).
159. J. W. Weber, V. E. Calado, and M. C. M. van de Sanden, "Optical constants of graphene measured by spectroscopic ellipsometry," *Appl. Phys. Lett.* **97**(9), 091904 (2010).
160. J. W. Suk, R. D. Piner, J. An, and R. S. Ruoff, "Mechanical Properties of Monolayer Graphene Oxide," *ACS Nano* **4**(11), 6557–6564 (2010).
161. Y. V. Stebunov, O. A. Aftenieva, A. V. Arsenin, and V. S. Volkov, "Highly Sensitive and Selective Sensor Chips with Graphene-Oxide Linking Layer," *ACS Appl. Mater. Interfaces* **7**(39), 21727–21734 (2015).

162. X. Wu, S. K. Gray, and M. Pelton, "Quantum-dot-induced transparency in a nanoscale plasmonic resonator," *Opt. Express* **18**(23), 23633 (2010).
163. H. Arwin, "TIRE and SPR-Enhanced SE for Adsorption Processes," in *Ellipsometry of Functional Organic Surfaces and Films*, K. Hinrichs and K.-J. Eichhorn, eds. (Springer Berlin Heidelberg, 2014), **52**, pp. 249–264.
164. B. Liedberg, C. Nylander, and I. Lundström, "Biosensing with surface plasmon resonance — how it all started," *Biosensors and Bioelectronics* **10**(8), i–ix (1995).
165. A. Kausaite-Minkstimiene, A. Ramanaviciene, J. Kirlyte, and A. Ramanavicius, "Comparative Study of Random and Oriented Antibody Immobilization Techniques on the Binding Capacity of Immunosensor," *Anal. Chem.* **82**(15), 6401–6408 (2010).
166. W. Wang, Y. Yang, S. Wang, V. J. Nagaraj, Q. Liu, J. Wu, and N. Tao, "Label-free measuring and mapping of binding kinetics of membrane proteins in single living cells," *Nature Chem* **4**(10), 846–853 (2012).
167. J. Zhou, Q. Qi, C. Wang, Y. Qian, G. Liu, Y. Wang, and L. Fu, "Surface plasmon resonance (SPR) biosensors for food allergen detection in food matrices," *Biosensors and Bioelectronics* **142**, 111449 (2019).
168. A. Makaraviciute and A. Ramanaviciene, "Site-directed antibody immobilization techniques for immunosensors," *Biosensors and Bioelectronics* **50**, 460–471 (2013).
169. Z. Balevicius, J. Talbot, L. Tamosaitis, I. Plikusiene, A. Stirke, G. Mickiene, S. Balevicius, A. Paulauskas, and A. Ramanavicius, "Modelling of immunosensor response: the evaluation of binding kinetics between an immobilized receptor and structurally-different genetically engineered ligands," *Sensors and Actuators B: Chemical* **297**, 126770 (2019).
170. A. Nooke, U. Beck, A. Hertwig, A. Krause, H. Krüger, V. Lohse, D. Negendank, and J. Steinbach, "On the application of gold based SPR sensors for the detection of hazardous gases," *Sensors and Actuators B: Chemical* **149**(1), 194–198 (2010).
171. Z. Balevicius, A. Makaraviciute, G.-J. Babonas, S. Tumenas, V. Bukauskas, A. Ramanaviciene, and A. Ramanavicius, "Study of optical anisotropy in thin molecular layers by total internal reflection ellipsometry," *Sensors and Actuators B: Chemical* **181**, 119–124 (2013).
172. I. Baleviciute, Z. Balevicius, A. Makaraviciute, A. Ramanaviciene, and A. Ramanavicius, "Study of antibody/antigen binding kinetics by total internal reflection ellipsometry," *Biosensors and Bioelectronics* **39**(1), 170–176 (2013).
173. S.-G. Huang, K.-P. Chen, and S.-C. Jeng, "Phase sensitive sensor on Tamm plasmon devices," *Opt. Mater. Express* **7**(4), 1267 (2017).

174. Y. Tsurimaki, J. K. Tong, V. N. Boriskin, A. Semenov, M. I. Ayzatsky, Y. P. Machekhin, G. Chen, and S. V. Boriskina, "Topological Engineering of Interfacial Optical Tamm States for Highly Sensitive Near-Singular-Phase Optical Detection," *ACS Photonics* **5**(3), 929–938 (2018).
175. Z. Balevicius and A. Baskys, "Optical Dispersions of Bloch Surface Waves and Surface Plasmon Polaritons: Towards Advanced Biosensors," *Materials* **12**(19), 3147 (2019).
176. A. Sinibaldi, N. Danz, E. Descrovi, P. Munzert, U. Schulz, F. Sonntag, L. Dominici, and F. Michelotti, "Direct comparison of the performance of Bloch surface wave and surface plasmon polariton sensors," *Sensors and Actuators B: Chemical* **174**, 292–298 (2012).
177. J. A. De Feijter, J. Benjamins, and F. A. Veer, "Ellipsometry as a tool to study the adsorption behavior of synthetic and biopolymers at the air-water interface," *Biopolymers* **17**(7), 1759–1772 (1978).
178. V. Ball and J. J. Ramsden, "Buffer dependence of refractive index increments of protein solutions," *Biopolymers* **46**(7), 489–492 (1998).
179. X. Shan, U. Patel, S. Wang, R. Iglesias, and N. Tao, "Imaging Local Electrochemical Current via Surface Plasmon Resonance," *Science* **327**(5971), 1363–1366 (2010).
180. S. Patskovsky, V. Latendresse, A.-M. Dallaire, L. Doré-Mathieu, and M. Meunier, "Combined surface plasmon resonance and impedance spectroscopy systems for biosensing," *Analyst* **139**(3), 596–602 (2014).
181. X. Kang, G. Cheng, and S. Dong, "A novel electrochemical SPR biosensor," *Electrochemistry Communications* **3**(9), 489–493 (2001).
182. S. Michaelis, J. Wegener, and R. Robelek, "Label-free monitoring of cell-based assays: Combining impedance analysis with SPR for multiparametric cell profiling," *Biosensors and Bioelectronics* **49**, 63–70 (2013).
183. H. T. M. Phan, S. Bartelt-Hunt, K. B. Rodenhausen, M. Schubert, and J. C. Bartz, "Investigation of Bovine Serum Albumin (BSA) Attachment onto Self-Assembled Monolayers (SAMs) Using Combinatorial Quartz Crystal Microbalance with Dissipation (QCM-D) and Spectroscopic Ellipsometry (SE)," *PLoS ONE* **10**(10), e0141282 (2015).
184. N. Kananizadeh, C. Rice, J. Lee, K. B. Rodenhausen, D. Sekora, M. Schubert, E. Schubert, S. Bartelt-Hunt, and Y. Li, "Combined quartz crystal microbalance with dissipation (QCM-D) and generalized ellipsometry (GE) to characterize the deposition of titanium dioxide nanoparticles on model rough surfaces," *Journal of Hazardous Materials* **322**, 118–128 (2017).
185. S. Adam, M. Koenig, K. B. Rodenhausen, K.-J. Eichhorn, U. Oertel, M. Schubert, M. Stamm, and P. Uhlmann, "Quartz crystal microbalance with coupled spectroscopic ellipsometry-study of temperature-responsive polymer brush systems," *Applied Surface Science* **421**, 843–851 (2017).

186. E. Bittrich, K. B. Rodenhausen, K.-J. Eichhorn, T. Hofmann, M. Schubert, M. Stamm, and P. Uhlmann, "Protein adsorption on and swelling of polyelectrolyte brushes: A simultaneous ellipsometry-quartz crystal microbalance study," *Biointerphases* **5**(4), 159–167 (2010).
187. H.-H. Hsiao, C. H. Chu, and D. P. Tsai, "Fundamentals and Applications of Metasurfaces," *Small Methods* **1**(4), 1600064 (2017).
188. A. Juneau-Fecteau, R. Savin, A. Boucherif, and L. G. Fr chet, "A practical Tamm plasmon sensor based on porous Si," *AIP Advances* **11**(6), 065305 (2021).
189. J. Volk, T. L. Grand, I. B rsony, J. Gombk to, and J. J. Ramsden, "Porous silicon multilayer stack for sensitive refractive index determination of pure solvents," *J. Phys. D: Appl. Phys.* **38**(8), 1313–1317 (2005).
190. D. Dorfner, T. Zabel, T. H rlimann, N. Hauke, L. Frandsen, U. Rant, G. Abstreiter, and J. Finley, "Photonic crystal nanostructures for optical biosensing applications," *Biosensors and Bioelectronics* **24**(12), 3688–3692 (2009).
191. M. Rabe, D. Verdes, and S. Seeger, "Understanding protein adsorption phenomena at solid surfaces," *Advances in Colloid and Interface Science* **162**(1–2), 87–106 (2011).
192. Z. Balevicius, V. Vaicikauskas, and G.-J. Babonas, "The role of surface roughness in total internal reflection ellipsometry of hybrid systems," *Applied Surface Science* **256**(3), 640–644 (2009).
193. "Schott Optical glass," .
194. C. M. Herzinger, B. Johs, W. A. McGahan, J. A. Woollam, and W. Paulson, "Ellipsometric determination of optical constants for silicon and thermally grown silicon dioxide via a multi-sample, multi-wavelength, multi-angle investigation," *Journal of Applied Physics* **83**(6), 3323–3336 (1998).
195. D. I. Yakubovsky, A. V. Arsenin, Y. V. Stebunov, D. Yu. Fedyanin, and V. S. Volkov, "Optical constants and structural properties of thin gold films," *Opt. Express* **25**(21), 25574 (2017).
196. J. A. Woollam, *CompleteEASE Data Analysis Manual* (J. A. Woollam Co., Inc., 2011).
197. A. Kudelski, "Influence of electrostatically bound proteins on the structure of linkage monolayers: adsorption of bovine serum albumin on silver and gold substrates coated with monolayers of 2-mercaptoethanesulphonate," *Vibrational Spectroscopy* **33**(1–2), 197–204 (2003).
198. T. Kasputis, A. Pieper, M. Schubert, and A. K. Pannier, "Dynamic analysis of DNA nanoparticle immobilization to model biomaterial substrates using combinatorial spectroscopic ellipsometry and quartz crystal microbalance with dissipation," *Thin Solid Films* **571**, 637–643 (2014).



199. M. Kauranen and A. V. Zayats, "Nonlinear plasmonics," *Nature Photon* **6**(11), 737–748 (2012).
200. C. Ropers, C. C. Neacsu, T. Elsaesser, M. Albrecht, M. B. Raschke, and C. Lienau, "Grating-Coupling of Surface Plasmons onto Metallic Tips: A Nanoconfined Light Source," *Nano Lett.* **7**(9), 2784–2788 (2007).
201. P. Nordlander, C. Oubre, E. Prodan, K. Li, and M. I. Stockman, "Plasmon Hybridization in Nanoparticle Dimers," *Nano Lett.* **4**(5), 899–903 (2004).
202. E. Prodan and P. Nordlander, "Plasmon hybridization in spherical nanoparticles," *The Journal of Chemical Physics* **120**(11), 5444–5454 (2004).
203. P. Nordlander and E. Prodan, "Plasmon Hybridization in Nanoparticles near Metallic Surfaces," *Nano Lett.* **4**(11), 2209–2213 (2004).
204. W. Wang, M. Ramezani, A. I. Väkeväinen, P. Törmä, J. G. Rivas, and T. W. Odom, "The rich photonic world of plasmonic nanoparticle arrays," *Materials Today* **21**(3), 303–314 (2018).
205. M. Seo and M. Lee, "Surface plasmon resonance and coloration in stainless steel with a 2D periodic texture," *Appl. Phys. A* **125**(9), 624 (2019).
206. D. Pavlov, S. Syubaev, A. Kuchmizhak, S. Gurbatov, O. Vitrik, E. Modin, S. Kudryashov, X. Wang, S. Juodkazis, and M. Lapine, "Direct laser printing of tunable IR resonant nanoantenna arrays," *Applied Surface Science* **469**, 514–520 (2019).
207. M. Seo, J. Lee, and M. Lee, "Grating-coupled surface plasmon resonance on bulk stainless steel," *Opt. Express* **25**(22), 26939 (2017).
208. K. Bhatnagar, A. Pathak, D. Menke, P. V. Cornish, K. Gangopadhyay, V. Korampally, and S. Gangopadhyay, "Fluorescence enhancement from nano-gap embedded plasmonic gratings by a novel fabrication technique with HD-DVD," *Nanotechnology* **23**(49), 495201 (2012).
209. A. D. Rakić, A. B. Djurišić, J. M. Elazar, and M. L. Majewski, "Optical properties of metallic films for vertical-cavity optoelectronic devices," *Appl. Opt.* **37**(22), 5271 (1998).
210. M. Eitan, Z. Iluz, Y. Yifat, A. Boag, Y. Hanein, and J. Scheuer, "Degeneracy Breaking of Wood's Anomaly for Enhanced Refractive Index Sensing," *ACS Photonics* **2**(5), 615–621 (2015).
211. L. J. Sherry, R. Jin, C. A. Mirkin, G. C. Schatz, and R. P. Van Duyne, "Localized Surface Plasmon Resonance Spectroscopy of Single Silver Triangular Nanoprisms," *Nano Lett.* **6**(9), 2060–2065 (2006).

## CURRICULUM VITAE

**Vardas:** Ernesta  
**Pavardė:** Bužavaitė-Vertelienė  
**Gimimo data:** 1991-12-30  
**El. paštas:** ernesta.verteliene@ftmc.lt

### Išsilavinimas:

1998-2010 Žvėryno gimnazija, Vilnius.  
2010-2015 Vilniaus universitetas, Fizikos fakultetas.  
*Bakalauro laipsnis.*  
2015-2017 Vilniaus universitetas, Fizikos fakultetas.  
*Magistro laipsnis.*  
2018-2022 Vilniaus universitetas, Fizikos fakultetas bei  
VMTI Fizinių ir technologijos mokslų centras.  
*Doktorantūra.*

### Darbo patirtis:

2015-2017 Laboratorijos technikė. *Vilniaus universitetas, Fizikos fakultetas.*  
2019-2020 Inžinierė. *VMTI Fizinių ir technologijos mokslų centras.*  
2020-2022 Jaunesnioji mokslo darbuotoja. *VMTI Fizinių ir technologijos mokslų centras.*

## NOTES

Vilniaus universiteto leidykla  
Saulėtekio al. 9, III rūmai, LT-10222 Vilnius  
El. p. [info@leidykla.vu.lt](mailto:info@leidykla.vu.lt), [www.leidykla.vu.lt](http://www.leidykla.vu.lt)  
[bookshop.vu.lt](http://bookshop.vu.lt), [journals.vu.lt](http://journals.vu.lt)  
Tiražas 20 egz.